NEEYATI PANDEY

# HYDROLOGICAL HAZARDS

## MODELING AND ANALYSIS

# Hydrological Hazards: Modeling and Analysis

# Hydrological Hazards: Modeling and Analysis

Neeyati Pandey

THE INFO LIBRARY

Published by The InfoLibrary,
4/21B, First Floor, E-Block,
Model Town-II,
New Delhi-110009, India



Hydrological Hazards: Modeling and Analysis
Neeyati Pandey
ISBN: 978-93-5590-246-7

# Table of Contents

# Analysis of Damage Caused by Hydrometeorological Disasters in Texas, 1960–2016

**Srikanto H. Paul * and Hatim O. Sharif**

Department of Civil and Environmental Engineering, University of Texas at San Antonio, San Antonio, TX 78249, USA; hatim.sharif@utsa.edu
* Correspondence: srikantopaul@live.com

**Abstract:** Property damages caused by hydrometeorological disasters in Texas during the period 1960–2016 totaled $54.2 billion with hurricanes, tropical storms, and hail accounting for 56%, followed by flooding and severe thunderstorms responsible for 24% of the total damages. The current study provides normalized trends to support the assertion that the increase in property damage is a combined contribution of stronger disasters as predicted by climate change models and increases in urban development in risk prone regions such as the Texas Gulf Coast. A comparison of the temporal distribution of damages normalized by population and GDP resulted in a less statistically significant increasing trend per capita. Seasonal distribution highlights spring as the costliest season (March, April and May) while the hurricane season (June through November) is well aligned with the months of highest property damage. Normalization of property damage by GDP during 2001–2016 showed Dallas as the only metropolitan statistical area (MSA) with a significant increasing trend of the 25 MSAs in Texas. Spatial analysis of property damage per capita highlighted the regions that are at greater risk during and after a major disaster given their limited economic resources compared to more urbanized regions. Variation in the causes of damage (wind or water) and types of damage that a "Hurricane" can produce was investigated using Hazus model simulation. A comparison of published damage estimates at time of occurrence with simulation outputs for Hurricanes Carla, 1961; Alicia, 1983; and Ike, 2008 based on 2010 building exposure highlighted the impact of economic growth, susceptibility of wood building types, and the predominant cause of damage. Carla and Ike simulation models captured less than 50% of their respective estimates reported by other sources suggesting a broad geographical zone of damage with flood damage making a significant contribution. Conversely, the model damage estimates for Alicia are 50% higher than total damage estimates that were reported at the time of occurrence suggesting a substantial increase in building exposure susceptible to wind damage in the modeled region from 1983 – 2010.

**Keywords:** natural hazards; hydrometeorological disasters; HAZUS; SHELDUS; Texas; property damage; economic loss

## 1. Introduction

Recent decades have witnessed a worldwide increasing trend in both the number of natural disasters and the resulting damages. In the two most recent years of the current study, the number of natural catastrophic events has increased from 730 events ($103 billion) in 2015 to 750 events ($175 billion) in 2016. Weather-related events such as severe storms and floods had the most significant increase in frequency. During the period 1980–2016, there were a total of 16,584 natural disaster events resulting in $4.3 trillion of damage worldwide, of which 80% were either hydrological or meteorological events and 20% climatological or geophysical events [1]. During the period 1980–2017, the U.S. experienced 233 weather and climate related disasters in which overall damages/costs reached

or exceeded $1 billion (2018 CPI adjusted) for a total cost exceeding $1.5 trillion [2]. As of the date of this study, 2017 has set the record for the most expensive year for damage due to natural disasters in recorded history both globally and in the U.S.

Assessment of damages due to historic natural disasters can include direct and indirect replacement cost estimates and/or insurance payout information. The former use in this study is more applicable in longitudinal research since it is a function of available exposure value and includes all property whether insured. The Congressional Research Service reported that inflation-adjusted disaster appropriations have increased 46% from a median of $6.2 billion between 2000 and 2006 to $9.1 billion between 2007 and 2013. The hurricanes in 2017 were immense and had a much costlier impact as they collided with growing cities with higher exposure. As more people compete for real estate thereby pushing up the property values in disaster prone regions such as coastal Florida, Texas, and California, the level of property damage also increases [3]. Damage data are widely available from public sources such as Munich Re and SHELDUS but typically exclude long-term indirect costs such as healthcare discontinuity and investment opportunity cost. Therefore, there is significant uncertainty in the exact total costs of natural disasters especially when comparing damage over time and across areas of varying degrees of urban development.

There is general agreement among public and private organizations and governmental agencies including the Government Accountability Office (GAO) that the cost of natural disasters in the U.S. is increasing at a significant rate. However, there are different perspectives on whether the increase is due to more violent storms or if the increase is due to the increase in population and wealth of property that is susceptible to damage. The U.S., as well as many other countries around the world, has experienced a rise in the number of natural disaster events and losses in the last four decades primarily due to convective events which are disaster events developing out of thunderstorms, such as hail, heavy precipitation, tornadoes and strong straight-line winds. Gall et al. noted that direct losses from convective disaster events such as hurricanes, flooding, and severe storms are increasing and contribute about 75% of the total damage with hurricane and flood losses having tripled over the last 50 years [4]. A study by Sander et al. found that 80% of all losses in the U.S. from 1970 to 2009 were due to convective events that had normalized losses exceeding $250 million. The study also suggests that there is a correlation between the increase in losses and the changes in meteorological potential for severe thunderstorms driven by changes in the humidity of the troposphere [5].

The scientific community largely in agreement that the rise of humidity in the air over the last decades can be attributed to warming oceans and increased evaporation from their surfaces. The intuitive consequence is that the increase in disaster events due to climate change is responsible for the increased damage losses. However, although the relationship of climate change to disaster occurrence is accepted, the relationship of disaster occurrence and the increasing trend in property damage is still a debated topic. One perspective is that the reported increasing damage and losses from hurricanes are not necessarily evidence of any increase in hurricane or tropical storm activity but are due only to the changes in population and wealth of the impacted regions [6–8]. Klotzbach et al. reported that damage caused by tropical cyclones adjusted for inflation and normalized by regional wealth and population factors did not show an increasing trend from 1900 to 2016 in the U.S., suggesting that the increase in damages are more a function of the increased regional wealth and property exposure than the increase in number of cyclones [8].

Texas is second in population (2010 Census) only to California and has a large and diverse terrain that combines a gulf coastline that is extremely susceptible to tropical storms and hurricanes; flooding and flash flooding at the base of the Balcones Escarpment running through the mid-section of the state; heat and drought conditions in the south/southwest; and rural cold extremes in the northwest panhandle. Hydrometeorological events are the predominant disasters in Texas and have resulted in a high number of fatalities and losses to infrastructure [9,10]. The overall population growth coupled with the rapid urban and coastal development in recent decades have created an environment in which fatality rates are decreasing per capita due to population increases but property damage is increasing

due to more people with more valuable property moving into more vulnerable (disaster prone) regions. This nexus of nature and society will continue to grow in Texas in the foreseeable future and warrants ongoing analysis to help policy and decision-makers identify and prioritize the social vulnerabilities that can be managed to reduce the risk to Texas life and property. This study is intended to provide a review of historic trends and types of damage and economic losses caused by hydrometeorological disasters impacting the coastal and inland property and infrastructure of Texas from 1960 to 2016. Spatial analysis of actual and normalized damage as well as a supplemental assessment of three major disasters causing extensive damage in Texas (Hurricanes Carla 1961, Hurricane Alicia 1983, and Hurricane Ike 2008) highlight the risk as a function of wind or flooding damage and the growth of exposure in hazard prone regions.

## 2. Study Area

Texas is the second largest state in the United States by population and area, with a population of 27,862,596 and a land area of 695,662 $km^2$. The southeast of Texas shares 591 km (367 miles) of coastline with the Gulf of Mexico and is susceptible to hurricanes and coastal flooding. A major topographical feature that affects weather disasters in Texas is the Balcones Escarpment that consists of a series of cliffs dropping from the Edwards Plateau to the Balcones Fault Line. This outer rim of the Hill Country is the formation point for many large thunderstorms, which frequently stall along the uplift and then hover over the region for prolonged rainfall. This flood prone region is known as "Flash Flood Alley" and includes counties having the fastest population growth rates in Texas [11].

Texas is the fastest growing state in the country by actual population and the fifth fastest by percentage. Between 1940 and 2010, Texas averaged 21.6% rate of growth per decade, compared to 13.3% for the U.S. Based on a conference presentation in 2013 by the Texas State Demographer's Office, the overall population is projected to increase to 55 million by 2050 assuming a continuation of the 2000–2010 migration pattern The split between the rural and the urban share of the population has experienced a complete reversal from 1910 to 2010 with nine out of ten Texans living in one of the state's 25 metropolitan areas and nearly two out of every three Texans living in Dallas-Fort Worth, Houston, Austin or San Antonio. Much of this growth is occurring within regions having high risk of hydrometeorological disasters such as hurricanes and flooding along the Texas Gulf Coast (e.g., Houston metropolitan area). Texas doubled the national job growth percentage in 2012 at 2.7% which translates to higher income and wealth exposure in preferred coastal regions of the state [12].

## 3. Data Sources

The primary source of property damage data is the Spatial Hazard Evaluation and Losses Database for the United States (SHELDUS) maintained by the Center for Emergency Management and Homeland Security at Arizona State University [13]. The database aggregates hazard losses across 18 different disaster categories. In Texas, the relevant disaster types are reduced to 15 with the omission of earthquakes, tsunamis, and volcanoes. SHELDUS losses are based on information from the National Centers for Environmental Information (NCEI, formerly the National Climatic Data Center, NCDC), the U.S. Geological Survey (USGS), and other credible sources. Building damage from the disaster case studies is generated from the HAZUS-MH hazard analysis model developed by the Federal Emergency Management Agency (FEMA) that contains detailed sociodemographic data for residences based on the 2010 census and Dun and Bradstreet data for commercial buildings [14]. The HAZUS hurricane model simulates the entire storm track with a series of engineering-based models and multiple nationwide inventory databases to develop damage and loss functions. The sub-models in the HAZUS hurricane model include a storm track model, a wind field model, a wind load model, a windborne debris model, a physical damage model, and building loss models [15,16]. The HAZUS hurricane model provides estimates of building damage and content losses and income-related business interruption due to the impact of wind damage to the infrastructure. The HAZUS model is a conservative estimate as noted by previous analytical comparisons [17–19].

## 4. Methodology

This study defines a hazard as a natural event that has the potential to cause harm and a disaster as the effect of the hazard on a community. Hydrometeorological disasters are defined as natural processes or phenomena of atmospheric, hydrological or oceanographic nature [20]. The analysis of annual distribution of damage for the entire state over the 57-year period (1960–2016) includes adjusted damage ($2016) and damage normalized by population and GDP. Before 1997, the basis of GDP was the Standard Industrial Classification (SIC). It transitioned from SIC to the North American Industry Classification System (NAICS) in 1997 resulting in two different GDP values for that year. The arithmetic average of the 1997 SIC GDP and 1997 NAICS GDP was used as the 1997 GDP in the analysis. The effect of population and GDP was also analyzed across metropolitan statistical areas (MSA) for the period (2001–2016) in which NAICS-based GDP data were available.

Normalization of the property damage provides an indication of the relationship between the damage, regional wealth, and population over time. The method used can be based on national adjustment factors as described by Pielke et al., in which the combined effects of inflation, wealth, and population were considered to adjust damage in the year occurrence to the perceived damage in the base year [7]. Wealth adjustment factor can be based on a number of metrics available through the U.S. Bureau of Economic Analysis (BEA) including Net Stock of Fixed Assets and Consumer Durable Goods or Gross Domestic Product (GDP). The current study used regional GDP made available by the USBEA by metropolitan statistical areas (MSA) as the wealth adjustment factor to normalize the damage trends. Normalization per capita was based on median population of either county or MSA with respect to the period analyzed.

Spearman's rho and kendall's tau were used for non-parametric correlation analysis to determine the statistical significance of property damage trends over time since both methods are conducive to environmental forensics but each has advantages and disadvantage. Spearman's rho is more sensitive to error and better for larger sample size and kendall's tau is less sensitive to error and more appropriate for smaller sample size [21]. Ranking of linear strength in the positive direction was selected based on general guidelines of correlation analysis: <0.3 (weak), 0.3–0.5 (moderate), and >0.5 (strong) with a similar opposite ranking for negative trends with a statistically significance based on a 5% significance level [22,23]. Quantitative boundaries for linear strength relationships were not adjusted for specific environmental forensics since the significance level represented by the $p$-value was the critical identifier of significance related for the analysis. The $p$-values associated with the correlation less than 0.05 were considered statistically significant with smaller $p$-values representing greater statistical significance.

## 5. Results

All property damage used in the historic trend analysis was inflation adjusted to $2016 unless otherwise specified as actual property damage in year of occurrence. Natural disasters caused more than $725 billion in property damage in the U.S. during 1960–2016 in which 8% ($54.2 billion) was due to Texas property damage. Convective storms such as thunderstorms, heavy precipitation, tornadoes and strong straight-line winds that cause extreme directional wind or object forces (hail), appear to result in a disproportionate amount of damage. Fifty-eight percent ($424 billion) of the total property damage in the U.S. was due to convective storm disasters. Texas property damage due to convective storm disasters accounted for 80% ($43 billion) of the total property damage. Hurricanes and tropical storms caused the greatest property damage in the U.S. and in Texas at 36% and 34% of their respective total property damage. Texas property damage was a significant percentage of the national property damage with hail accounting for 33%, followed by coastal property damage at 32% and drought damage at 28% (Table 1). In addition to the total extent of the property damage observed during the 57-year period, the current study analyzed temporal distribution of damage which indicated a distinct increasing annual trend as well as seasonal variation that may reflect some influence of climate change. As suggested by Sander et al., the changes in meteorological potential for severe thunderstorms driven

by changes in the humidity of the troposphere (rise of humidity in the air over the last decades can be attributed to warming oceans and increased evaporation from their surfaces) may be contributing to the increase in hurricane winds and rainfall [5]. This increase in magnitude coupled with the increase in exposure will continue to result in escalating property damage particularly along hurricane prone regions.

**Table 1.** Total property damage caused by natural disasters in U.S. and Texas (1960–2016).

| Disaster Type | TX ($2016) | US ($2016) |
|---|---|---|
| Hurricane/Trop Strm | 18,325,926,908 | 258,877,397,419 |
| Hail | 12,301,331,729 | 37,295,600,013 |
| Flooding | 7,035,494,246 | 152,447,938,320 |
| Severe /TStrm | 6,298,129,432 | 35,434,257,137 |
| Tornado | 4,103,255,471 | 58,871,799,205 |
| Wind | 2,095,538,316 | 33,335,423,825 |
| Drought | 1,454,769,396 | 5,121,265,940 |
| Coastal | 940,709,789 | 2,955,956,179 |
| Winter Weather | 795,182,868 | 26,391,427,257 |
| Wildfire | 692,696,316 | 22,497,632,949 |
| Lightning | 159,383,681 | 3,101,409,332 |
| Fog | 6,885,490 | 58,142,521 |
| Heat | 1,794,114 | 504,346,195 |
| Landslide | 179,521 | 18,864,695,667 |
| Avalanche | 1,064 | 30,299,599 |
| **Grand Total** | **54,211,278,340** | **655,787,591,561** |

*5.1. Annual Distribution of Damage*

The average annual property damage between 1960 and 2016 is $951,075,059 ($2016) with a significant increasing trend ($p$-value < 0.0001 at the 5% significance level) (Figure 1a). Major disaster events such as hurricanes, tropical storms, widespread flooding in 1980, 1983 (Alicia), 1996, 2001 (Allison), 2005, and 2008 (Ike) resulted in the high variability of actual property damage over the 57-year period (coefficient of variation (COV) = 1.65) that is reduced to COV = 1.38 after adjusting the property damage to 2016 U.S. dollars.

Adjusted property damage per capita has a significant positive trend suggesting that the inflation rate outpaced the population growth. Actual property damage per GDP displays a non-significant positive trend display increasing trends over time highlighting substantial growth of the economy specifically building exposure susceptible to damage. The coefficient of variation of the damage per capita over the study period is 1.22 and has a statistically significant increasing trend (spearman's $\rho$ = 0.4194, $p$-value = 0.0012) at the 5% significance level (Figure 1b). GDP appears to be a stronger contributor to the time series increase compared to population given the reduction in trend strength and significance (spearman's $\rho$ = 0.1906, $p$-value = 0.1555) at the 5% level (Figure 1c). A secondary verification of linear strength and significance using Kendall's tau reduced the linear strength but did not change the significance in either normalization trends, respectively (*kendall* $\tau$ = 0.2897, $p$-value = 0.0015 and *kendall* $\tau$ = 0.1278, $p$-value = 0.1621). Furthermore, GDP normalization of damage results in the greatest reduction in variability (COV = 1.13).

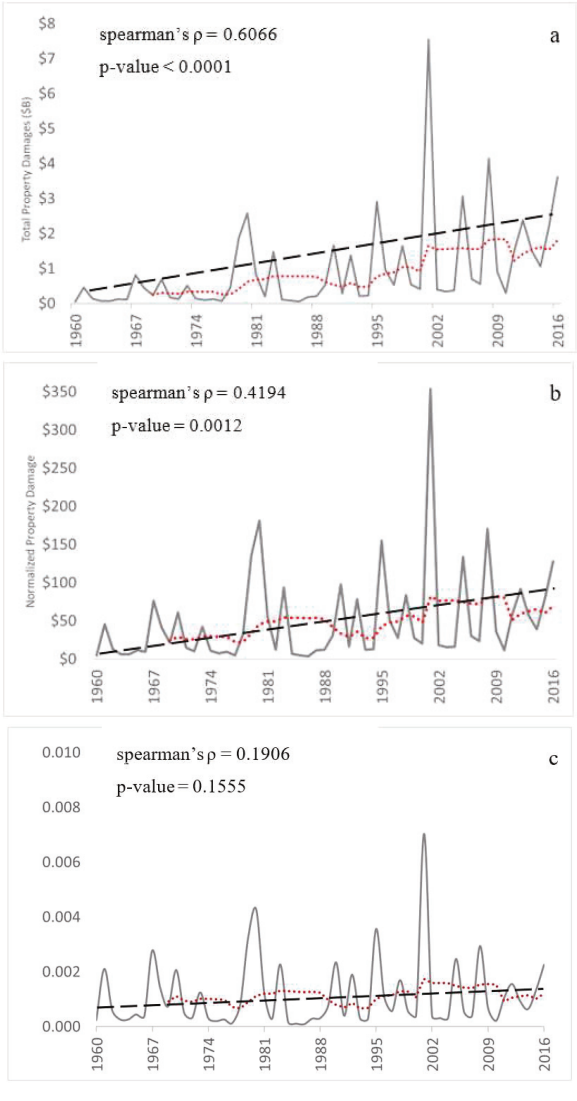


**Figure 1.** (**a**) Adj property damage caused by natural disasters in Texas (1960–2016); (**b**) Adj property damage per capita; and (**c**) Actual property damage by GDP. *Notation: 10-year moving average (red dots) and linear trend (black dash).*

### *5.2. Monthly Distribution of Damage*

Monthly distribution of damage highlights a significant difference between damages incurring in Winter and those incurring in the other seasons. The winter months (December, January, and February) account for only 5% of the total damages. Spring is the costliest season (March, April, and May) accounting for 36% of the total damages followed by summer (34%) and fall (25%). The monthly analysis of property damage suggests that the property damage is in sync with the North American hurricane season. A tri-modal distribution with peaks in April, June, and October can be observed

in Figure 2. Hail was the predominant cause of damage in April and hurricanes/tropical storms the dominant contributor to damage in June and September.

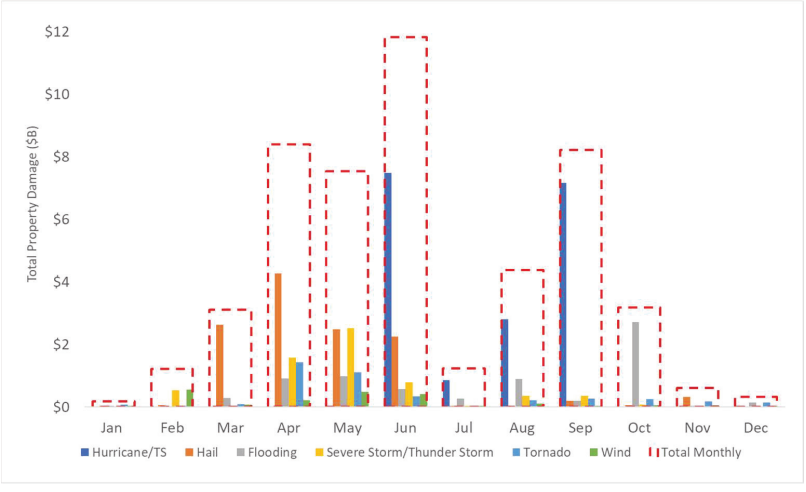


**Figure 2.** Top 6 disaster types monthly distribution of property damage (1960–2016).

Approximately 93% of the total property damage during 1960–2016 was caused by six of the 13 disaster types listed in Table 1. Monthly stratification of property damages caused by the hydrometeorological disasters shows that hurricane and tropical storms are the leading cause in four of the 12 months (June, July, August, and September). Hail damage is the leading cause of property damage in the months of March, April, May, and November. Flooding damage is highest in October. Hail, severe/thunderstorms, tornado, and wind overlap from February to June indicating the favorable seasonal conditions for storms that have intense wind and hail characteristics. The total damage for this period was $24.8 billion in property damage (46% of total). The bimodal annual characteristic of damage due to hurricanes and tropical storms is highlighted as well peaking in June and September when meteorological conditions are most favorable. The N.A. Atlantic hurricane season is 1 June–30 November and is closely aligned with the monthly damage totals suggesting a relationship between hurricanes and flooding. Flooding damage begins at the end of the June (peak hurricane month) and spikes in October toward the end of hurricane season which is likely a result of saturated conditions due to the cumulative amount of precipitation throughout the hurricane season.

### *5.3. Regional Normalized Trends and Spatial Distribution of Damage*

Additional analysis of damage and risk to property as a result of natural disasters included groupings of counties known as metropolitan statistical areas (MSAs). The MSAs are currently the lowest level in which the U.S. BEA maintains GDP data. County level GDP is not yet available but is under development [24]. The MSAs represent economic subdivisions in which the wealth measured as GDP for each county within the MSA is combined and represented as the total GDP for the MSA. In Texas from 2001 to 2016, 18 of the 25 MSAs had greater average annual increase in GDP than the U.S. annual average (4.8%). The Texas MSAs with the highest relative GDP are centralized around the major cities of Houston, Dallas/Ft. Worth, San Antonio, Austin, and El Paso.

The limited time study of 16 years is not a large sample size, but can provide high-level perspectives on the effects of wealth on property damage across the geographically dispersed MSAs. Actual property damage normalized by the GDP for the MSAs follow increasing trends similar to the statewide annual trends (1960–2016) for 44% of the MSAs. Fourteen of the 25 Texas MSAs exhibited

non-significant decreasing but trends at the 5% significance level and 11 MSAs exhibited increasing trend in property damage with only the Dallas MSA indicating a strong linear relationship and statistically significant trend ($\rho$ = 0.8176, $p$-value = 0.0001). The Dallas and Houston MSAs had very similar total and annual average GDP yet had opposite trends suggesting that there is a significant difference in the periodicity of major damaging events over the 16-year period between the two regions. Dallas is an inland region that is prone to tornado and hail damage which caused almost all reported property damage in 2012 and 2016, while the property damage to the Houston regions is primarily due to hurricane winds and related flooding. The non-significant decreasing trend for the Houston coastal region reflects the extreme damage and irregular occurrence of hurricanes specifically in 2001 (TS Allison) and 2008 (Hurricane Ike) resulting in an inconsistent linear trend, while the tornado and hail damage events in the Dallas region are more frequent and continuous resulting in increasing in property damage due to increasing exposure.

Spatial comparison of property damage ($2016) for the period 1960–2016 shows regional differences in Texas with higher property damage concentrated in counties with high population and urban development. Not surprisingly, the regional density of property damage due to natural disasters is clustered around the four largest metropolitan areas (Houston, Dallas, Austin, and San Antonio) and is also in alignment with the raw fatality densities discussed in previous research [9,10]. This is expected since an area of greater property exposure is more susceptible to higher damage during a natural disaster event. Considering the property damage per capita and per GDP as the wealth indicator provides a closer look of the relationship of damage and exposure.

Distinct counties of high property damage without adjustment for population or wealth normalization over the 57-year period is depicted in Figure 3 (Left). The counties with the highest overall property damage were Harris, Dallas, Tarrant, Bexar, and Lubbock. Other than Lubbock, the counties with highest damage are counties with high population and wealth. Lubbock is unique in that, even though it is not a large urban center with high wealth, the county is affected by frequent damage due to multiple types of disaster, mostly hail, wind, severe storms, flooding, and tornados, that span over seasonal changes resulting in higher overall damages. Counties in coastal Texas and the "Flash Flood Alley" region show higher damage losses.

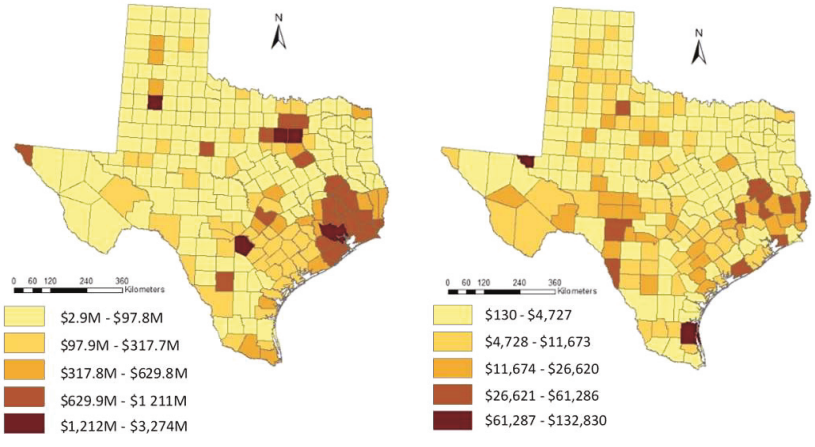


**Figure 3.** Spatial distribution of property damage ($2016) by Texas county (1960–2016): (**Left**) total property damage; and (**Right**) total property damage per capita.

Normalizing the property damage by median population (1988) reveals that the most affected counties with highly urbanized counties have below average normalized damage (Figure 3, Right). The most significant effect of this normalization is observed in the counties surrounding the Houston

and Dallas metropolitan areas which have a much lower per capita damage due to the high population density in the counties compared to counties near the Gulf coast, along the southern edge of the Balcones Escarpment in north Texas, and other sparsely populated counties.

As noted previously, the effect of population and wealth on property damage cannot currently be evaluated at the county level since the lowest level of sub-state GDP data is at the MSA level. The total adjusted property damage ($2016) and total GDP for all MSAs during 2001–2016 was $30 billion and $19 trillion, respectively. The Houston and Dallas MSAs had the highest total GDP by a large margin (four times that of the Austin MSA or San Antonio MSA). The average *adjusted* property damage per capita highlights the regions of relatively high property damage with low population increase over the 16-year period. Normalized *actual* property damage by GDP highlights the regions (MSA) with relatively high property damage and lower GDP (Table 2).

**Table 2.** Normalized property damage and trend correlation for Texas MSAs (2001–2016). Ranked by decreasing linear trend strength.

| | 16-year Average | | 16-year Annual Trend | | | |
|---|---|---|---|---|---|---|
| **MSA—Actual/GDP** | **Adj PD/Capita** | **Act PD/GDP** | **Spearman** | ***p*** | **Kendall** | ***p*** |
| Dallas-Fort Worth-Arlington | $48.12 | 0.706 | 0.8176 | 0.0001 | 0.6500 | 0.0004 |
| Lubbock | $393.40 | 9.672 | 0.4853 | 0.0567 | 0.3667 | 0.0476 |
| Texarkana | $100.05 | 1.732 | 0.2796 | 0.2942 | 0.1757 | 0.3439 |
| McAllen-Edinburg-Mission | $27.87 | 1.262 | 0.2264 | 0.4364 | 0.1868 | 0.3520 |
| Tyler | $1.90 | 0.030 | 0.1319 | 0.6676 | 0.1026 | 0.6255 |
| El Paso | $57.66 | 1.741 | 0.0682 | 0.8020 | 0.0342 | 0.8558 |
| Austin-Round Rock | $43.82 | 0.727 | 0.0643 | 0.8199 | 0.0476 | 0.8046 |
| Corpus Christi | $25.53 | 0.583 | 0.0440 | 0.8866 | 0.0769 | 0.7143 |
| Killeen-Temple | $4.51 | 0.106 | 0.0382 | 0.8882 | 0.0000 | 1.0000 |
| Sherman-Denison | $39.40 | 1.212 | 0.0382 | 0.8882 | −0.0167 | 0.9283 |
| Longview | $10.99 | 0.229 | 0.0059 | 0.9827 | 0.0084 | 0.9640 |
| Laredo | $16.25 | 0.527 | −0.0604 | 0.8445 | 0.0000 | 1.0000 |
| San Angelo | $36.72 | 0.882 | −0.1273 | 0.7092 | −0.0909 | 0.6971 |
| Waco | $5.13 | 0.122 | −0.1471 | 0.5868 | −0.1167 | 0.5285 |
| Brownsville-Harlingen | $16.00 | 0.712 | −0.1729 | 0.5377 | −0.1409 | 0.4788 |
| San Antonio-New Braunfels | $44.83 | 0.956 | −0.2341 | 0.4010 | −0.2297 | 0.2344 |
| Amarillo | $221.04 | 4.698 | −0.2357 | 0.3977 | −0.1619 | 0.4002 |
| Houston-The Woodlands-Sugar Land | $69.44 | 1.034 | −0.2634 | 0.3242 | −0.1925 | 0.2999 |
| Odessa | $5.41 | 0.117 | −0.2813 | 0.2912 | −0.2017 | 0.2789 |
| Victoria | $2.32 | 0.055 | −0.3091 | 0.3848 | −0.3333 | 0.1797 |
| Beaumont-Port Arthur | $457.18 | 8.690 | −0.3176 | 0.2306 | −0.2667 | 0.1497 |
| College Station-Bryan, | $6.04 | 0.168 | −0.3370 | 0.2018 | −0.2427 | 0.1912 |
| Abilene | $194.88 | 4.499 | −0.3626 | 0.2026 | −0.2527 | 0.2080 |
| Wichita Falls | $14.09 | 0.261 | −0.4059 | 0.1188 | −0.2833 | 0.1258 |
| Midland | $91.18 | 0.693 | −0.4794 | 0.0706 | −0.3942 | 0.0420 |

* Green highlighted rows are decreasing trends.

More than 75% of the Texas MSAs exceeded the national average annual growth in GDP (4.8%) during 2001–2016. The highest annual growth in GDP was noted in the Odessa (10%), Midland (9.1%), Austin (8.9%), McAllen (8.3%), and Tyler (7.5%) MSAs. The top MSAs for total property damage in Texas were Houston ($5.6 billion), Dallas ($5.3 billion), Beaumont ($2.8 billion), Lubbock ($1.9 billion), and San Antonio ($1.6 billion). The regions with larger increases in average annual GDP suggest that these areas may have a higher risk of increased property damage in future disaster events. The GDP and property damage for each MSA clearly identifies the Houston and the Dallas MSAs as the wealthiest regions that also experienced the greatest property damage. Several of the MSAs in the western counties such as Amarillo, Lubbock, and El Paso have significantly lower GDP but relatively high property damage resulting in an appreciable normalized risk of economic loss (Figure 4, top).

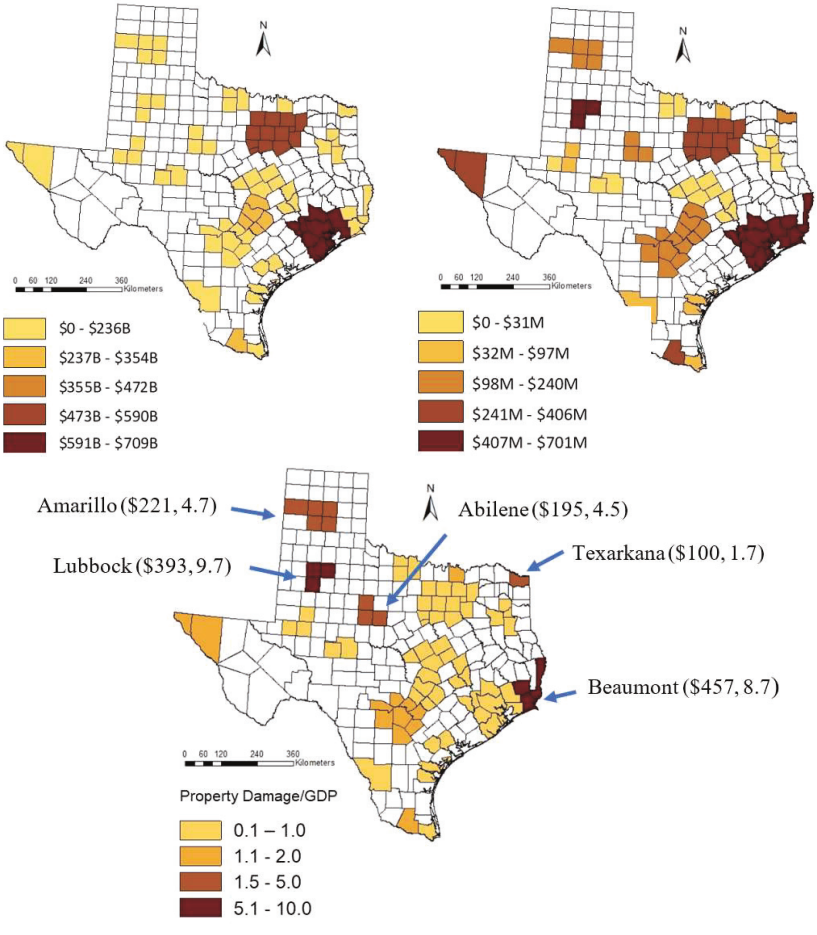


**Figure 4.** Spatial distribution of property damage for Texas MSAs (2001–2016): (**top left**) total GDP; (**top right**) total adjusted property damage; and (**bottom**) average actual property damage per capita and actual property damage by GDP ($\times 10^{-3}$).

The annual average adjusted property damage per capita and property damage normalized by GDP highlights regions of greater risk (Figure 4, bottom). The lower populations and relative wealth of these types of regions such as Lubbock (290,805/$171 billion), Beaumont (403,190/$324 billion), Abilene (165,252/$95 billion), and Amarillo (251,933/$172 billion) can create a greater critical need for assistance after a major disaster given their respective historic property damage ($1.9 billion, $2.8 billion, $524 million, and $860 million, respectively) and their limited resources compared to more urbanized regions.

*5.4. Detailed Event Damage*

The preceding review of historic damage estimates provides an assessment of damage trends, regional wealth diversity, and the relative impacts of different types of disasters on regions with different economic status. The damage estimates were culled from the SHLEDUS database that only includes direct property damage estimates adjusted to 2016 U.S. dollars. Natural disasters are difficult to categorize since the disaster types can overlap. In the current study, SHELDUS differentiates

damage caused between hurricanes, severe thunderstorms, hail, flooding, and tornados among other categories. However, in reality, the damage due to a major natural disaster such as a hurricane will be a combination of the hurricane high winds, the extreme rainfall, possible hail, and the subsequent flooding. Additionally, hurricanes sometimes spawn tornados that cause extensive damage which may or may not be attributed to the original hurricane. It can be of value to model specific disaster types in a specific region of known economic wealth to obtain additional details of the damage across specific types of damage and types of property and disruption to the economy such as transport, communication, utilities, and displacement costs can provide perspective to benefit the development of risk mitigation strategies.

Extensive research and development are ongoing to develop or improve simulation and prediction modelling systems in the field of natural disasters. A paper published and presented at the 4th International Conference on Emerging Ubiquitous Systems and Pervasive Networks highlights the development emphasis with focus on an agent-based methodological framework that allows for customizable desired observables [25]. Researchers at the NOAA Geophysical Fluid Dynamics Laboratory are currently in the process of enhancing the predictability of major weather events by replacing existing models with new generation prediction model known as the FV3 [26]. Disaster modeling is also a critical component in emergency management that facilitates response planning and prioritization of resources based on predicted aftermath of a major disaster. FEMA has developed the HAZUS-MH Multi-hazard damage estimation tool which allows for modeling of known historic or probabilistic disaster events in any region of the U.S. to facilitate the estimation of property damage, business and infrastructure interruption in a user-defined region and 2010 building exposure and population [27].

The assessment of the historic hurricane damage during 1960–2016 highlighted the changes to specific types of infrastructure damage based on growth in population and development. The damage and loss information generated by HAZUS is a snapshot of the types of damage that can be caused by a hurricane to different types of building, facilities, and utility systems and can be used as a risk assessment surrogate for other regions. HAZUS-MH (v.4.0) was used to model the specific damages that resulted from three historical hurricanes but using 2010 population, building and infrastructure exposure based on the regional Level 1 inventory imbedded in Hazus model with the output adjusted to 2014 exposure valuation. Hurricane Carla made landfall in 1961, Alicia made landfall in 1983, and Hurricane Ike made landfall in 2008. The total economic losses output from HAZUS also includes cost of business interruption such as lost wages and, displacement costs. The modeled hurricanes are representative of major storm events that caused at least 80% of all property damage in Texas in the year of occurrence. The counties included in the simulation were those in the immediate vicinity of landfall for the hurricanes since they have the greatest potential for damage due to high winds which is the main contributor to building damage. These counties are also representative of the types of building and infrastructure given the population and extent of economic development of the region. Results of the current study indicate that hurricanes caused the greatest percentage of total economic losses in Texas with each event representing the majority of damage in the given year. Three hurricanes occurring 22 years and 25 years apart were simulated to provide insight into the relative risk and economic loss across building types as well as show the variation in damage estimates as a function of wind damage, flood damage, regional development, and data source variation. The storm tracks and residential exposure for the three hurricanes generated by the Hazus hurricane model are depicted in Figure 5.

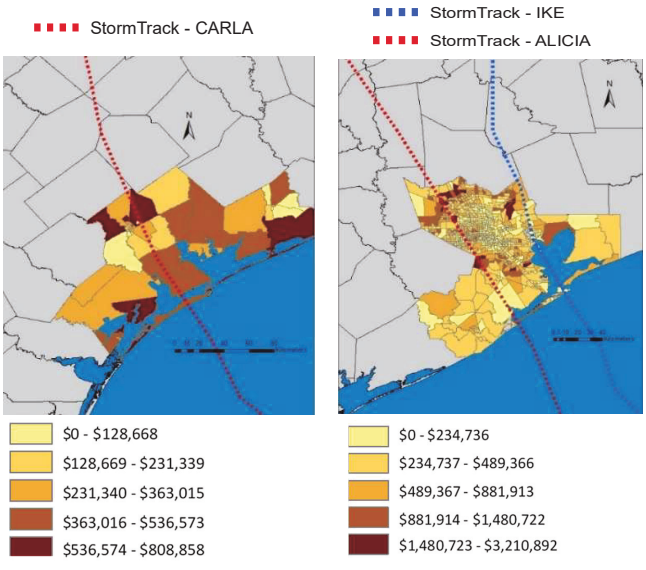


**Figure 5.** Storm tracks and residential (single-family) building exposure (2014): (**Left**) Hurricane Carla; and (**Right**) Hurricanes Alicia and Ike.

5.4.1. Hurricane Carla (2014 U.S. dollars)

Hurricane Carla made landfall on 11 September 1961 near Port O'Connor as a Category-5 hurricane but weakened quickly as it moved further inland in a northerly direction. Carla brought only small amounts of precipitation (3.15 in (80 mm)), but very strong wind gusts as high as 170 mph (280 km/h) in Port Lavaca. Since Hurricane Carla made landfall in proximity to Port O Conner (Calhoun county), the region selected for the model consisted of six counties in the immediate impact zone (Aransas, Calhoun, Jackson, Matagorda, Refugio, and Victoria) which is an area of 4468 square miles (11,572 $km^2$), and with 2010 census has 86,470 buildings, 71,000 households and a population of 189,492. Ninety-three percent of buildings and 80% ($17.1 billion) of the total building value are designated as residential. Commercial buildings comprise the majority (10.6%) of the non-residential buildings in the region. Essential facilities include 10 hospitals with a total bed capacity of 989 beds, 100 schools, 35 fire stations, 22 police stations, and no emergency operation facilities.

The model simulation of Hurricane Carla making landfall in 2010 at the same proximate location resulted in a total economic loss (property damage and business interruption) of $796 million representing 3.9 % of the total replacement value ($20.6 billion) of the region's buildings. The total losses consist of 85% direct property damage ($679 million) with the remaining 15% losses due to business interruption losses which include the inability to operate a business and temporary living expenses for those people displaced from their homes. The largest loss (both for property damage and business interruption loss) was sustained by the residential occupancies which made up over 86% of the total losses across all building types. The residential homes are primarily wood framed structures at an average cost of $213,207 per home. Seven percent of all wood structures would incur at least moderate damage.

5.4.2. Hurricane Alicia (2014 U.S. dollars)

Hurricane Alicia made landfall in August 1983 at Galveston Island as a Category-3 hurricane, with sustained winds of 100 mph (161 km/h) and gusts up to 127 mph (204 km/h). Alicia was not a particularly strong hurricane, but the area of maximum winds crossed a large metropolitan area

(Galveston-Houston) with a majority of the structural damage caused by high winds. The region selected for Model simulation included Brazoria, Chambers, Galveston, and Harris counties, an area of 4237 square miles (10,974 $km^2$), 1,435,808 buildings, 1,662,000 households and a population of 4,732,030 people. Ninety-one percent of buildings and 80% ($417.7 billion) of the total building value is designated as residential. Commercial buildings comprise the majority of non-residential buildings in the region. Essential facilities in HAZUS simulation include 76 hospitals with a total bed capacity of 15,898 beds, 1546 schools, 95 fire stations, 135 police stations and 11 emergency operation facilities.

The model simulation of Hurricane Alicia making landfall in 2010 at the same proximate location resulted in a total economic loss of $11.4 billion representing 2.2% of the total replacement value ($522 billion) of the area's buildings. The total losses consist of 89% direct property damage ($10.2 billion) with the remaining 11% losses due to business interruption losses. The largest loss (both for property damage and business interruption loss) was sustained by the residential occupancies which made up over 89% of the total losses across all building types. The residential homes are primarily wood framed structures at an average cost of $318,547 per home. Three percent of all wood structures would incur, at least, moderate damage.

#### 5.4.3. Hurricane Ike (2014 U.S. dollars)

Hurricane Ike made landfall near the city of Galveston on 13 September 2008 as a strong Category-2 storm with a central pressure of 951.6 millibars and maximum sustained winds of 110 mph (177 km/h). Hurricane Ike differs from the two previous case studies in that more than 50% of the total damage was due to storm surge in coastal Galveston, Harris, and Chambers counties, whereas wind was the primary cause of damage in Hurricanes Carla and Alicia. Since Hurricane Ike made landfall in very close proximity to where Alicia made landfall, the same four county (Brazoria, Chambers, Galveston, Harris) area was selected for HAZUS simulation with geographical specifications and property exposure count and value.

The model simulation of Hurricane Ike making landfall in 2010 at the same proximate location resulted in a total economic loss is $7.2 billion representing 1.4% of the total replacement value of the region's buildings. The total losses consist of 91% direct property damage ($6.5 billion) with the remaining 9% losses due to business interruption losses. The largest loss (both for property damage and business interruption loss) was sustained by the residential occupancies which made up over 90% of the total losses across all building types. As was the case with Hurricane Alicia, the residential homes in the selected region are primarily wood framed structures at an average cost of $318,547 per home. Slightly less than 2% of all wood structures would incur, at least, moderate damage.

#### 5.4.4. Variability and Limitations in Damage Estimates

The model damage estimates for the three hurricanes were adjusted from 2014 to 2016 US dollars to allow for comparison with each other and to other sources. The variability between the damage estimates provides some insight into the primary cause of damage (wind or flood), the level of property exposure in the modeled region, and the limitations of the modeling tool and database information used in the study (Table 3).

**Table 3.** Comparison of damage estimates for Hurricane Carla, Hurricane Alicia, and Hurricane Ike (*all dollar values adjusted to 2016 U.S. dollars*).

| Disaster Event Name | Hurricane Carla | Hurricane Alicia | Hurricane Ike |
|---|---|---|---|
| Month/Days | September 8–14 | August 15–21 | September 11–12 |
| Saffir-Simpson Classification | Cat-5 | Cat-3 | Cat-2 |
| Year | 1961 | 1983 | 2008 |
| Landfall | Port O'Connor, Tx | Galveston, Tx | |
| Primary Cause of Damage | Wind/Storm Surge | Wind/Tornadoes | Flooding |
| Texas Almanac (total damage) | $2.4 billion | $7.2 billion | $15.6 billion |
| NWS/NOAA (total damage) | NA | $7.3 billion | $33.4 billion |
| SHELDUS (property damage) | $204.4 million | $1.23 billion | $3.8 billion |
| SHELDUS (crop damage) | $204.4 million | $1.23 billion | NA |
| HAZUS model counties | Aransas, Calhoun, Jackson, Matagorda, Refugio, Victoria | Brazoria, Chambers, Galveston, Harris | |
| Counties population (2010) | 189,492 | 4,732,030 | |
| Hazus model (2010 building exposure) | $20.9 billion (80% wood residential) | $529 billion (80% wood residential) | |
| Hazus model (property damage) | $689 million | $10.3 billion | $6.63 billion |
| Hazus model (business interruption) | $119 million | $1.23 billion | $697 million |

First, even though all three of the historic disasters modeled were hurricanes, the type and extent of damage varies widely depending on the specific characteristics of the hurricane such as wind velocity, storm surge, and rainfall induced flooding. The HAZUS Hurricane model used in this study only calculates damages caused by the high winds recorded in the historic disaster parameter database. Hazus also has developed a Flood Model that could be used in conjunction with the Hurricane Model to aggregate damage estimates from both disaster types for the same region. This was not done in the current study since comprehensive damage prediction is not a focal point of the paper.

Secondly, the damage estimates are based on internal algorithms of structural design directly dependent on the types and number of structures are in the hurricane storm track. This structural inventory will vary depending on the selected region (one or more counties) and the level of urban development in these counties which increases with time in regions with population and GDP growth such as Texas. Since the model only analyzes wind damage across the user-defined subset of counties created for the model, the true actual damage across all regions affected by the storm track will always be greater.

Thirdly, the level of urban development is a dynamic variable that is critical in generating robust economic loss as a function of property damage and business interruption. Damage due to disasters is usually reported in current year dollars and then updated as new information is received and adjusted to the later year inflation factor (CPI). The version of the Hazus modeling tool used in the current study is developed with a structure inventory database that is based on 2010 census for residential buildings and 2010 Dun and Bradstreet for commercial buildings considered a Level 1 inventory. The model has the capability to be updated with more precise and current building data that would enhance the accuracy of the damage, repair and replacement cost estimates. Comparing the modeled damage estimates for Hurricanes Carla, Alicia, and Ike to other sources exemplifies the potential variation that can be attributed to one or more of these discontinuities.

For comparison to the Carla simulation, a *SHELDUS* data query for all property and crop damage caused by hurricane/tropical storm, coastal, flooding, hail, and severe thunderstorms for all Texas counties in the month of September 1961 reports $205 million property damage and an equal loss for crop damage. The *Texas Almanac* archives document total property and crop damage for Carla at $2.4 billion which is similar to the *NWS* estimate of $2.6 billion in which 2/3 was property and 1/3 crop damage. Storm surge played a major role in the damage for this hurricane which is not capture in the Hazus model. The NWS reports 1915 homes and 983 businesses, farm buildings, and other buildings were completely destroyed. Major damage occurred to 7398 homes and 2601 businesses, farm buildings, and other buildings. Minor damage was reported to 43,325 homes and 13,506 businesses,

farm buildings and other buildings [28]. The Hazus model for Carla resulted in $688 million in property damage and $119 million in business interruption.

Similarly, for comparison to Alicia, a *SHELDUS* query for all property and crop damage caused by hurricane/tropical storm, coastal, flooding, hail, severe thunderstorms for all Texas counties in the month of August 1983 reports $1.2 billion in property damage and an equal loss for crop damage. The *Texas Almanac* archives report total property and crop damage for Alicia at $7.2 billion which is similar to the *NOAA* estimate of $7.3 billion. A report by the NRC Committee on Natural Disasters published in 1983 reported $602 million in economic loss for Galveston, Harris, Brazoria, and Chambers with about 50% due to property damage and the other 50% damage due to roads, utilities, agriculture, marine, and vehicles. Alicia was a high wind damage hurricane that spawned at least 22 tornadoes resulting in an additional 18 fatalities and property damage [29]. The Hazus model for Alicia resulted in $10.3 billion in property damage and $1.23 billion in business interruption.

The difference in actual to model was most pronounced with Ike. A *SHELDUS* query for property and crop damage caused by hurricane/tropical storm, coastal, flooding, hail, and severe thunderstorms for all Texas counties in the month of September 2008 reports $3.76 billion in property damage. The *Texas Almanac* archives report $15.6 billion in the counties of Harris, Chambers, Galveston, Liberty, Polk, Matagorda, Brazoria, Fort Bend, San Jacinto, and Montgomery, with an estimated $8.9 billion of that due to storm surge in coastal Galveston, Harris, and Chambers counties. The NOAA reports a much higher value of $33.4 billion but include all counties in the storm track suggesting that much of the Ike damage was not in these Texas counties. The Hurricane Ike Impact Report published by the Office of Homeland Security Division of Emergency Management in 2008 breaks out the damage as follows: housing damage ($3.8 billion), infrastructure repairs ($2.7 billion), Public buildings ($1.9 billion), hospital damage ($791 million), and transportation ($147 million) [30]. The Hazus model for Ike resulted in $6.63 billion in property damage and $697 million in business interruption (Table 3).

**6. Discussion and Conclusions**

The spatiotemporal trends of annual damage caused by natural disasters in Texas highlight the disproportionate impact of hurricanes, tropical storms, and hail accounting for approximately 70% of total property damage during 1960–2016. The extreme susceptibility of coastal property damage due to hurricane is explicit in Texas (34% due to hurricanes) and supported by national damage statistics in which 40% of all U.S. property damage during this period is due to hurricane or tropical storms. Given the ongoing progress in scientific understanding of climate change and the record setting temperatures around the world in recent years being investigated and made public by several scientific NGOs as well as the International Panel on Climate Change (IPCC) [31], it is a natural tendency to gravitate to the assumption that the primary driver of our increasing disaster losses is due to the increase in frequency and intensity of hydrometeorological events. The change in disaster severity is generally increasing but the change in frequency remains an open debate. Conversely, the increase in property damage due the disasters is most definitely increasing and not debated. This suggests that the increase in damage is due to other factors outside the disaster itself such as the exposure, wealth and level of development of the regions with high risk of hurricane activity (e.g., coastal communities).

Annual distribution of property damage (2016 U.S. dollars) due to hydrometeorological disasters during the 57-year study period exhibited a statistically significant increasing trend with high annual variability that decreases when normalized per capita. Actual property damage (year of occurrence) normalized by annual GDP further decreases to a non-significant statistical positive trend suggesting a relationship of population and wealth to the level of damage in the impacted region. Additional inference of wealth effects on property damage is observed with trend analysis of the 25 Metropolitan Statistical Areas (MSA) in Texas during 2001–2016. Although a 16-year study period is limited in prediction value for trend analysis, it does provide some high-level results that highlight the differences in regional wealth in Texas. Actual property damage normalized by the GDP for each of the MSA regions property damage results in increasing trends similar to the statewide annual trends (1960–2016)

for 11 of the MSAs with only the Dallas MSA indicating a strong linear and significant correlation. Fourteen of the Texas MSAs exhibited non-significant decreasing trends based on non-parametric correlation analysis at a 5% significance level suggesting that growth in GDP is outpacing the actual property damage in those regions.

Simulation of three historic hurricanes using the HAZUS hurricane modeling estimation tool generated conservative estimates of total economic loss as expected given the limitation noted in Section 5.4.4. However, the simulation can be useful as a source of information for the types of buildings most susceptible to wind damage as well as an indirect indication of the number of counties impacted by the entire storm track. The model simulations provide a microcosm of lower level building level damage within one specific disaster event that may be representative of disaster damage that may occur in future disasters and therefore be useful as a loss predictor. The HAZUS modeling tool is designed and managed by FEMA to serve as a predictor of damage and resource disruption to aid emergency management personnel and is not intended to provide a precise account of the financial impact of a disaster. Within that context, the model output was substantially different from the total damage estimations produced by other sources that can provide perspective on the nature and extent of the modeled hurricanes.

Hurricane Carla made landfall at Galveston Island in 1961 and headed northwest into Harris county. Carla caused damage to many counties along its northeasterly track from Texas into the Great Lakes region resulting in $2.4–2.6 billion in total property and crop damage along its path (Texas Almanac and NWS). The SHELDUS aggregate data estimate for the entire month of September 1961 was $410 million and the Hazus simulation model using 2010 building inventory for six counties around the Texas landfall showed $688 million in property damage and $119 million in business interruption. The fact that the model output is higher than the other sources suggests that Carla was a combination of wind and water damage along the landfall counties due to storm surge and the building exposure has likely increased significantly from 1961 to 2010. Hurricane Alicia and Hurricane Ike made landfall within 40 km of each other around Galveston Island, albeit 25 years apart. These two hurricanes were drastically different in wind and rainfall which affected the type and location of damage. Alicia spawned at least 22 tornados causing excessive wind damage and Ike had heavy rainfall causing much more flood damage than wind damage. NOAA reported $7.3 billion in total damage for Alicia and $33.4 billion total damage for Ike which includes property and crops of all affected areas. SHELDUS data for the entire month of August 1983 indicated $2.4 billion (property and crop) and $3.8 billion (property) damage for September 2008. The Hazus simulation model (2010 inventory) was $11.5 billion (property damage and business interruption) for Alicia and $7.3 billion for Ike. In summary, both the Carla and Ike simulation models captured less than 50% of their respective estimates reported by other sources suggesting a broad geographical zone of damage with flood damage making a significant contribution. Conversely, the Alicia model damage estimates are 50% higher than total damage estimates reported at the time of occurrence by NOAA suggesting a substantial increase in building exposure in the modeled region that was damaged by high winds captured by the model.

In conclusion, it is apparent that damage estimates for historic disaster events can vary widely based on data source and methodology. Particularly in hurricane events where there is overlap in damage causality of wind, storm surge, and flooding, the estimates are very dependent on the categorization of the disaster type and the regions of impact. Deriving meaningful conclusions from historic data or simulation model data based on historic events should be tempered with the known limitations of the source data. For example, the damage reported by SHELDUS is spread out over the affected counties equally even if the event may have impacted one county disproportionately. In addition, prior to 1995, the database only reported an event that caused at least one death or over $50,000 in damage neglecting all smaller events [25]. Further research into historic property damage assessment may consider securing access to a level of SHELDUS data that is aggregated by disaster event and presidential disaster declaration to better relate the damage to the disaster. The hurricane

modeling used by the HAZUS-MH hurricane model only includes damage and losses caused directly and immediately by the hurricane wind. Moreover, the default building, infrastructure, and terrain data in HAZUS-MH is based on the best information available at the time of the application release which, at best, includes 2010 U.S. census for residential buildings and Dun and Bradstreet estimates for commercial buildings. The accuracy of HAZUS simulation output can be greatly increased by modeling the historic disaster of interest for wind, hail, and flooding in high risk areas and using advanced regional inventory, utility, transportation, and economic data. The noted constraints that limits the quantitative accuracy of the Hazus model output can be mitigated by: (1) Using multiple disaster models to account for damage due to wind and flooding when considering a hurricane event. (2) Upgrading the Level 1 building inventory and infrastructure database with user defined building files obtained from the property tax assessment agency and current hazard maps that provide accurate flood depth grids and boundaries and hurricane wind fields. (3) Building the model region to include as many counties as practical in the storm track.

**Author Contributions:** H.O.S. provided research supervision and professional guidance in all aspects of writing this paper. S.H.P. performed the data mining, quantitative analysis, qualitative interpretation and discussion, and is responsible for all content in this paper.

**Acknowledgments:** The authors thank David and Bethene Player for review of the manuscript and providing a sounding board for interdisciplinary perspective.

## References

1. Munich, R. NatCatSERVICE, Natural Catastrophe Know-how for Risk Management and Research. Natural Catastrophe Online Tool. Available online: http://natcatservice.munichre.com/ (accessed on 18 September 2018).
2. National Oceanic and Atmospheric Administration (NOAA). National Centers for Environmental Information. Storm Events Database 2017. Available online: https://www.ncdc.noaa.gov/billions/overview (accessed on 18 September 2018).
3. Irfan, U.; Resnick, B. Megadisasters Devastated America in 2017. And They're Only Going to Get Worse. Storms, Fires, Floods, and Heat Caused at Least $306 Billion in Destruction Last Year. 2018. Available online: https://www.vox.com/energy-and-environment/2017/12/28/16795490/natural-disasters-2017-hurricanes-wildfires-heat-climate-change-cost-deaths (accessed on 18 September 2018).
4. Gall, M.; Borden, K.A.; Emrich, C.T.; Cutter, S.L. The Unsustainable Trend of Natural Hazard Losses in the United States. *Sustainability* **2011**, *3*, 2157–2181. [CrossRef]
5. Sander, J.; Eichner, J.F.; Faust, E.; Steuer, M. Rising Variability in Thunderstorm-Related U.S. Losses as a Reflection of Changes in Large-Scale Thunderstorm Forcing. *Am. Meteorol. Soc.* **2013**. [CrossRef]
6. Pielke, R.A.; Landsea, C.W. Normalized Hurricane Damage in the United States: 1925–95. *Am. Meteorol. Soc.* **1998**, *13*, 621–631. [CrossRef]
7. Pielke, R.A.; Gratz, J.; Landsea, C.W.; Collins, D.; Saunders, M.A.; Musulin, R. Normalized Hurricane Damage in the United States: 1900–2005. *Nat. Hazards Rev. ASCE* **2008**, *9*. [CrossRef]
8. Klotzbach, P.J.; Bowen, S.G.; Pielke, R.A.; Bell, M. Continental U.S Hurricane Landfall Frequency and Associated Damage, Observations and Future Risks. *Am. Meteorol. Soc.* **2018**. [CrossRef]
9. Paul, S.; Sharif, H.; Crawford, A. Fatalities Caused by Hydrometeorological Disasters in Texas. *Geosciences* **2018**, *8*, 186. [CrossRef]
10. Sharif, H.; Jackson, T.; Hossain, M.; Zane, D. Analysis of Flood Fatalities in Texas. *Nat. Disasters Rev.* **2014**, *16*. [CrossRef]
11. Gaines, J.; Hunt, H. Tierra Grande. Housing Markets. Publication 2028. 2013. Available online: https://assets.recenter.tamu.edu/documents/articles/2028.pdf (accessed on 18 September 2018).

12. Potter, L. The Changing Population of Texas and West Texas. In Proceedings of the Cross Roads Healthcare Transformation in West Texas Conference, Lubbock, TX, USA, 5 June 2013; Office of State Demographer: Austin, TX, USA, 2013.
13. CEMHS. *Spatial Hazard Events and Losses Database for the United States, Version 16.1*; Center for Emergency Management and Homeland Security, Arizona State University: Phoenix, AZ, USA, 2018.
14. Schneider, P.; Schauer, B. Hazus-Its development and its future. *Nat. Hazards Rev.* **2006**, *7*, 40–44. [CrossRef]
15. Vickery, J.; Lin, J.; Skerlj, P.; Twisdale, L.; Huang, K. Hazus-MH hurricane model methodology I: Hurricane hazard, terrain, and wind load modeling." and "Hazus-MH hurricane model methodology II: Damage and loss estimation. *Nat. Hazards Rev.* **2006**, *7*, 82–93. [CrossRef]
16. Hahn, D.; Emmanuelle, V.; Ross, C. Multi-Hazard Mapping of the U.S. *J. Risk Uncertain. Eng. Syst. Part A Civ. Eng.* **2017**, *3*. [CrossRef]
17. Gordon, P.; Richardson, H.W.; Davis, B. Transport-related impacts of the Northridge earthquake. *J. Transp. Stat.* **1998**, *1*, 21–36.
18. Burrus, R.; Dumas, C.F.; Farrell, C.H.; Hall, W.W., Jr. Impact of low-intensity hurricanes on regional economic activity. *Nat. Hazards Rev.* **2002**, *3*, 118–125. [CrossRef]
19. Pan, Q. Case Study: Economic Losses from a Hypothetical Hurricane Event in the Houston-Galveston Area. *ASCE Nat. Hazards Rev.* **2011**, *12*, 146–155. [CrossRef]
20. Hydrometeorological Hazards. Disaster Risk Reduction. Natural Sciences. United Nations Education, Scientific, and Cultural Organization (UNESCO). Available online: http://www.unesco.org/new/en/natural-sciences/special-themes/disaster-risk-reduction/natural-hazards/hydro-meteorological-hazards/ (accessed on 18 September 2018).
21. Gautheir, T. Detecting Trends Using Spearman's Rank Correlation Coefficient. *Environ. Forensics* **2001**, *2*, 359–362. [CrossRef]
22. Wilson, L.T. Statistical Correlation. 2009. Available online: https://explorable.com/statistical-correlation (accessed on 8 October 2018).
23. Statistics Solutions, Complete Dissertation. Available online: https://www.statisticssolutions.com/kendalls-tau-and-spearmans-rank-correlation-coefficient/ (accessed on 8 October 2018).
24. Guci, L.; Mead, C.; Panek, S. A Research Agenda for Measuring GDP at the County Level, Bureau of Economic Analysis. 2016. Available online: https://www.bea.gov/system/files/papers/WP2016-4.pdf (accessed on 18 September 2018).
25. Mustapha, K.; Mcheick, H.; Mellouli, S. Modeling and Simulation Agent-Based of Natural Disaster Complex Systems. In Proceedings of the 4th International Conference on Emerging Ubiquitous Systems and Pervasive Networks (EUSPN-2013), Niagara Falls, ON, Canada, 21–24 October 2013.
26. FV3: Finite-Volume Cubed Sphere Dynamical Core, Geophysical Fluid Dynamics Laboratory (GFDL), Princeton University Forrestal Campus. Available online: https://www.gfdl.noaa.gov/fv3/ (accessed on 18 September 2018).
27. Federal Emergency Management Agency (FEMA). *U.S. Hazard Multi-hazard Estimation Tool, Hurricane Model*; HAZUS-MH 4.0; Federal Emergency Management Agency (FEMA): Washington, DC, USA, 2018.
28. National Weather Service (NWS). National Oceanic and Atmospheric Administration, Carla 50th Anniversary, Storm Summary. Available online: https://www.weather.gov/crp/hurricanecarla (accessed on 8 October 2018).
29. Savage, R.P. National Research Council (NRC), Committee on Natural Disasters, Commission on Engineering and Technical Systems. In *Hurricane Alicia: Galveston and Houston, TX, USA, 17–18 August 1983*; National Academy Press: Washington, DC, USA, 1984.
30. Colley, J.; DeBlasio, S.M. *Hurricane Ike Impact Report-December 2008*; Office of Homeland Security, Division of Emergency Management: Austin, TX, USA, 2008.
31. International Panel on Climate Change (IPPC). Summary for Policymakers of IPCC Special Report on Global Warming of 1.5°C Approved by Government. 2018. Available online: https://www.ipcc.ch/news_and_events/pr_181008_P48_spm.shtml (accessed on 8 October 2018).

# 2

# Simulating the Influence of Buildings on Flood Inundation in Urban Areas

**Riccardo Beretta [1], Giovanni Ravazzani [1,*], Carlo Maiorano [2] and Marco Mancini [1]**

[1] Politecnico di Milano, Piazza Leonardo da Vinci, 32, 20133 Milano, Italy; riccardo4.beretta@mail.polimi.it (R.B.); marco.mancini@polimi.it (M.M.)
[2] Modellistica e Monitoraggio Idrologico S.r.l, Via Ariberto 1, 20123 Milano, Italy; carlo.maiorano@mmidro.it
* Correspondence: giovanni.ravazzani@polimi.it

**Abstract:** Two-dimensional hydraulic modeling is fundamental to simulate flood events in urban area. Key factors to reach optimal results are detailed information about domain geometry and utility of hydrodynamic models to integrate the full or simplified Saint Venant equations in complex geometry. However, in some cases, detailed topographic datasets that represent the domain geometry are not available, so approximations—such as diffusive wave equation—is introduced whilst representing urban area with an adjusted roughness coefficient. In the present paper, different methods to represent buildings and approximation of the Saint Venant equations are tested by performing experiments on a scale physical model of urban district in laboratory. Simplified methods are tested for simulation of a real flood event which occurred in 2013 in the city of Olbia, Italy. Results show that accuracy of simulating flow depth with a detailed geometry is comparable to the one achieved with an adjusted roughness coefficient.

**Keywords:** urban topography; flood modeling; Saint Venant equations; laboratory experiment; buildings; roughness coefficient

## 1. Introduction

Flood events are one of the most dangerous natural phenomena connected to human activities, with possible consequences on people's safety and economic losses [1].

The flood hazard affecting densely populated areas is increasing in recent times, due to the intensification of extreme meteorological events and poorly managed urban development [2]. Two-dimensional flood inundation modeling is a pivotal component of flood risk assessment and management. It is therefore not surprising that over the last few decades significant efforts have been devoted to the development of increasingly complex algorithms to simulate the flow of water in streams and floodplains [3–10]. In areas with mild slope terrain, one-dimensional models may produce misleading results and two-dimensional (2D) models are recommended also for their ability to capture preferential flow directions caused by the presence of buildings [11,12].

The correct representation of buildings in a 2D model is a fundamental factor to reach good flood simulation results in urban areas. When detailed geometry is available, the individual shapes of buildings can be incorporated into the calculations. For large scale modeling or when detailed geometry information are not available, flow obstructions may be represented as areas with higher roughness coefficient (roughness approach). This accounts for the increased resistance induced by the presence of buildings in the urban area. Moreover, low accuracy of available topographic data justifies introducing some simplifications to the Saint Venant equations, also known as shallow water equations (SWE), that describe fluid dynamics [13–15]. In most practical applications of flood simulation, the diffusive wave simplification is preferred to the full solution (dynamic wave), since the local and convective acceleration terms are small in comparison to the bed slope [16].

In the last few decades, many aspects of urban flooding have been investigated through experimental studies [17,18], and few of these investigations have focused on how to properly represent buildings within inundation models [19,20].

The main objective of this paper is to verify the accuracy of the roughness approach against full buildings incorporation in flood simulation. Further analysis was dedicated to test diffusive model against full SVE. The novelty of this research is that three different methods to represent buildings are tested by performing a number of laboratory experiments carried out with a simplified urban district physical model, and reconstructing results with a hydraulic mathematical model considering both the solution of the full SWE and the diffusive simplification. Simplified methods are tested for simulation of a real flood event that hit the city of Olbia, Italy, on November 2013.

## 2. Materials and Methods

### *2.1. Experimental Setup*

Experiments were performed on a physical scale model at the Fantoli Hydraulic Laboratory at the Politecnico di Milano (Figure 1a). The model was implemented for verifying the hydraulic performance of the dam body of an on-stream detention basin designed for flood risk reduction of the Fosso di Pratolungo river, a small tributary of the river Aniene, in the Lazio region, Italy. Flow into the physical model is regulated by two triangular Thompson weirs, often used in laboratory experiments for their high sensitivity to low flow rates. The maximum flow rate achievable, is 110 L/s. The ratio between the physical model lengths and the prototype is 1:25. Specifically for this work, we considered the channel reach and floodplain downstream of the dam artifact (427 cm × 223 cm), where six bricks (12 cm × 25 cm) were placed for the representation of a small urban area with regular simple geometry (Figure 1c). An impermeable foam layer was attached to the lower side of the bricks in order to follow the irregularities of floodplain reproduced in the physical model (Figure 1b). A removable bridge was placed within the channel (Figure 1c) and the channel end was blocked with a board (Figure 1a) in order to promote floodplain inundation.

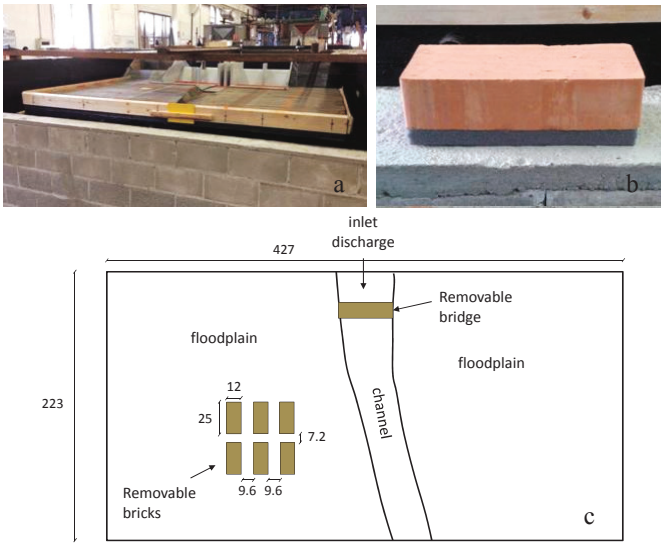


**Figure 1.** (**a**) Physical scale model of the dam body and the downstream floodplain; (**b**) brick with a layer of foam lining the lower side used to represent the urban area; (**c**) layout of the experimental setup denoting inlet discharge, channel, floodplain, and removable bridge and bricks (dimension in cm).

Water level and velocity were measured using a portable high precision nonius hydrometric rod and a micro-current-meter, respectively, in the points shown in Figure 2. The hydrometric rod was used to measure floodplain and channel bed elevation with a spatial resolution of 1 cm, leading to the digital elevation model shown in Figure 2.


**Figure 2.** Digital Elevation Model of the floodplain with the six bricks used to represent a simplified urban district and locations of points where measures were acquired, marked with letters from A to N.

*2.2. Mathematical Hydraulic Modelling*

In order to simulate the flood inundation, the Hec-Ras model was employed [21]. As from release 5.0, Hec-Ras is designed to simulate one-dimensional, two-dimensional, and combined one/two-dimensional unsteady flow through a full network of open channels, floodplains, and alluvial fans. For the purpose of this work, flood inundation was simulated with unsteady two-dimensional solution of the full SWE and the simplified diffusive equation. When a steady state was required, this was reached by setting as input a constant discharge hydrograph long enough to reach the steady condition.

Several methods have been proposed to set the friction coefficient when roughness approach is employed to simulate flow obstacles such as the equivalent friction slope method [22,23] or similar methods [24]. In this work, we chose to use roughness Manning coefficient reported in the Hec-Ras 2D manual [25] as this is what is likely done for practical engineering applications. Further analysis to verify possible improvement when using different approaches to set roughness coefficient is ongoing.

Buildings were modeled in three different ways:

1. Method 1: incorporation of buildings using the detailed digital elevation model (DEM) with 1 cm spatial resolution.
2. Method 2: buildings are replaced by a flat area with high roughness (Manning coefficient = 10).
3. Method 3: all urban area is replaced by a flat area with high roughness (Manning coefficient = 0.15).

The mean relative absolute error (MRAE) was computed as goodness of fit index

$$MRAE = \frac{\sum_{i=1}^{n} \left| X_{obs,i} - X_{mod,i} \right| / X_{obs,i}}{n} \quad (1)$$

where $X_{obs}$ and $X_{mod}$ are the observed and modeled values, respectively, $n$ is the number of points compared.

*2.3. Hydrologic Model*

Flood hydrograph of the six streams flowing to Olbia during the 2013 flood were simulated with the FEST model (flash-flood event-based spatially distributed rainfall-runoff transformation) [26–29]. FEST is

a distributed, raster-based hydrologic model developed focusing on flash-flood event simulation. As a distributed model, FEST can manage spatial distribution of meteorological forcings, and heterogeneity in hill slope and drainage network morphology (slope, roughness, etc.) and land use.

The FEST model has three principal components. In the first component, the flow path network is automatically derived from the digital elevation model using a least-cost path algorithm [30]. In the second component, the surface runoff is computed for each elementary cell using the SCS-CN method [31,32]. The third component performs the runoff routing throughout the hill slope and the river network through a diffusion wave scheme based on the Muskingum–Cunge method in its non-linear form with the time variable celerity [33]. Spatial resolution of input maps was 10 m.

*2.4. The 2013 Flood in Olbia*

Olbia is a flood-prone city located in Sardinia, Italy, that developed in an alluvial plain bounded on the West side by a steep mountains chain and on the East side by the Tyrrhenian Sea. Six creeks cross this area with drainage area ranging from 0.5 $km^2$ to 38.4 $km^2$ (Figure 3). A steep slope in the upper part and a mild slope in the valley where city mostly expanded characterize them.

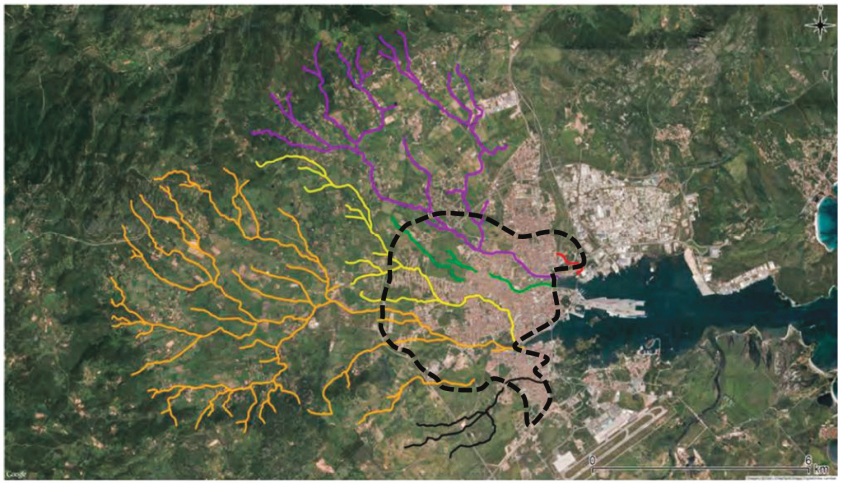

**Figure 3.** Creeks draining to the Olbia city center. Dashed line marks the study area where flood simulation has been conducted.

The peculiar morphology of the territory together with the urbanization pressure have contributed to transform a flood prone area into a high flood risk territory demonstrated by catastrophic floods that hit Olbia in 1970, 2013, and 2015.

Specifically, on 18 November 2013, the island of Sardinia (Italy) was affected by a meteorological event, named Cleopatra, characterized by extreme rainfall intensity (rain rate exceeded 120 mm/h in some localities), and amount (more than 450 mm of cumulated rainfall in 15 h) that sets the maximum return period of precipitation well above 200 years. Continuous rain over two days resulted in the overflowing of the rivers in the north-eastern part of Sardinia. Olbia was one of the affected cities of the island, with discharge values that reached the 25-year return period. Images and videos of the flood can be seen on the page dedicated by BBC to the Cleopatra cyclone affecting Sardinia (http://www.bbc.com/news/world-europe-24996292).

After the flood, the technical office of the Municipality carried out a survey of the flooded areas in the urban center of Olbia.

## 3. Results

### *3.1. Simulation of Flow Depth and Velocity of the Laboratory Experiments*

The first phase of experiments was dedicated to calibrate the Manning roughness coefficient of the channel and the floodplains. In this phase, bricks and bridge were removed from the physical model. Normal depth was set as boundary condition on domain border. The domain was implemented with a square mesh with 1 cm spatial resolution.

Measurements of the free-surface profile in the channel and over the floodplain for various flow rates (15, 18, and 21 L/s) were compared to values computed with Hec-Ras with different roughness coefficient. The roughness coefficient value that minimized the difference between measured and computed water profile was 0.0166 s $m^{-1/3}$, which is in consistent with the expected value for concrete.

In the second phase, the bricks and bridge were positioned in the model, and experiments were performed considering a constant flow rate of 22.6 L/s, discharged through the dam bottom spillway of the physical model. Flow depth and velocity measured values were compared to mathematical model simulation results obtained with the solution of the diffusive equation and considering the three methods for representing buildings described in Section 2.2. Simulated water levels and velocities are shown in Figures 4 and 5, respectively.

In Tables 1 and 2 observed and simulated water level and velocity, respectively, the 14 points monitored are reported. MRAE and standard deviation values computed between observed and simulated water levels and velocities are reported in Table 3. Errors related to water levels are lower than values calculated for water velocity; this is probably also justified by the relatively higher uncertainty intrinsically involved in the velocity measuring in very low water depth (indeed, in point I, it was not possible to get velocity measurement).

As a general comment, the three methods tested are all equivalent in simulating water depths, while Method 3 is not able to correctly capture water velocities within the area approximated with a homogeneous roughness coefficient. In fact, velocity computed inside the buildings (points E, F, G, H, J, and K) do not have a physical meaning when Method 3 is used. Method 3 is intended for considering effect of urban area on flood inundating surrounding places and not to investigate flow dynamics inside the urban area.

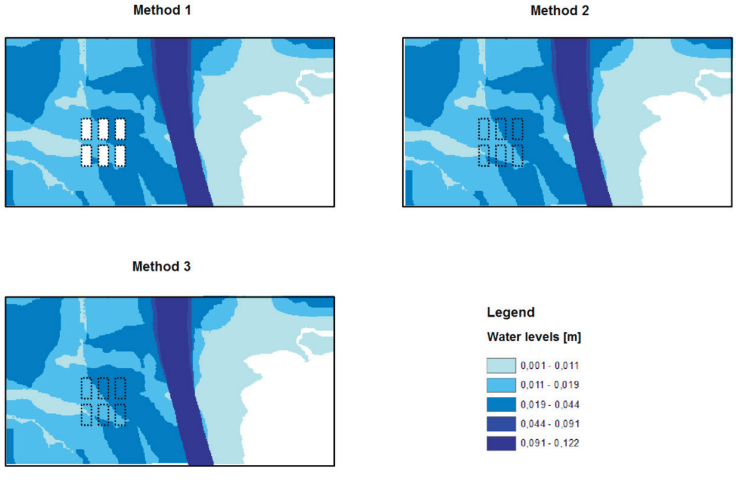


**Figure 4.** Water levels (m) on the laboratory model simulated with the three methods. The dashed lines denote brick locations.

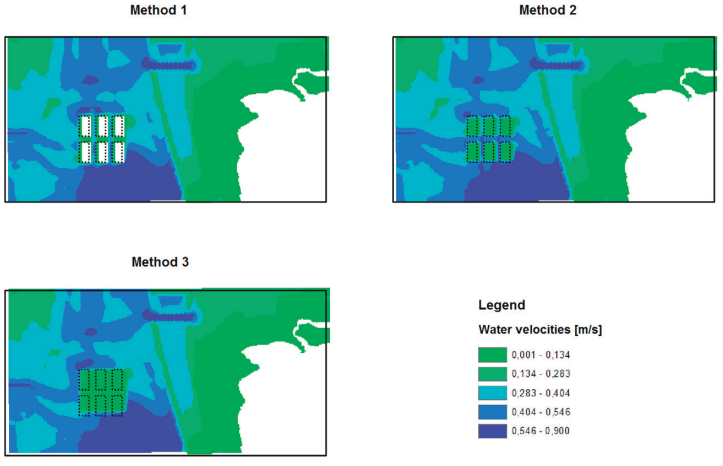


**Figure 5.** Water velocities on the laboratory model simulated with the three methods. Dashed lines denote brick locations.

**Table 1.** Observed and simulated water levels with Methods 1, 2, and 3.

| Point | Observed Water Level (m) | Simulated Water Level (m) | | |
|---|---|---|---|---|
| | | Method 1 | Method 2 | Method 3 |
| A | 0.014 | 0.009 | 0.009 | 0.009 |
| B | 0.022 | 0.014 | 0.013 | 0.014 |
| C | 0.022 | 0.016 | 0.016 | 0.016 |
| D | 0.044 | 0.024 | 0.023 | 0.024 |
| E | 0.015 | 0.019 | 0.019 | 0.019 |
| F | 0.021 | 0.021 | 0.021 | 0.022 |
| G | 0.016 | 0.018 | 0.019 | 0.019 |
| H | 0.024 | 0.022 | 0.021 | 0.022 |
| I | 0.011 | 0.008 | 0.009 | 0.009 |
| J | 0.010 | 0.014 | 0.014 | 0.014 |
| K | 0.017 | 0.018 | 0.018 | 0.018 |
| L | 0.040 | 0.023 | 0.022 | 0.022 |
| M | 0.019 | 0.019 | 0.019 | 0.019 |
| N | 0.044 | 0.027 | 0.026 | 0.026 |

**Table 2.** Observed and simulated water velocities with Methods 1, 2, and 3.

| Point | Observed Water Velocity (m/s) | Simulated Water Velocity (m/s) | | |
|---|---|---|---|---|
| | | Method 1 | Method 2 | Method 3 |
| A | 0.505 | 0.345 | 0.331 | 0.351 |
| B | 0.416 | 0.392 | 0.370 | 0.369 |
| C | 0.862 | 0.340 | 0.355 | 0.341 |
| D | 0.590 | 0.373 | 0.368 | 0.349 |
| E | 0.359 | 0.400 | 0.350 | 0.072 |
| F | 0.497 | 0.400 | 0.330 | 0.058 |
| G | 0.267 | 0.103 | 0.442 | 0.078 |
| H | 0.267 | 0.117 | 0.450 | 0.072 |
| I | NA | 0.412 | 0.459 | 0.440 |
| J | 0.382 | 0.490 | 0.530 | 0.086 |
| K | 0.566 | 0.550 | 0.550 | 0.092 |
| L | 0.673 | 0.526 | 0.515 | 0.546 |
| M | 0.244 | 0.390 | 0.416 | 0.432 |
| N | 0.659 | 0.700 | 0.680 | 0.687 |

Note: NA = measure was not possible.

**Table 3.** Mean relative absolute error, with standard deviation in brackets, for water level and velocity simulation with the three different methods.

| | Method 1 | Method 2 | Method 3 |
|---|---|---|---|
| Level | 0.248 (0.157) | 0.257 (0.161) | 0.252 (0.154) |
| Velocity | 0.309 (0.214) | 0.347 (0.244) | 0.551 (0.288) |

In Method 2 and 3, as buildings that are considered impervious in Method 1 are represented only with a different roughness coefficient, water is free to flow in the area occupied by buildings, although with velocities close to zero. While this does not represent an issue when performing constant flow rate simulations, it could introduce error in inundation volume when simulating unsteady flow transient condition with discharge changing over time.

For this reason, further simulations for Methods 1 and 2 were performed, considering two different triangular symmetric hydrographs characterized by the same peak discharge, and two different durations, 1 and 10 min (denoted H1 and H10, respectively), so to consider two hydrographs with different volume (Figure 6). Moreover, water flow was also simulated running full SWE, to evaluate possible differences against simplified diffusive scheme. As the laboratory model was not intended for reproducing unsteady hydrograph, in this test we could only compare simulated data. The goodness of fit indexes are to be interpreted as the deviation of Method 2 with respect to the Method 1 simulation. Water depth and velocity in points F, G, and J are considered in this analysis at 20, 40, and 60 s for H1, and 3, 6, and 10 min for H10.

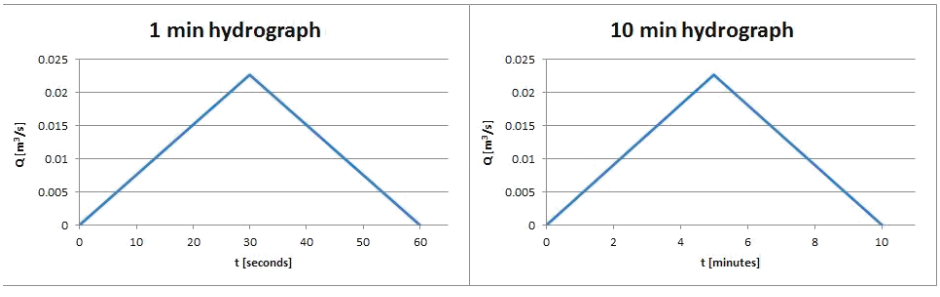


**Figure 6.** Hydrographs characterized by the same peak discharge, and two different durations, 1 and 10 min, used to run unsteady simulations.

The results shown in Table 4 confirm small differences between Methods 1 and 2 concerning water levels, especially using diffusive model, with a maximum deviation of 0.11 when full SWE are solved with H1. This confirms that the roughness approach and diffusive solution of SWE are good enough to simulate water depths even with unsteady flow hydrographs.

On the other hand, by analyzing water velocities, greater differences between Method 1 and 2 are reported for both the simulations, especially for the diffusive model.

**Table 4.** Mean relative absolute deviation of Method 2 respect to Method 1 in reconstructing water levels and velocities with 1 min (H1) and 10 min (H10) duration hydrographs.

| | Water Levels | | Water Velocities | |
|---|---|---|---|---|
| Simulation | Diffusive | Dynamic | Diffusive | Dynamic |
| H1 | 0.04 | 0.11 | 0.64 | 0.27 |
| H10 | 0.04 | 0.09 | 0.71 | 0.22 |

Finally, an advantage of the diffusive solution is that it is faster than full SWE; in particular, the simplified simulation took about 20% time less than the full solution on a laptop computer with 1.5 GHz CPU clock speed and 2 GB ram.

*3.2. Simulation of Olbia Flood Inundation*

Results presented in the previous section show that Methods 1 and 2 provide similar accuracy in simulating water depth and velocity in urban area. This is relevant when one flood event has to be simulated in an urban area for which detailed buildings geometry is not available. In order to validate these findings, the 2013 flood that occurred in Olbia was simulated with the assumptions of Method 2, that are 2D diffusive solution model and buildings represented with high roughness cells (Manning coefficient = 10). Method 1 could not be applied as available DEM does not include building geometry, only terrain elevation is provided. Method 3 was not applied as it is assumed to be more suited to flood simulation over larger areas with many urbanized zones in them. In the case of the Olbia flood, we are interested in reconstructing detailed inundation in one single urban area.

Hydrographs of the six streams flowing to Olbia reconstructed by the FEST hydrological model were used as forcing input of the hydraulic model. The domain was implemented with a square mesh with 15 m spatial resolution deriving information from an available LIDAR survey with 1 m spatial resolution.

By comparing the flood extent simulated by the hydraulic model and the one surveyed after the flood (Figures 7 and 8), a good agreement can be observed. The small discrepancy is probably due to the contribution of the subsurface urban drainage flow that is not considered in the mathematical model, and uncertainties in hydrological reconstruction of stream flood hydrographs. This confirms that the use of a simplified equation and approximation of buildings as high friction cells does not introduce significant error in practical applications when flood area must be assessed, even in a complex area such as the one considered in this analysis.

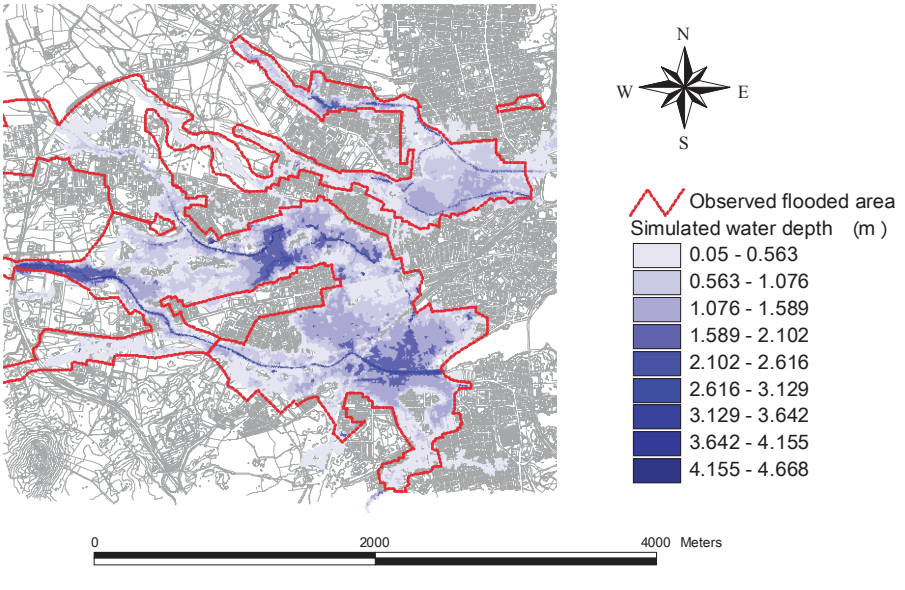


**Figure 7.** Water depth (m) simulated by the 2D hydraulic model compared to the observed flood extent.

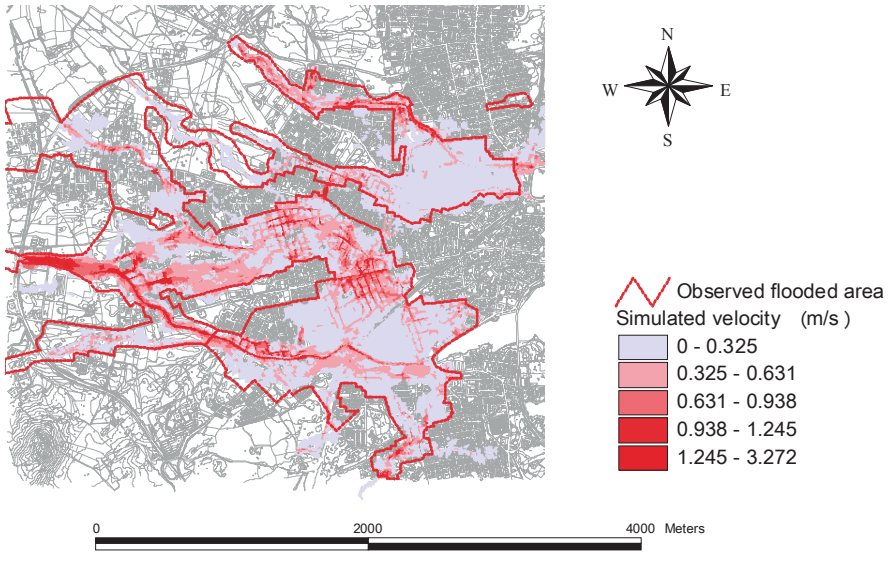


**Figure 8.** Flow velocity (m/s) simulated by the 2D hydraulic model compared to the observed flood extent.

## 4. Conclusions

In this paper, three different methods to simulate the influence of buildings on flood inundation have been tested against measurement undertaken on a simplified urban district model in laboratory. The first method considered detailed information about topography of area containing the buildings. According to the further two methods tested, single buildings or the entire urban district are represented with a high friction area.

Results show that adoption of 2D diffusive model and roughness parameter method to represent buildings is a good option to model water heights, even when unsteady discharge with rapid change in time is considered.

On the other hand, water velocities are significantly better reconstructed by methods that consider the effect of single buildings, like in Methods 1 and 2. Results of unsteady analysis show that solution of the full SWE is less sensitive to the method considered for representing buildings respect to diffusive simplification.

Application to the simulation of a real flood that occurred in Olbia (Italy) demonstrated that use of 2D diffusive model and setting high friction instead of detailed building geometry is an effective method to assess flood inundation extent.

**Acknowledgments:** We thank the three anonymous reviewers that provided comments that helped to improve this manuscript.

**Author Contributions:** Riccardo Beretta, Giovanni Ravazzani, and Marco Mancini conceived and designed the experiments; Riccardo Beretta performed the experiments; Riccardo Beretta, Giovanni Ravazzani, and Carlo Maiorano analyzed the data; Riccardo Beretta and Giovanni Ravazzani wrote the paper.

**References**


1. Berz, G.; Kron, W.; Loster, T.; Rauch, E.; Schimetschek, J.; Schmieder, J.; Siebert, A.; Smolka, A.; Wirtz, A. World map of natural hazards—A global view of the distribution and intensity of significant exposures. *Nat. Hazards* **2001**, *23*, 443–465. [CrossRef]
2. Milly, P.C.D.; Wetherald, R.T.; Dunne, K.A.; Delworth, T.L. Increasing risk of great floods in a changing climate. *Nature* **2002**, *415*, 514–517. [CrossRef] [PubMed]
3. De Almeida, G.A.M.; Bates, P.; Freer, J.; Souvignet, M. Improving the stability of a simple formulation of the shallow water equations for 2-D flood modeling. *Water Resour. Res.* **2012**, *48*, W05528. [CrossRef]
4. Peraire, J.; Zienkiewicz, O.C.; Morgan, K. Shallow water problems: A general explicit formulation. *Int. J. Numer. Methods Eng.* **1986**, *22*, 547–574. [CrossRef]
5. Toro, E.F.; Garcia-Navarro, P. Godunov-type methods for freesurface shallow flows: A review. *J. Hydraul. Res.* **2007**, *45*, 736–751. [CrossRef]
6. Guinot, V.; Frazão, S. Flux and source term discretization in two-dimensional shallow water models with porosity on unstructured grids. *Int. J. Numer. Method Fluids* **2006**, *50*, 309–345. [CrossRef]
7. LeVeque, R.J.; George, D.L. High-resolution finite volume methods for the shallow water equations with bathymetry and dry states. In *Advanced Numerical Models for Simulating Tsunami Waves and Runup*; World Scientific: Singapore, 2008. Available online: http://www.amath.washington.edu/rjl/pubs/catalina04 (accessed on 10 January 2018).
8. Sanders, B.; Schubert, J.E.; Gallegos, H.A. Integral formulation of shallow-water equations with anisotropic porosity for urban flood modeling. *J. Hydrol.* **2008**, *362*, 19–38. [CrossRef]
9. Li, S.; Duffy, C.J. Fully coupled approach to modeling shallow water flow, sediment transport, and bed evolution in rivers. *Water Resour. Res.* **2011**, *47*, W03508. [CrossRef]
10. Tsakiris, G. Flood risk assessment: Concepts, modelling, applications. *Nat. Hazard Earth Syst. Sci.* **2014**, *14*, 1361–1369. [CrossRef]
11. Alcrudo, F. Mathematical Modelling Techniques for Flood Propagation in Urban Areas. IMPACT Project Technical Report. Available online: http://www.impact-project.net/AnnexII_DetailedTechnicalReports/AnnexII_PartB_WP3/Modelling_techniques_for_urban_flooding.pdf (accessed on 10 January 2018).
12. Liu, L.; Liu, Y.; Wang, X.; Yu, D.; Liu, K.; Huang, H.; Hu, G. Developing an effective 2-D urban flood inundation model for city emergency management based on cellular automata. *Nat. Hazards Earth Syst. Sci.* **2015**, *15*, 381–391. [CrossRef]
13. Dottori, F.; Todini, E. Testing a simple 2D hydraulic model in an urban flood experiment. *Hydrol. Proces.* **2013**, *27*, 1301–1320. [CrossRef]
14. McMillan, H.K.; Brasington, J. Reduced complexity strategies for modelling urban floodplain inundation. *Geomorphology* **2007**, *90*, 226–243. [CrossRef]
15. Hunter, N.M.; Bates, P.D.; Horritt, M.S.; Wilson, M.D. Simple spatially distributed models for predicting flood inundation: A review. *Geomorphology* **2007**, *90*, 208–225. [CrossRef]
16. Prestininzi, P. Suitability of the diffusive model for dam break simulation: Application to a CADAM experiment. *J. Hydrol.* **2008**, *361*, 172–185. [CrossRef]
17. Lopes, P.; Leandro, J.; Carvalho, R.F.; Páscoa, P.; Martins, R. Numerical and experimental investigation of a gully under surcharge conditions. *Urban Water J.* **2015**, *12*, 468–476. [CrossRef]
18. Bazin, P.-H.; Nakagawa, H.; Kawaike, K.; Paquier, A.; Mignot, E. Modeling flow exchanges between a street and an underground drainage pipe during urban floods. *J. Hydraul. Eng.* **2014**, *140*, 4014051. [CrossRef]
19. Zhou, Q.; Yu, W.; Chen, A.S.; Jiang, C.; Fu, G. Experimental assessment of building blockage effects in a simplified urban district. *Procedia Eng.* **2016**, *154*, 844–852. [CrossRef]
20. Testa, G.; Zuccala, D.; Alcrudo, F.; Mulet, J.; Soares-Frazão, S. Flash flood flow experiment in a simplified urban district. *J. Hydraul. Res.* **2007**, *45*, 37–44. [CrossRef]
21. US Army Corps of Engineers—Hydrologic Engineering Center. Hydraulic Reference Manual. Available online: http://www.hec.usace.army.mil/software/hec-ras/documentation/HEC-RAS%205.0%20Reference%20Manual.pdf (accessed on 10 January 2018).
22. Kim, J.; Ivanov, V.Y.; Katopodes, N.D. Hydraulic resistance to overland flow on surfaces with partially submerged vegetation. *Water Resour. Res.* **2012**, *48*, W10540.

23. Sammarco, P.; Di Risio, M. Effects of moored boats on the gradually varied free-surface profiles of river flows. *J. Waterw. Port Coast. Ocean Eng.* **2016**, *143*, 04016020. [CrossRef]
24. Yamashita, K.; Suppasri, A.; Oishi, Y.; Imamura, F. Development of a tsunami inundation analysis model for urban areas using a porous body model. *Geosciences* **2018**, *8*, 12. [CrossRef]
25. US Army Corps of Engineers—Hydrologic Engineering Center. HEC-RAS 5.0 River Analysis System 2D Modeling User's Manual. Available online: http://www.hec.usace.army.mil/software/hec-ras/documentation/HEC-RAS%205.0%202D%20Modeling%20Users%20Manual.pdf (accessed on 10 January 2018).
26. Ravazzani, G.; Amengual, A.; Ceppi, A.; Homar, V.; Romero, R.; Lombardi, G.; Mancini, M. Potentialities of ensemble strategies for flood forecasting over the Milano urban area. *J. Hydrol.* **2016**, *539*, 237–253. [CrossRef]
27. Ravazzani, G.; Bocchiola, D.; Groppelli, B.; Soncini, A.; Rulli, M.C.; Colombo, F.; Mancini, M.; Rosso, R. Continuous stream flow simulation for index flood estimation in an Alpine basin of Northern Italy. *Hydrol. Sci. J.* **2015**, *60*, 1013–1025. [CrossRef]
28. Ravazzani, G.; Gianoli, P.; Meucci, S.; Mancini, M. Assessing downstream impacts of detention basins in urbanized river basins using a distributed hydrological model. *Water Resour. Manag.* **2014**, *28*, 1033–1044. [CrossRef]
29. Ravazzani, G.; Gianoli, P.; Meucci, S.; Mancini, M. Indirect estimation of design flood in urbanized river basins using a distributed hydrological model. *J. Hydrol. Eng.* **2014**, *19*, 235–242. [CrossRef]
30. Ehlschlaeger, C.R. Using the AT search algorithm to develop hydrologic models from digital elevation data. In Proceedings of the International Geographic Information System (IGIS) Symposium, Baltimore, MD, USA, 18–19 March 1989.
31. Soil Conservation Service. *National Engineering Handbook, Hydrology, Section 4*; US Department of Agriculture: Washington, DC, USA, 1986.
32. Miliani, F.; Ravazzani, G.; Mancini, M. Adaptation of precipitation index for the estimation of Antecedent Moisture Condition (AMC) in large mountainous basins. *J. Hydrol. Eng.* **2011**, *16*, 218–227. [CrossRef]
33. Ponce, V.M.; Chaganti, P.V. Variable—Parameter Muskingum—Cunge method revisited. *J. Hydrol.* **1994**, *162*, 433–439. [CrossRef]

# 3

# SPI Trend Analysis of New Zealand Applying the ITA Technique

**Tommaso Caloiero**

National Research Council—Institute for Agricultural and Forest Systems in Mediterranean (CNR-ISAFOM), Via Cavour 4/6, 87036 Rende, Cosenza, Italy; tommaso.caloiero@isafom.cnr.it

**Abstract:** A natural temporary imbalance of water availability, consisting of persistent lower-than-average or higher-than-average precipitation, can cause extreme dry and wet conditions that adversely impact agricultural yields, water resources, infrastructure, and human systems. In this study, dry and wet periods in New Zealand were expressed using the Standardized Precipitation Index (SPI). First, both the short term (3 and 6 months) and the long term (12 and 24 months) SPI were estimated, and then, possible trends in the SPI values were detected by means of a new graphical technique, the Innovative Trend Analysis (ITA), which allows the trend identification of the low, medium, and high values of a series. Results show that, in every area currently subject to drought, an increase in this phenomenon can be expected. Specifically, the results of this paper highlight that agricultural regions on the eastern side of the South Island, as well as the north-eastern regions of the North Island, are the most consistently vulnerable areas. In fact, in these regions, the trend analysis mainly showed a general reduction in all the values of the SPI: that is, a tendency toward heavier droughts and weaker wet periods.

**Keywords:** drought; SPI; trend; New Zealand

## 1. Introduction

Recently, the adverse impacts of climate change have become the focus of considerable international attention due to the increase in phenomena such as flood, heat waves, forest fires, and droughts [1,2]. Among these damaging climate events, drought phenomena play a significant role in socio-economic and health terms, even though their impact on populations depends on the vulnerable elements [3]. Moreover, understanding drought phenomena is paramount for the appropriate planning and management of water resources [4]. For example, different drought events have been detected during the last decades [5–7], and drought is expected to become more frequent in the 21st century in some seasons and areas [8] following precipitation and/or evapotranspiration variability [9].

In recent years, several researchers have analyzed drought events in several parts of the world [10–17], even though drought phenomena are difficult to detect and to monitor due to their complex nature. Usually, drought severity is evaluated by means of drought indices since they facilitate communication of climate anomalies to diverse user audiences; they also allow scientists to assess quantitatively climate anomalies in terms of their intensity, duration, frequency, recurrence probability, and spatial extent [3,18]. In the past few decades, numerous indices were proposed for identifying and monitoring drought events. Some of these indices refer to meteorological drought (scarcity of precipitation) and are based on the analysis of the rainfall information only. Thus, different categories of drought can be investigated by choosing appropriate temporal scales addressing different categories of users. Other indices, however, are more suitable to describe hydrological drought (scarcity in surface and subsurface water supplies), agricultural drought (water shortage compared to the typical needs crops irrigation), and socio-economic drought (referred to the global water consumption).

Specifically, meteorological drought consists of temporary lower-than-average precipitation and results in diminished water resources availability [19], which impact on economic activities, human lives, and the environment [20]. The most well-known index for analyzing the meteorological drought is undoubtedly the Standardized Precipitation Index (SPI) proposed by McKee et al. [21], which has been extensively applied in different countries [22–28]. This drought index can be considered one of the most robust and effective drought indices, as it can be evaluated for different time scales and allows the analysis of different drought categories [29]. Moreover, the evaluation of the SPI requires only precipitation data, making it easier to calculate more than complex indices, and allows for the comparison of drought conditions in different regions and for different time periods [30–33]. Due to its intrinsic probabilistic nature, the SPI is the ideal candidate for carrying out drought risk analysis [34,35]. With this aim, several authors focused on the SPI trend [36–38]. These studies are mainly based on non-parametric tests, which are better suited to deal with non-normally distributed hydrometeorology data than the parametric methods. Recently, Şen [39] proposed the Innovative Trend Analysis (ITA) technique, which allows a graphical trend evaluation of the low, medium, and high values in the data. The ITA technique was widely applied to the trend detection of several hydrological variables. Haktanir and Citakoglu [40] analyzed the annual maximum rainfall series by means of the ITA method. Kisi and Ay [41] studied some water quality parameters registered at five Turkish stations by means of the ITA and the MK. Şen [42] and Ay and Kisi [43] applied the ITA to Turkish temperature data. The ITA technique was also used to analyze the trends of heat waves [44], monthly pan evaporations [45], and streamflow data [46].

Since agriculture is one of the largest sectors of the tradable economy, a period of drought in New Zealand can have significant ecological, social, and economic impacts [47]. In fact, New Zealand experiences rainfall deficits and short duration of dry spells that are not as unusual as isolated drought events at regional level. For example, the widespread drought event that affected New Zealand from late 2007 to the end of autumn 2008 caused damages of about 2.8 billion New Zealand dollars [48]. The 2013 drought in New Zealand was estimated to have caused GDP (Gross Domestic Product) to fall by 0.6% [49]. Regional scenarios of drought in New Zealand evidenced an increase in drought trends during this century in all the areas presently subject to drought [50]. Furthermore, based on the latest climate and impact modelling, more droughts can be expected in the future in some locations such as the agricultural regions on the Eastern coast and particularly the Canterbury Plains, as well as Northland [51].

In this article, drought events in several regions of New Zealand have been studied by applying the SPI at various time scales (3, 6, 12, and 24 months) starting from a database of 294 monthly rainfall series in the period 1951–2010. In particular, this work aims to identify the most drought-prone regions of New Zealand by analyzing its evolution through the identification of the SPI trend at different timescales by means of the Innovative Trend Analysis (ITA), which allows the trend identification of the low, medium, and high values of a series.

## 2. Methodology

### *2.1. Standardized Precipitation Index*

In this study, dry and wet periods were evaluated using the SPI at different time scale (3, 6, 12 and 24 months). In fact, while the 3- and 6-month SPI describe droughts that affect plant life and farming, the 12- and 24-month SPI influence the way how water supplies/reserves are managed [52,53]. Angelidis et al. [54] offered a meticulous description of the method to compute the SPI.

In order to calculate the index, for each time scale, an appropriate probability density function (PDF) must be fitted to the frequency distribution of the cumulated precipitation. In particular, a gamma function is considered. The shape and the scale parameters must be estimated for each month of the year and for each time aggregation, for example by using the approximation of Thom [55].

Since the gamma distribution is undefined for a rainfall amount $x = 0$, in order to take into account the zero values that occur in a sample set, a modified cumulative distribution function (CDF) must be considered.

$$H(x) = q + (1 - q)G(x) \tag{1}$$

with $G(x)$ the CDF and $q$ the probability of zero precipitation, given by the ratio between the number of zero in the rainfall series ($m$) and the number of observations ($n$).

Finally, the CDF is changed into the standard normal distribution by using, for example, the approximate conversion provided by Abramowitz and Stegun [56].

$$z = \mathrm{SPI} = -\left(t - \frac{c_0 + c_1 t + c_2 t^2}{1 + d_1 t + d_2 t^2 + d_3 t^3}\right), t = \sqrt{\ln\left(\frac{1}{(H(x))^2}\right)} \text{ for } 0 < H(x) < 0.5, \tag{2}$$

$$z = \mathrm{SPI} = +\left(t - \frac{c_0 + c_1 t + c_2 t^2}{1 + d_1 t + d_2 t^2 + d_3 t^3}\right), t = \sqrt{\ln\left(\frac{1}{(1 - H(x))^2}\right)} \text{ for } 0.5 < H(x) < 1, \tag{3}$$

with $c_0$, $c_1$, $c_2$, $d_1$, $d_2$, and $d_3$ as mathematical constants.

Table 1 reports the climatic classification according to the SPI provided by the National Drought Mitigation Center. This index is now habitually used in the classification of wet periods, even though the original classification provided by McKee et al. [21] was limited to drought periods only.

**Table 1.** Climate classification according to the Standardized Precipitation Index (SPI) values.

| SPI Value | Class | Probability (%) |
|---|---|---|
| SPI $\geq$ 2.00 | Extremely wet | 2.3 |
| 1.5 $\leq$ SPI < 2.00 | Severely wet | 4.4 |
| SPI < 1.50 | Moderately wet | 9.2 |
| SPI < 1.00 | Mildly wet | 34.1 |
| $-1.00 \leq$ SPI < 0.00 | Mild drought | 34.1 |
| $-1.50 \leq$ SPI < $-1.00$ | Moderate drought | 9.2 |
| $-2.00 \leq$ SPI < $-1.50$ | Severe drought | 4.4 |
| SPI < $-2.00$ | Extreme drought | 2.3 |

*2.2. Innovative Trend Analysis (ITA)*

The ITA method has been first proposed by Şen [39]: unlike the MK test or other methods, the ITA's greatest advantage is the fact that it does not require any assumptions (serial correlation, non-normality, sample number, and so on). First, the time series is divided into two equal parts, which are separately sorted in ascending order. Then, the first and the second half of the time series are located on the X-axis and on the Y-axis, respectively. In Figure 1, a graphical representation of the innovative method on a Cartesian coordinate system is shown. If the data are collected on the 1:1 ideal line (45° line), there is no trend in the time series. If data are located on the upper triangular area of the ideal line, an increasing trend in the time series exists, while if data are accumulated in the lower triangular area of the 1:1 line, there is a decreasing trend in the time series [39,42]. Thus, trends of low, medium, and high values of any hydro-meteorological or hydro-climatic time series can be clearly identified through this method.

For example, the results shown in Figure 1 identify a positive trend of the lowest values and a negative trend of the highest ones, while no trends can be detect for the medium values that lies near the 1:1 ideal line.

In this work, in order to easily and better identify the possible trend of the severe dry and wet conditions, two vertical bands have been added in Figure 1: a red band corresponding to the severe drought limit (SPI = $-1.5$) and a blue band corresponding to the severe wet limit (SPI = 1.5).

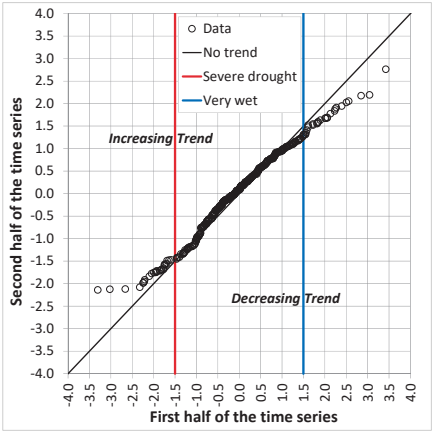


**Figure 1.** Example of the Innovative Trend Analysis (ITA) proposed by Şen [39].

## 3. Study Area

New Zealand, with an elongated shape of 1930 km and a maximum width of 400 km and a surface area of about 270,000 km$^2$, is located in the southern hemisphere 2500 km east from Australia. Its altitude distribution is mainly mountainous; in fact, 76% of its territory presents an elevation higher than 600 m a.s.l. with a maximum altitude of 3724 m (Figure 2).

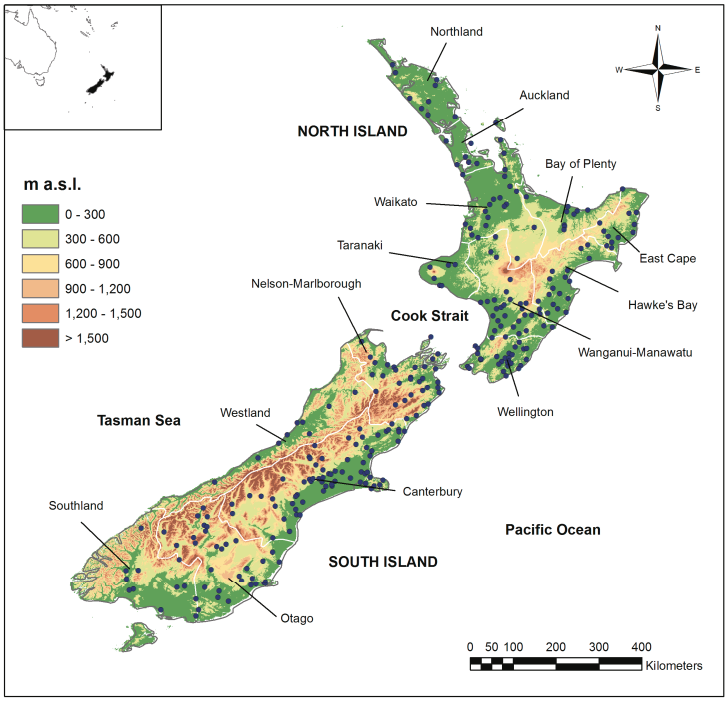


**Figure 2.** Location of the 14 regions of New Zealand and of the selected 294 rain gauge stations on a Digital Elevation Model (DEM) of New Zealand.

New Zealand's climate is mainly influenced by the following physical factors [57]:

a. The water masses surrounding the country, which results in cool summers and moderately cold winters, and the cold air masses from Antarctica, which cause snow and frost in some areas of the country;
b. The mountains crossing both the islands, which constitute a barrier against air flows coming in from south-south west, cause significant differences in the rainfall amounts, also within short distances;
c. The proximity of the Australia's eastern land/sea boundary, which is characterized by a low-pressure region of cyclonic circulation toward the Tasman Sea.

For a more thorough description of the New Zealand's climate, interested readers can refer to the National Institute of Water and Atmosphere Research (NIWA) of New Zealand, which published a detailed analysis of New Zealand's climate [58].

In order to carry out an SPI analysis at different time scales, the New Zealand National Climate database of the National Institute of Water and Atmospheric Research (NIWA) has been selected. Several studies on New Zealand's climate [59–65] made extensive use of this database, which presents high-quality data and complete, or near complete, records for the period 1951–2010. Until 2010, the New Zealand National Climate database consisted of measurements collected at 3011 stations, with a density of one station per 89 $km^2$. In particular, for the present analysis, the monthly rainfall data were extracted and used after performing record error checks and metadata analyses for inhomogeneities detection. Following these procedures, a number of station series, which presented either low quality records or few years of observation for statistical purposes (<50 available years of data), were discarded. The series ending before 2010 and those showing more than 5% of lacking data were also discarded. Thus, the final selection included 294 series longer than 50 years with a density of one station per 913 $km^2$ (Figure 2).

**4. Results and Discussion**

Following the NIWA, which provides climate maps at regional scale, for every region of New Zealand shown in Figure 2, an average SPI series has been evaluated for each time scale, and a trend analysis has been performed through the application of the ITA approach. In particular, the SPI has been evaluated for each rain gauge and for each time scale and then a simple arithmetic average of the obtained SPI values has been computed for each region.

Before applying the ITA, the number of months showing severe or extreme dry and wet conditions was evaluated. As a result, different conditions have been detected considering the different time scales.

As to what concerns the 3-month SPI (Figure 3a) in nine out of 14 regions the number of months showing severe or extreme wet conditions is higher than the ones showing severe or extreme dry conditions. In particular, in the South Island, in the Canterbury and Southland areas, only in 15 and 18 months dry conditions have been detected while, instead, 32 and 27 months evidenced wet conditions, respectively. Differently from these regions, in the Hawke's Bay area (North Island), the months that showed dry conditions (35 months) clearly outperform the months (24) in which wet conditions have been detected.

The 6-month SPI (Figure 3b) showed a different behavior with respect to the 3-month SPI. In fact, in eight regions, the number of months showing severe or extreme dry conditions is higher than the one presenting wet conditions. Dry conditions have been detected especially in the North Island and, specifically, in the Auckland (27 months against 16), Bay of Plenty (36 months against 29), East Cape (37 months against 31), Wanganui-Manawatu (28 months against 13), and Hawke's Bay (31 months against 19) areas. In the South Island, only the Nelson-Marlborough region showed dry conditions in 26 months (17 wet months), while in the other regions, wet conditions have been evidenced.

Concerning the 12-month SPI (Figure 3c) an equal number of regions showed prevailing dry or wet conditions. In particular, in the North Island, in six out of nine regions, the number of months showing dry conditions is higher than the ones showing wet conditions. Conversely, in the South Island, four regions showed wet conditions, and only one region (Nelson-Marlborough) evidenced dry conditions. Specifically, in the North Island, relevant results have been obtained in the Bay of Plenty and in the East Cape regions, with 38 and 40 months showing severe or extreme dry conditions, respectively, while, in the South Island, the Westland (45 months against 24) and the Southland (38 months against 22) regions marked dry conditions have been detected.

Finally, the 24-month SPI (Figure 3d) showed a clear difference between the two islands. In fact, in the North Island, severe or extreme dry conditions have been detected in all the regions, while severe or extreme wet conditions have been detected in all the regions of the South Island. In particular, the driest conditions in the North Island have been detected in the Taranaki (73 months against 34) and in the Bay of Plenty (61 months against 37) regions, while, in the South Island, the Southland (73 months against 34) and the Canterbury (61 months against 37) areas showed the highest number of months with wet conditions.

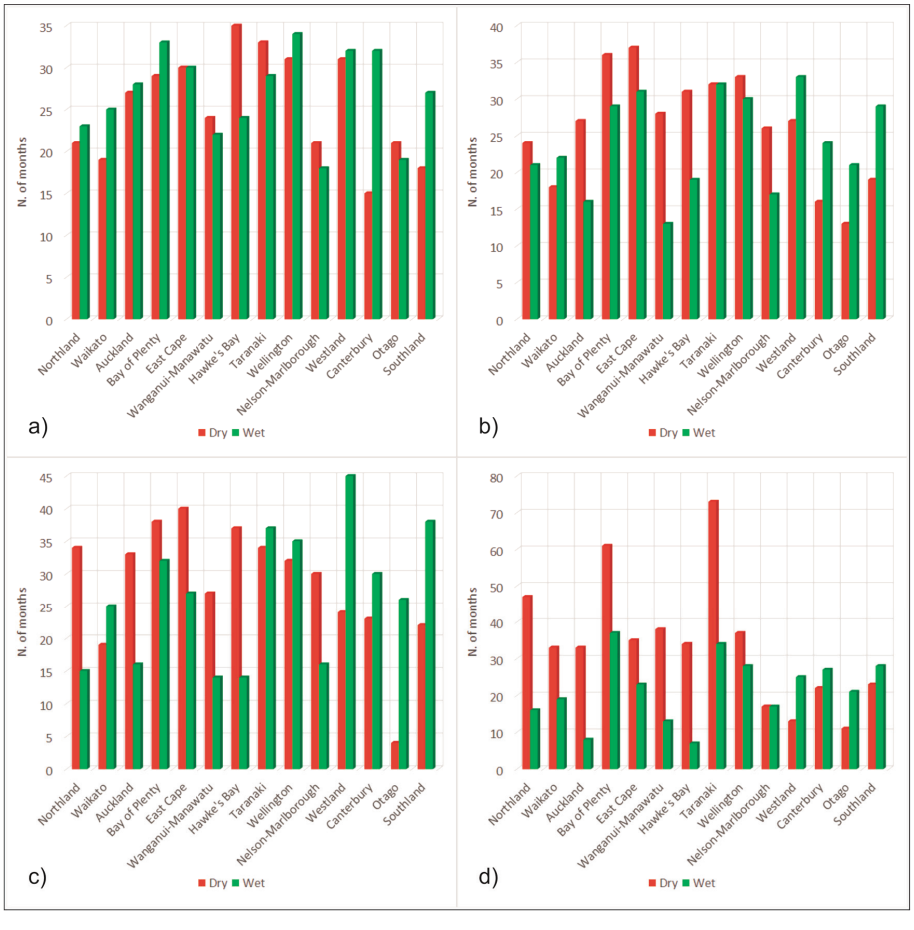


**Figure 3.** Number of months showing severe or extreme dry and wet conditions for the 3-month (**a**); 6-month (**b**); 12-month (**c**); and 24-month SPI (**d**).

With the aim to detect possible trends in the 3-, 6-, 12-, and 24-month SPI values, for each region the ITA method was applied to the monthly series of the index. The ITA method allowed to evidence the tendencies of both low and high SPI values, thus including values referred to wet conditions. As a result of the ITA approach, Figures 4–7 show the results obtained at regional level for the 3-, 6-, 12- and 24-month SPI, respectively. All the SPI series were divided into two 30-year sub-series: from 1951 to 1980, and from 1981 to 2010.

Generally, the main result obtained for the 3-month SPI values was a negative trend of the highest values of the index, which is related to weaker wet periods (Figure 4). This tendency has been detected in nine out of 14 regions but with a different behavior of the lowest SPI values. In fact, in four regions of the North Island (Northland, Auckland, Bay of Planty and East Cape) and in the Canterbury region in the South Island, a negative trend of both the lowest and the highest values of the index has been detected, thus evidencing heavier droughts and weaker wet periods. At the same time, in the Waikato, Wellington, Southland, and Westland regions, a positive trend of the lowest values and negative trend of the highest ones has been evidenced, both indicating weaker droughts and wet periods. Differently from the previous regions, the Otago, Wanganui-Manawatu, and Taranaki areas evidenced a tendency through weaker droughts and heavier wet periods given by a positive trend of both the lowest and the highest SPI values. Finally, in the Nelson-Marlborough region, a negative trend of the lowest values (heavier droughts) and a positive trend of the highest values (heavier wet periods) have been detected. The results of the ITA methods on the Hawke's Bay region did not show a clear tendency, with the lowest and highest values falling close to the no trend line.

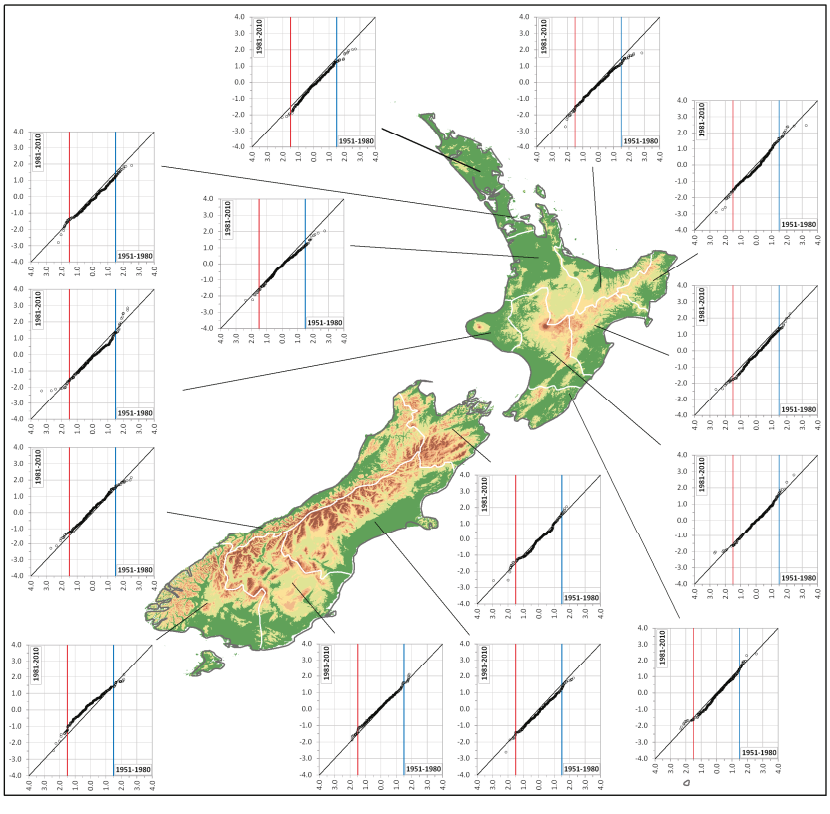


**Figure 4.** Regional results of the Innovative Trend Analysis (ITA) method applied to the 3-month SPI.

As regards the 6-month SPI, results confirm the ones obtained for the 3-month SPI, with a spreading negative trend of the highest values of the index (Figure 5). In fact, similar results to the 3-month SPI have been obtained in Northland, Auckland, Bay of Planty, Wanganui-Manawatu, Taranaki, Nelson-Marlborough, Westland, and Southland. Different from the results obtained for the 3-month SPI, in the Waikato and in the Hawke's Bay regions, a negative trend of both the lowest and the highest values of the SPI index has been detected. Moreover, in the Canterbury and Otago region, a positive trend of the lowest values (weaker droughts) and a negative trend of the highest values (weaker wet periods) have been evidenced. Finally, the Wellington and East Cape regions did not show a clear tendency.

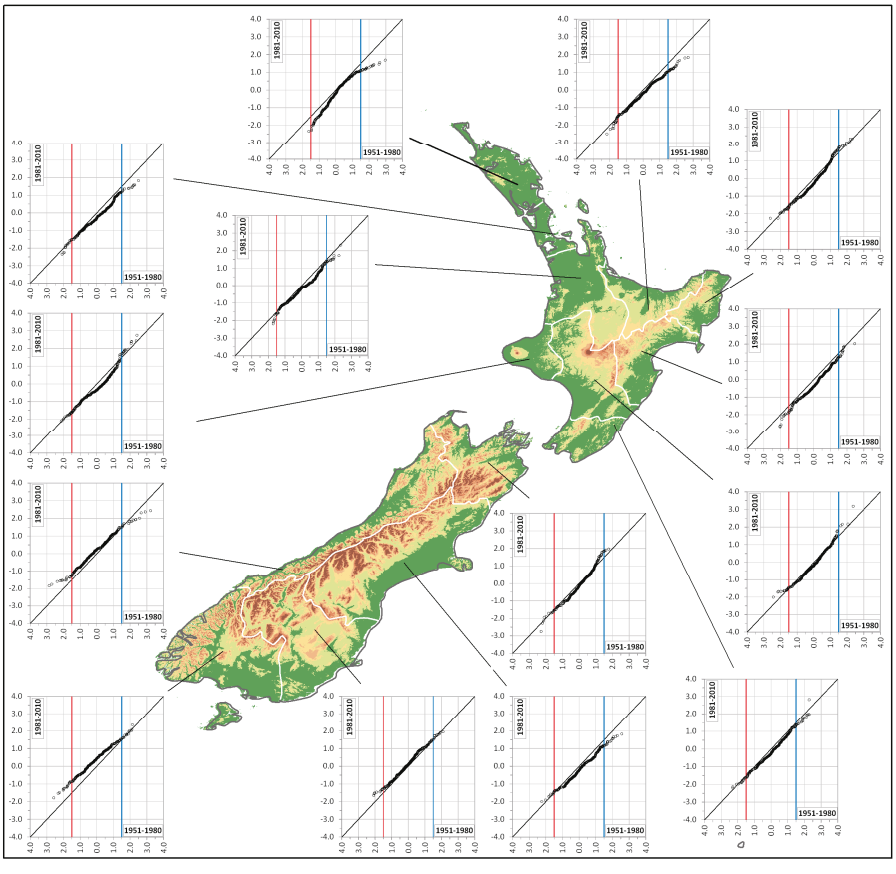


**Figure 5.** Regional results of the ITA method applied to the 6-month SPI.

Studies on the 3- and 6-month SPI trends, which impact vegetation and agricultural practices, are paramount for New Zealand because agriculture is one of the largest sectors of the economy. As a summary of the results of the trend analysis on these time scales, in the South Island, which is generally characterized by wet conditions, a negative trend of the highest SPI value has been detected in the majority of the regions, thus indicating a tendency toward weaker wet periods. In particular, in the agricultural area of the Canterbury, the 3-month SPI evidenced a decreasing trend of both the lowest and the highest values of the index, which lead to heavier droughts and weaker wet periods. In the North Island, where the majority of the regions showed a higher percentage of dry months than wet

months, a general negative trend of both the lowest and the highest SPI values has been identified, with the exception of some region such as Wanganui-Manawatu and Taranaki.

Considering the long time scales, the 12-month SPI trend showed similar results than the 6-month SPI but with an increase in the negative trend (Figure 6). In fact, in the Northland, Waikato, Auckland, Bay of Planty, East Cape, Hawke's Bay, and Canterbury regions, a reduction of all the SPI values has been detected, thus confirming a clear tendency toward heavier droughts and weaker wet periods. On the contrary, the Wanganui-Manawatu, Nelson-Marlborough, and Otago regions showed trend results that indicate weaker droughts and heavier wet periods. An increase of the lowest values and a decrease in the highest values (weaker wet and dry periods) has been evidenced in the Wellington, Westland, and Southland regions. In the Taranaki area, no clear tendencies have been detected in the severe and extreme SPI values.

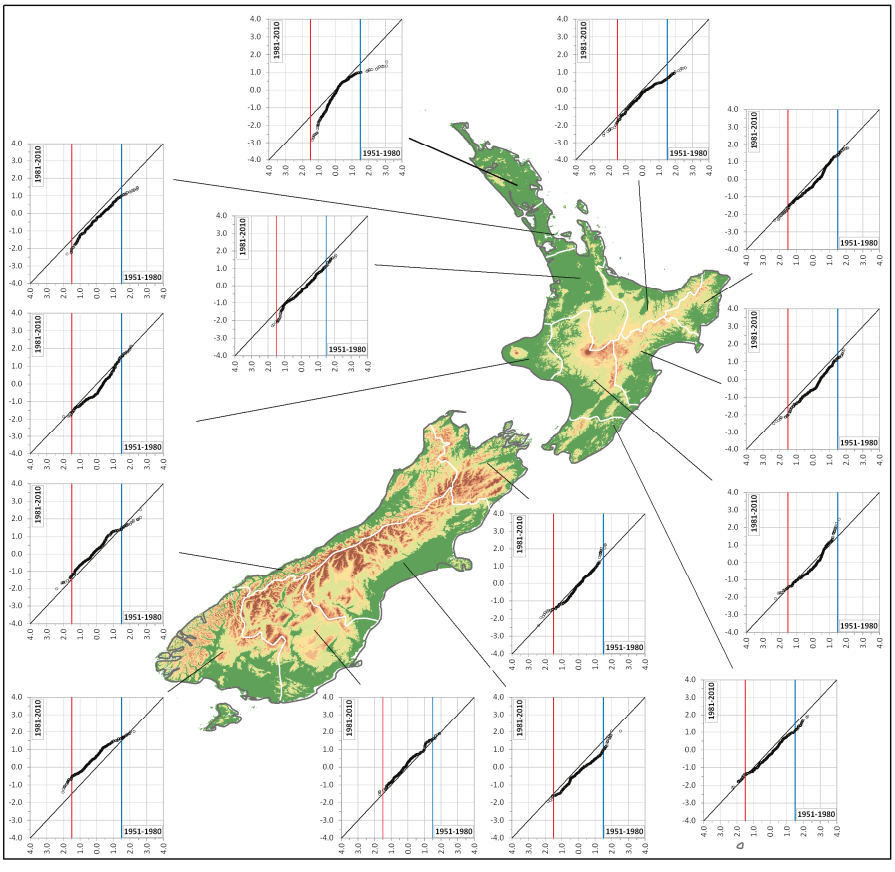


**Figure 6.** Regional results of the ITA method applied to the 12-month SPI.

As regards the 24-month SPI, in eight regions (Northland, Waikato, Auckland, Bay of Planty, East Cape, Wanganui-Manawatu, Hawke's Bay, and Canterbury), the results of the trend analysis with the ITA method evidenced a clear reduction of the lowest SPI values. Among these regions, the same result has been obtained for the highest values, with the exception of the Waikato and Auckland, in which the highest values showed a positive trend. By contrast, the Taranaki, Nelson-Marlborough, Otago Westland, and Southland regions showed an increase in the lowest values, with concomitant

decrease in the highest values in the Taranaki and Otago areas and increase in the highest values in the Nelson-Marlborough, Westland, and Southland regions. As also evidenced for the 3-month SPI, the Wellington region did not show a clear tendency.

The 12- and 24-month SPI are a broad proxy for water resource management. Results of the trend analysis on these time scales confirm the ones obtained on a short time scale but with an increase in the number of regions where a negative trend has been detected. In fact, current global level assessments suggest that droughts are expected to both increase and decrease following future climate change depending upon geographic location [66]. Based on the latest climate and impact modelling, New Zealand can expect more droughts in the future in some locations [51].

As a result, this work has evidenced an increase in drought trend in all the areas that are presently subject to drought, supporting what has been evidenced in past studies [50,64]. In fact, the results of this paper confirm the geographic pattern of change found by Mullan et al. [50] and Caloiero [64], which mainly detected a drought increase in the future projections on the East Coast and no change in drought projections for the West Coast of the South Island. Specifically, as also evidenced by Clark et al. [51] and Caloiero [64], the results of this paper highlight that key agricultural regions on the Eastern side such as the Canterbury Plains are the most consistently vulnerable areas in the South Island, together with other regions in the North Island, including a key primary industry region like Waikato.

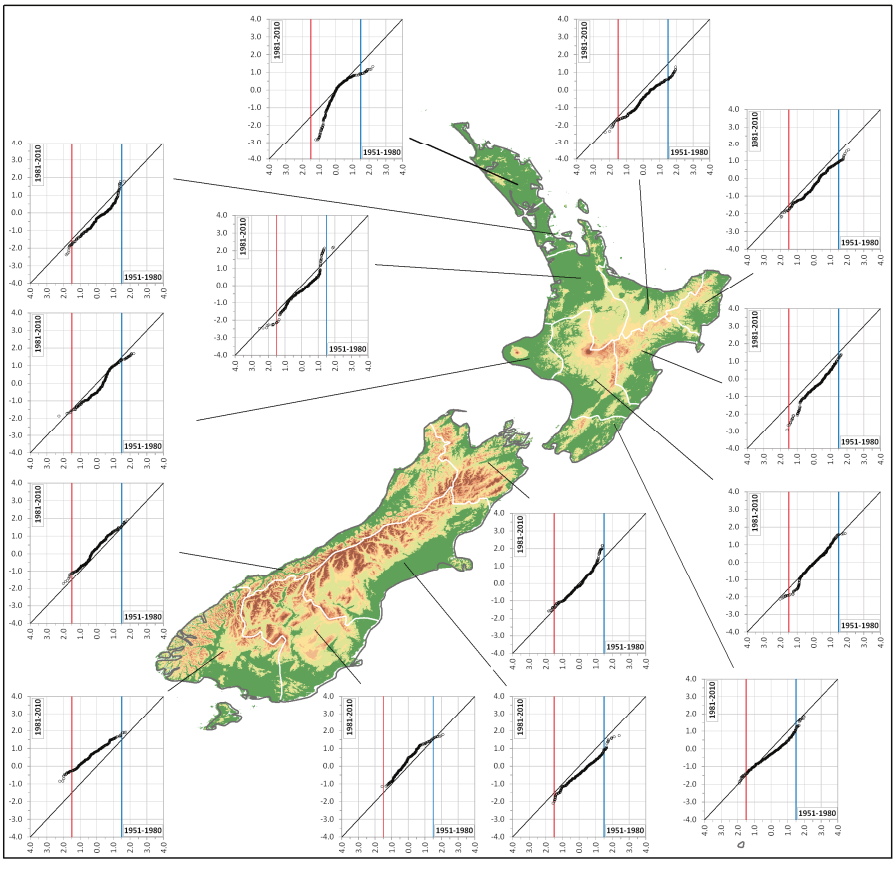


**Figure 7.** Regional results of the ITA method applied to the 24-month SPI.

## 5. Conclusions

Generally, the methods used for trend detection allow researchers to analyze general tendencies of climatic variables, but they do not make it possible to identify sub-trends. In this paper, for every region of New Zealand, an average SPI series has first been evaluated at various time scales (3, 6, 12, and 24 months). Then, for each region, the number of months showing severe or extreme dry and wet conditions has been detected. Finally, a graphical technique, based on the Innovative Trend Analysis (ITA) proposed by Şen [39], was applied to the SPI series. As a result, a different behavior emerged between the two islands. In fact, for the several time scale, in the majority of the regions of the North Island, the number of months showing dry conditions is higher than the ones showing wet conditions, while in the South Island, the number of months showing wet conditions is higher than the ones showing dry conditions. In particular, for the 24-month time scale, dry conditions have been detected in all the regions of the North Island, while wet conditions have been detected in the South Island ones. As to what concerns the trend analysis, on a short time scale, the results showed a negative trend of the highest SPI value in the South Island, thus indicating a tendency toward weaker wet periods. In particular, in the agricultural area of the Canterbury, the 3-month SPI evidenced a decreasing trend in both the lowest and the highest values of the index, which lead to heavier droughts and weaker wet periods. In the North Island, a general negative trend of both the lowest and the highest SPI values has been identified, thus evidencing heavier droughts and weaker wet periods. Results of the trend analysis on long time scales confirm the ones obtained on a short time scale but with an increase in the number of regions where a negative trend has been detected, highlighting that agricultural regions on the eastern side of the South Island, as well as the north-eastern regions of the North Island, are the most consistently vulnerable areas.

**Acknowledgments:** The author would like to thank the National Institute of Water and Atmosphere Research for providing access to the New Zealand meteorological data from the National Climate Database.

## References

1. Estrela, T.; Vargas, E. Drought management plans in the European Union. *Water Resour. Manag.* **2010**, *26*, 1537–1553. [CrossRef]
2. Kreibich, H.; Di Baldassarre, G.; Vorogushyn, S.; Aerts, J.C.J.H.; Apel, H.; Aronica, G.T.; Arnbjerg-Nielsen, K.; Bouwer, L.M.; Bubeck, P.; Caloiero, T.; et al. Adaptation to flood risk: Results of international paired flood event studies. *Earth's Future* **2017**, *5*, 953–965. [CrossRef]
3. Wilhite, D.A.; Hayes, M.J.; Svodoba, M.D. Drought monitoring and assessment in the US. In *Drought and Drought Mitigation in Europe*; Voght, J.V., Somma, F., Eds.; Kluwers: Dordrecht, The Netherlands, 2000; pp. 149–160.
4. Yevjevich, V.; Da Cunha, L.; Vlachos, E. *Coping with Droughts*; Water Resources Publications: Littleton, CO, USA, 1983.
5. Fink, A.H.; Brücher, T.; Krüger, A.; Leckebush, G.C.; Pinto, J.G.; Ulbrich, U. The 2003 European summer heatwaves and drought-synoptic diagnosis and impacts. *Weather* **2004**, *59*, 209–216. [CrossRef]
6. Lloyd-Huhes, B.; Saunders, M.A. A drought climatology for Europe. *Int. J. Climatol.* **2002**, *22*, 1571–1592. [CrossRef]
7. Zaidman, M.D.; Rees, H.G.; Young, A.R. Spatio-temporal development of streamflow droughts in north-west Europe. *Hydrol. Earth Syst. Sci.* **2012**, *5*, 733–751. [CrossRef]
8. Hannaford, J.; Lloyd-Hughes, B.; Keef, C.; Parry, S.; Prudhomme, C. Examining the large-scale spatial coherence of European drought using regional indicators of precipitation and streamflow deficit. *Hydrol. Process.* **2011**, *25*, 1146–1162. [CrossRef]
9. Intergovernmental Panel on Climate Change (IPCC). *Summary for Policymakers*; Fifth Assessment Report of the Intergovernmental Panel on Climate Change; Cambridge University Press: Cambridge, UK, 2013.
10. Buttafuoco, G.; Caloiero, T.; Ricca, N.; Guagliardi, I. Assessment of drought and its uncertainty in a southern Italy area (Calabria region). *Measurement* **2018**, *113*, 205–210. [CrossRef]

11. Caloiero, T.; Coscarelli, R.; Ferrari, E.; Sirangelo, B. Analysis of Dry Spells in Southern Italy (Calabria). *Water* **2015**, *7*, 3009–3023. [CrossRef]
12. Fang, K.; Gou, X.; Chen, F.; Davi, N.; Liu, C. Spatiotemporal drought variability for central and eastern Asia over the past seven centuries derived from tree-ring based reconstructions. *Quat. Int.* **2013**, *283*, 107–116. [CrossRef]
13. Feng, S.; Hu, Q.; Oglesby, R.J. Influence of Atlantic sea surface temperatures on persistent drought in North America. *Clim. Dyn.* **2011**, *37*, 569–586. [CrossRef]
14. Hua, T.; Wang, X.M.; Zhang, C.X.; Lang, L.L. Temporal and spatial variations in the Palmer Drought Severity Index over the past four centuries in arid, semiarid, and semihumid East Asia. *Chin. Sci. Bull.* **2013**, *58*, 4143–4152. [CrossRef]
15. Minetti, J.L.; Vargas, W.M.; Poblete, A.G.; de la Zerda, L.R.; Acuña, L.R. Regional droughts in southern South America. *Theor. Appl. Climatol.* **2010**, *102*, 403–415. [CrossRef]
16. Sirangelo, B.; Caloiero, T.; Coscarelli, R.; Ferrari, E. A stochastic model for the analysis of the temporal change of dry spells. *Stoch. Environ. Res. Risk Assess.* **2015**, *29*, 143–155. [CrossRef]
17. Sirangelo, B.; Caloiero, T.; Coscarelli, R.; Ferrari, E. Stochastic analysis of long dry spells in Calabria (Southern Italy). *Theor. Appl. Climatol.* **2017**, *127*, 711–724. [CrossRef]
18. Tsakiris, G.; Pangalou, D.; Vangelis, H. Regional drought assessment based on the Reconnaissance Drought Index (RDI). *Water Resour. Manag.* **2007**, *21*, 821–833. [CrossRef]
19. Tabari, H.; Abghari, H.; Hosseinzadeh Talaee, P. Temporal trends and spatial characteristics of drought and rainfall in arid and semi-arid regions of Iran. *Hydrol. Process.* **2012**, *26*, 3351–3361. [CrossRef]
20. Bayissa, Y.A.; Moges, S.A.; Xuan, Y.; Van Andel, S.J.; Maskey, S.; Solomatine, D.P.; Griensven, A.; Van Tadesse, T. Spatio-temporal assessment of meteorological drought under the influence of varying record length: The case of Upper Blue Nile Basin, Ethiopia. *Hydrol. Sci. J.* **2015**, *60*, 1927–1942. [CrossRef]
21. McKee, T.B.; Doesken, N.J.; Kleist, J. The relationship of drought frequency and duration to time scales. In Proceedings of the 8th Conference on Applied Climatology, Anaheim, CA, USA, 17–22 January 1993; pp. 179–184.
22. Khan, S.; Gabriel, H.F.; Rana, T. Standard precipitation index to track drought and assess impact of rainfall on watertables in irrigation areas. *Irrig. Drain. Syst.* **2008**, *22*, 159–177. [CrossRef]
23. Logan, K.E.; Brunsell, N.A.; Jones, A.R.; Feddema, J.J. Assessing spatiotemporal variability of drought in the US central plains. *J. Arid Environ.* **2010**, *74*, 247–255. [CrossRef]
24. Manatsa, D.; Mukwada, G.; Siziba, E.; Chinyanganya, T. Analysis of multidimensional aspects of agricultural droughts in Zimbabwe using the Standardized Precipitation Index (SPI). *Theor. Appl. Climatol.* **2010**, *102*, 287–305. [CrossRef]
25. Patel, N.R.; Yadav, K. Monitoring spatio-temporal pattern of drought stress using integrated drought index over Bundelkhand region, India. *Nat. Hazards* **2015**, *77*, 663–677. [CrossRef]
26. Raziei, T.; Saghafian, B.; Paulo, A.A.; Pereira, L.S.; Bordi, I. Spatial patterns and temporal variability of drought in Western Iran. *Water Resour. Manag.* **2009**, *23*, 439–455. [CrossRef]
27. Buttafuoco, G.; Caloiero, T. Drought events at different timescales in southern Italy (Calabria). *J. Maps* **2014**, *10*, 529–537. [CrossRef]
28. Zhai, L.; Feng, Q. Spatial and temporal pattern of precipitation and drought in Gansu Province Northwest China. *Nat. Hazards* **2009**, *49*, 1–24. [CrossRef]
29. Capra, A.; Scicolone, B. Spatiotemporal variability of drought on a short–medium time scale in the Calabria Region (Southern Italy). *Theor. Appl. Climatol.* **2012**, *3*, 471–488. [CrossRef]
30. Wu, H.; Hayes, M.J.; Wilhite, D.A.; Svoboda, M.D. The effect of the length of record on the standardized precipitation index calculation. *Int. J. Climatol.* **2005**, *25*, 505–520. [CrossRef]
31. Vicente-Serrano, S.M. Differences in spatial patterns of drought on different time sales: An analysis of the Iberian Peninsula. *Water Resour. Manag.* **2006**, *20*, 37–60. [CrossRef]
32. Buttafuoco, G.; Caloiero, T.; Coscarelli, R. Analyses of Drought Events in Calabria (Southern Italy) Using Standardized Precipitation Index. *Water Resour. Manag.* **2015**, *29*, 557–573. [CrossRef]
33. Caloiero, T.; Coscarelli, R.; Ferrari, E.; Sirangelo, B. An Analysis of the Occurrence Probabilities of Wet and Dry Periods through a Stochastic Monthly Rainfall Model. *Water* **2016**, *8*, 39. [CrossRef]
34. Guttman, N.B. Accepting the standardized precipitation index: A calculating algorithm. *J. Am. Water Resour. Assoc.* **1999**, *35*, 311–323. [CrossRef]

35. Cancelliere, A.; Di Mauro, G.; Bonaccorso, B.; Rossi, G. Drought forecasting using the Standardised Precipitation Index. *Water Resour. Manag.* **2007**, *21*, 801–819. [CrossRef]
36. Bordi, I.; Fraedrich, K.; Sutera, A. Observed drought and wetness trends in Europe: An update. *Hydrol. Earth Syst. Sci.* **2009**, *13*, 1519–1530. [CrossRef]
37. Golian, S.; Mazdiyasni, O.; AghaKouchak, A. Trends in meteorological and agricultural droughts in Iran. *Theor. Appl. Climatol.* **2015**, *119*, 679–688. [CrossRef]
38. Zhai, J.; Su, B.; Krysanova, V.; Vetter, T.; Gao, C.; Jiang, T. Spatial variation and trends in PDSI and SPI indices and their relation to streamflow in 10 large regions of China. *J. Clim.* **2010**, *23*, 649–663. [CrossRef]
39. Şen, Z. An innovative trend analysis methodology. *J. Hydrol. Eng.* **2012**, *17*, 1042–1046. [CrossRef]
40. Haktanir, T.; Citakoglu, H. Trend, independence, stationarity, and homogeneity tests on maximum rainfall series of standard durations recorded in Turkey. *J. Hydrol. Eng.* **2014**, *19*, 501–509. [CrossRef]
41. Kisi, O.; Ay, M. Comparison of Mann–Kendall and innovative trend method for water quality parameters of the Kizilirmak River, Turkey. *J. Hydrol.* **2014**, *513*, 362–375. [CrossRef]
42. Şen, Z. Trend identification simulation and application. *J. Hydrol. Eng.* **2014**, *19*, 635–642. [CrossRef]
43. Ay, M.; Kisi, O. Investigation of trend analysis of monthly total precipitation by an innovative method. *Theor. Appl. Climatol.* **2015**, *120*, 617–629. [CrossRef]
44. Martínez-Austria, P.F.; Bandala, E.R.; Patiño-Gómez, C. Temperature and heat wave trends in northwest Mexico. *Phys. Chem. Earth* **2015**, *91*, 20–26. [CrossRef]
45. Kisi, O. An innovative method for trend analysis of monthly pan evaporations. *J. Hydrol.* **2015**, *527*, 1123–1129. [CrossRef]
46. Tabari, H.; Willems, P. Investigation of streamflow variation using an innovative trend analysis approach in northwest Iran. In Proceedings of the 36th IAHR World Congress, The Hague, The Nederland, 28 June–3 July 2015.
47. Palmer, J.G.; Cook, E.R.; Turney, C.S.M.; Allen, K.; Fenwick, P.; Cook, B.; O'Donnell, A.J.; Lough, J.M.; Grierson, P.F.G.; Baker, P. Drought variability in the eastern Australia and New Zealand summer drought atlas (ANZDA, CE 1500–2012) modulated by the Interdecadal Pacific Oscillation. *Environ. Res. Lett.* **2015**, *10*, 124002. [CrossRef]
48. MAF. *Regional and National Impacts of the 2007–2008 Drought*; Butcher Partners Ltd.: Tai Tapu, New Zealand, 2009.
49. Kamber, G.; McDonald, C.; Price, G. *Drying Out: Investigating the Economic Effects of Drought in New Zealand*; Reserve Bank of New Zealand: Wellington, New Zealand, 2013.
50. Mullan, B.; Porteous, A.; Wratt, D.; Hollis, M. *Changes in Drought Risk with Climate Change*; National Institute of Water & Atmospheric Research: Wellington, New Zealand, 2015.
51. Clark, A.; Mullan, B.; Porteous, A. *Scenarios of Regional Drought under Climate Change*; National Institute of Water & Atmospheric Research: Wellington, New Zealand, 2011.
52. Edwards, D.; McKee, T. *Characteristics of 20th Century Drought in the United States at Multiple Scale*; Atmospheric Science Paper 634; Department of Atmospheric Science Colorado State University: Fort Collins, CO, USA, 1997.
53. Bonaccorso, B.; Bordi, I.; Cancelliere, A.; Rossi, G.; Sutera, A. Spatial variability of drought: An analysis of SPI in Sicily. *Water Resour. Manag.* **2003**, *17*, 273–296. [CrossRef]
54. Angelidis, P.; Maris, F.; Kotsovinos, N.; Hrissanthou, V. Computation of drought index SPI with Alternative Distribution Functions. *Water Resour. Manag.* **2012**, *26*, 2453–2473. [CrossRef]
55. Thom, H.C.S. A note on the gamma distribution. *Mon. Weather Rev.* **1958**, *86*, 117–122. [CrossRef]
56. Abramowitz, M.; Stegun, I.A. *Handbook of Mathematical Functions with Formulas, Graphs, and Mathematical Tables*; Dover Publications, INC.: New York, NY, USA, 1970.
57. Oliver, J.E. *Encyclopedia of World Climatology*; Springer: Amsterdam, The Netherlands, 2005.
58. NIWA. Overview of New Zealand Climate. Available online: http://www.niwa.co.nz/education-and-training/schools/resources/climate/overview (accessed on 26 February 2018).
59. Salinger, M.J.; Mullan, A.B. New Zealand climate: Temperature and precipitation variations and their links with atmospheric circulation 1930–1994. *Int. J. Climatol.* **1999**, *19*, 1049–1071. [CrossRef]
60. Griffiths, G.M.; Salinger, M.J.; Leleu, I. Trends in extreme daily rainfall across the South Pacific and relationship to the South Pacific Convergence Zone. *Int. J. Climatol.* **2003**, *23*, 847–869. [CrossRef]
61. Dravitzki, S.; McGregor, J. Extreme precipitation of the Waikato region, New Zealand. *Int. J. Climatol.* **2011**, *31*, 1803–1812. [CrossRef]
62. Caloiero, T. Analysis of daily rainfall concentration in New Zealand. *Nat. Hazards* **2014**, *72*, 389–404. [CrossRef]

63. Caloiero, T. Analysis of rainfall trend in New Zealand. *Environ. Earth. Sci.* **2015**, *73*, 6297–6310. [CrossRef]
64. Caloiero, T. Drought analysis in New Zealand using the standardized precipitation index. *Environ. Earth. Sci.* **2017**, *76*, 569. [CrossRef]
65. Caloiero, T. Trend of monthly temperature and daily extreme temperature during 1951–2012 in New Zealand. *Theor. Appl. Climatol.* **2017**, *129*, 111–117. [CrossRef]
66. Wang, G. Agricultural drought in a future climate: Results from 15 global climate models participating in the IPCC 4th assessment. *Clim. Dyn.* **2005**, *25*, 739–753. [CrossRef]

# 4

# Fatalities Caused by Hydrometeorological Disasters in Texas

**Srikanto H. Paul *, Hatim O. Sharif and Abigail M. Crawford**

Department of Civil and Environmental Engineering, University of Texas at San Antonio, San Antonio, TX 78249, USA; hatim.sharif@utsa.edu (H.O.S.); amc1591@gmail.com (A.M.C.)

* Correspondence: srikanto.paul@utsa.edu

**Abstract:** Texas ranks first in the U.S in number of fatalities due to natural disasters. Based on data culled from the National Oceanic and Atmospheric Administration (NOAA) from 1959 to 2016, the number of hydrometeorological fatalities in Texas have increased over the 58-year study period, but the per capita fatalities have significantly decreased. Spatial review found that non-coastal flooding is the predominant hydrometeorological disaster in a majority of the Texas counties located in "Flash Flood Alley" and accounts for 43% of all hydrometeorological fatalities in the state. Flooding fatalities occur most frequently on "Transportation Routes" followed by heat fatalities in "Permanent Residences". Seasonal and monthly stratification identifies Spring and Summer as the deadliest seasons, with the month of May registering the highest number of total fatalities dominated by flooding and tornado fatalities. Demographic trends of hydrometeorological disaster fatalities indicated that approximately twice as many male fatalities occurred from 1959-2016 than female fatalities, but with decreasing gender disparity over time. Adults are the highest fatality risk group overall, children are most at risk to die in flooding, and the elderly at greatest risk of heat-related death.

**Keywords:** natural hazards; weather disasters; hydrometeorological fatalities; flooding; tornadoes; extreme temperatures

## 1. Introduction

Hydrometeorological disasters can result in tremendous damage to infrastructure, significant loss to the economy, and, very often, loss of life. In terms of the human loss, natural disasters resulted in approximately 1.7 million fatalities between 1980 and 2016. More than 49% of these fatalities were due to geophysical events (earthquake, tsunami, volcanic activity), 26% were due to meteorological events (tropical storm, extratropical storm, convective storm, local storm), 14% were due to hydrological events (flood, landslides), and 11% were due to climatological events (extreme temperature, drought, forest fire). Slightly less than 80% of the 16,500 disaster events that caused fatalities were hydrological or meteorological (39%) [1].

Although more research is beginning to shift to multi-hazard analysis [2,3], much of the available natural disaster research focuses on a particular type of disaster (e.g., floods, hurricanes, lightning, earthquakes) or disaster event (e.g., Hurricane Harvey, Northridge Earthquake). The focus on key disaster events is advantageous in that a deeper dive can benefit the preparation and mitigation strategies in the affected areas. Flooding is an exemplary disaster type that is responsible for high fatality rates and has been extensively investigated on a global [4–7] and national scale including the U.S. [8], India [9], Pakistan [10], and Australia [11]. It is also of value to focus at the regional level or the effects of one type of hazard to provide a basis for better allocation of resources to prepare for high risk hydrometeorological disasters with high probability of impact to a specific region.

This study analyzes fatality rates resulting from multiple hydrometeorological disasters that affect the state of Texas at the county level. Texas has a long history of devastation by natural disaster

(especially hydrometeorological disasters). The most lethal natural disaster in United States history occurred in Galveston Island, Texas in 1900 in which an estimated 6000–12,000 people died as a result of the "Great Galveston Hurricane". From January 1960 to December 2016, Texas had the highest number of fatalities in the nation in which natural disasters killed an average of 40 people per year [12]. During this period, Texas accounted for 7.4% of all U.S. fatalities (32,289). Flood, heat, and tornado accounted for 60% of all fatalities in Texas during this period. Texas also ranks highest in fatalities per capita (15 fatalities per 100,000 people). During this period two Texas counties ranked in the top ten across all states for the occurrence of disaster events: Harris County (1088 events) and Tarrant County (1009 events). Dallas County, Texas, ranked eighth in the number of fatalities in the U.S. Extensive research has been conducted to investigate the quantitative and qualitative aspect of flooding in the state of Texas [12,13].

Hurricanes are also a critical hydrometeorological disaster that claim many lives in Texas. In 2005, Hurricane Katrina struck the Louisiana coast causing $96 billion in damages and 1833 fatalities. Two-thirds of the fatalities were directly related to more than fifty breaches of the levee and floodwall systems [14]. Most recently in August 2017, Hurricane Harvey made the landfall near Port Aransas on the Gulf Coast as a category-4 storm with wind gusts up to 212 kph (132 mph) and resulted in $200 billion in damages and 103 confirmed deaths in Texas, primarily due to flooding across 11 counties. Thirty-six of the total 68 direct fatalities caused by the hurricane winds and flooding occurred in Harris County (Houston Metropolitan area) [15].

Tornadoes were responsible for 14% of the total number of natural disaster-related fatalities in the U.S. from 1960 to 2015 [16]. Texas leads the nation in the average number of tornadoes between 1991 and 2010 with 155 tornadoes per year followed by Kansas (96), Florida (66) and Oklahoma (62) [17]. Analysis of tornado-induced fatalities and damage in the U.S. between 1880 and 2005 in 2007 identified 1812 tornado-related fatalities caused by 366 fatal tornado events mostly along the northeastern border of the state [18]. The normalized fatality rate per tornado event in Texas is in line with the national normalized averages (2.7 fatalities and 0.54 events).

The impact of disastrous extreme weather to society is a function of both the climatic and local setting. For example, although both the fatality rate and the extent of damage to infrastructure have increasing trends from the 1960′s to the present, some studies suggest that population growth and demographic shifts play a greater role in the degree of increase than the increase in intensity and/or frequency of the extreme weather that the Earth has been experiencing in the last several decades [19]. This would suggest that even without any detrimental climate changes, the shifts in U.S. economic development patterns and growth will result in ever increasing losses caused by hydrometeorological disasters. Therefore, it is necessary to recognize spatial and temporal trends of natural disasters to allow for the allocation of resources to the higher risk disasters and their locations.

Supplemental to the intensity of such hazards is the exposure of people in the affected areas. In the last several decades, the U.S. has experienced steady increases in population shifts in rural and coastal development patterns, and economic growth, which have positioned more people in disaster-prone areas [20]. Research on the October 2015 flood event in Columbia, SC, indicated that considerations for public safety were sometimes secondary to profitable land development [21]. Hurricane research that was published in 2018 analyzed the decision biases of persons affected by hurricanes and found that temporal band spatial myopia is a major issue that places a lower priority on long-term decisions (e.g., preparation) than short term routine tasks with the failed intention of addressing the long term need when the disaster event is closer in time [22].

The purpose of this paper is to analyze the fatality rates caused by hydrometeorological disasters in Texas for the period 1959–2016 in an effort to identify counties and metropolitan areas in Texas that have a greater risk for particular hydrometeorological disasters. The hydrometeorological disasters were categorized into "Flooding", "Heat", "Cold Weather", "Tornado", "Lightning", and "Wind Events". Fatalities due to "Tropical Events" (hurricanes and tropical storms) were either classified as flooding or wind events depending on the cause of fatality. The study examines temporal

trends, spatial variations, and demographic characteristics of the victims. The paper concludes with a discussion and commentary of considerations that may influence the fatality rate with the goal of providing information and perspectives that would help reduce hydrometeorological disaster fatalities.

## 2. Materials and Method

### *2.1. Study Area*

Texas is the second largest state in the U.S., both in terms of population and area, with a population of 27,862,596 and a land area of 695,662 km$^2$. The southeast of Texas shares 591 km (367 miles) of coastline with the Gulf of Mexico and is susceptible to hurricanes and coastal flooding. A major topographical feature that affects the number of hydrometeorological disasters in Texas is the Balcones Escarpment that consists of a series of cliffs dropping from the Edwards Plateau to the Balcones Fault Line. As noted in an article from the Texas Hill Country magazine published in 2016, "This outer rim of the Hill Country is the formation point for many large thunderstorms, which frequently stall along the uplift and then hover over this region" [23]. The "Flash Flood Alley" includes counties having the fastest population growth rates in Texas.

### *2.2. Data Source*

The Texas hydrometeorological disaster fatality information reviewed in this study was culled from the National Oceanic and Atmospheric Administration (NOAA) *Storm Data* reports for the period January 1959 through December 2016 [24]. From 1959–1995, the data were only available via PDF files. Disaster data from 1996–2016 were available via the NOAA searchable database. The data in the *Storm Data* Publication relies on self-reporting from individual states and counties and is dependent upon the verification and validation of the reporting agency. The *Storm Data* had some inconsistencies from year to year and county to county in the classification of the causes of fatalities. For example, deaths by lightning are classified as either electrical deaths or lightning deaths. Similarly, wild fires or prairie fires are listed under either wind events or wildfire events in the database. Heat-related deaths from the homeless or illegal immigrants in rural counties also have a potential to be under-reported since the location of the victims may remain undetected. As an example of a potential under-reporting condition, the *Storm Data* indicates that before 2008 there were no deaths due to heat exposure discovered along the border of Texas and Mexico. This is unlikely given that the U.S. Customs and Border Protection indicate that 7216 people have died from exposure attempting to cross the U.S./Mexico border between 1998 and 2017 [25]. In 2005 alone, more than 500 people died attempting to across the U.S./Mexico border [26]. Fatality information was also reviewed from the Hazards Vulnerability Research Institute (HVRI), U.S Hazard Losses Summary Report (1960–2015), to provide perspective for large scale comparisons of trends between Texas and the national fatality rate [16]. The HVRI data was not used in the numerical analysis of spatial and temporal trends forming the basis of this paper.

### *2.3. Methodology*

Differences in the terminology exists across varying literature sources as it pertains to the effects of natural hazards and disasters on people and the land. This study defines a hazard as a natural event that has the potential to cause harm and a disaster as the effect of the hazard on humanity. Hydrometeorological disasters are defined as "natural processes or phenomena of atmospheric, hydrological or oceanographic nature" [27]. The Texas fatality data used in this study were all caused by hydrometeorological disasters. If the disaster did not result in at least one fatality it was not included. The fatalities also did not have to result from a disaster that was classified through a formal disaster declaration. The definitions of the descriptors and disaster types used in this study for the database files (1996 onward) and the manually aggregated fatality data prior to 1996 are in agreement with the NWS Directive 10-1605 [28].

Only fatalities that were classified as being directly caused by the incident are included in the study. *Storm Data* lists each incident with the date, time, the number of people who died in the incident, the number of people injured, and a brief description of the event. The descriptive narratives provided along with each event were used to get information related to the gender, age, activity, mode of transport, and location of the individual who died. In 1996 and after, the database provided an accompanying chart of the victims. The chart listed the victim's age, gender, and location. If there was a disparity between the description and the accompanying table, the information in the description was used since the descriptions were often retrieved from the police report that was filed with the death.

The data analysis includes temporal and spatial trending using linear trendlines and correlation analysis to verify statistical significance. Moving 10-year averages were also included to in the temporal distribution to support the linear trending. Spatial analysis by county used the ArcGIS (v.10.4) (Esri, Redlands, CA, USA) to generate thematic maps. Fatality rates were normalized by annual population for temporal trends and by the study period median population for the spatial distribution by county. Percentages were generally rounded to the nearest whole number unless otherwise necessary for comparative analysis.

## 3. Results

### *3.1. Types of Hydrometeorological Disasters*

The *Storm Data* reports 55 disaster event types. For purposes of this study the disaster fatalities reported in Texas from 1959 to 2016 were categorized into one of the following nine hydrometeorological disaster types based on the information provided in the incident report or the NOAA database (Table 1). The definitions are consistent with the general classifications of weather disasters as defined by the National Weather Service.

**Table 1.** Definitions of Hydrometeorological Disaster Types.

| Disaster Type | Characteristics |
|---|---|
| Flooding | Floods and flash floods due to extreme rain caused by hurricanes *, tropical storms, or other rain storm events |
| ** Tornado | Wind event meeting the minimum classification of wind speed and ground contact |
| Lightning | Natural high voltage electrical discharge from atmosphere striking person or surface in proximity of person |
| Heat | Prolonged period of time with extremely high average temperature usually accompanied by drought |
| Cold Weather | Blizzards, snow storms, ice storms, and prolonged period of time with extremely low average temperatures |
| Wind | Extreme high winds causing damage but not meeting the minimum criteria of hurricanes or tornados |
| Other | Hail, water spouts, wildfires, or rain that directly resulted in some major structural damage (e.g., roof collapse) |
| Rip Current | Coastal specific disaster that includes people killed (drowned) in rip currents. Rip currents have only been tracked as of 1997 |

* The Saffir–Simpson hurricane wind scale (SSHWS), classifies hurricanes as Western Hemisphere tropical cyclones that exceed the intensities of tropical depressions and tropical storms with sustained winds of at least 74 mph (Category 1). ** The Enhanced Fujita scale (EF) classifies tornadoes based on wind speed and damage (once they have touch ground) from EF-0 (65–85 mph) to EF-5 (>200 mph).

Approximately 80% (205 of the 254) of the counties in Texas reported hydrometeorological fatalities in at least one year during the 58-year study period. Figure 1 shows the primary type of disaster that resulted in fatalities for each Texas county. Seventy-seven of the 205 counties that reported

fatalities indicated that flooding was the primary disaster in their county. Thirty-one counties had more than one predominant cause of fatality and so were not categorized as primary disaster.

Counties that reported deaths due to flooding as the predominant hydrometeorological disaster are clustered towards the central region of the state and extend west towards Mexico/New Mexico in the region known as Flash Flood Alley. The disasters that caused the greatest number of fatalities along the Gulf Coast of Texas were wind events and lightning (Figure 1). Heat-related fatality counties were scattered in 11 counties across Texas and 75% of the cold weather fatality counties were in the northwest of Texas (Texas Panhandle) above the 34° N latitude. Fatalities due to tropical events (hurricanes and tropical storms) were all determined to be a result of subsequent flooding and therefore classified as flood-related fatalities. Death due to heat-related events was predominant in Harris County, the most populated county in Texas.

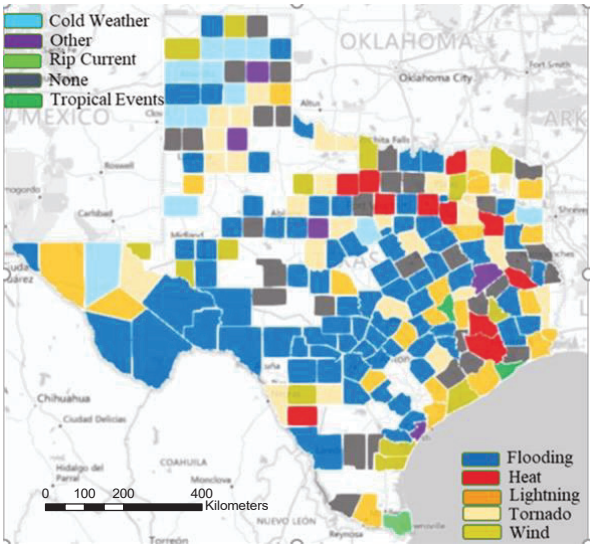


**Figure 1.** Primary disaster resulting in largest number of deaths per county. Dark grey: no one predominant disaster. Light grey: No hydrometeorological disaster fatalities reported.

A total of 2330 natural disaster-related fatalities occurred in Texas from 1959 to 2016 with 43% due to flooding (991 fatalities) as shown in Table 2. The second most frequent cause of fatalities was extreme heat (16%) followed by tornados (14%) and lightning (10%). The single most fatal natural disaster event during this 58-year period was the tornado of April 1979 that struck Wichita and Wilbarger counties killing 54 people and injuring 1807. This was an EF-4 (Enhanced Fujita scale) tornado with a maximum width of 2.5 km that killed four people along it's northeastern track through the states of Oklahoma (3 deaths) and Indiana (1 death). Seventy-nine percent (79%) of the total tropical storm-related fatalities were caused by hurricanes (108 deaths).

**Table 2.** Hydrometeorological Disaster Fatalities, source: NOAA (National Oceanic and Atmospheric Administration) *Storm Data* [24].

| Disaster Type | Fatalities | % Total |
|---|---|---|
| Flooding * | 991 | 42.5 |
| Heat | 378 | 16.2 |
| Tornado | 333 | 14.3 |
| Lightning | 222 | 9.5 |
| Wind | 172 | 7.4 |
| Cold Weather | 160 | 6.9 |
| Other | 43 | 1.9 |
| Rip Current | 31 | 1.3 |
| **Total** | **2330** | **100** |

* Includes fatalities due to hurricanes and tropical storms.

### *3.2. Temporal Distribution*

#### 3.2.1. Annual Distribution of Fatalities

An average of 42 fatalities per year occurred in Texas from 1959 to 2016 with a median of 33 fatalities per year and a total of 2330 hydrometeorological fatalities. The difference between the mean and the median indicates that the annual distribution is positively skewed with long tail in the right direction (towards higher numbers). Although, the raw number of fatalities exhibits a slight increasing trend during the study period, the trend has low linearity ($R^2 = 0.0369$, $p = 0.233$) and the relationship of fatalities over time is statistically weak (Spearman's $p = 0.16$). The lowest number of fatalities (6) occurred in 1963 and the highest number of fatalities (118) occurred in 1998 (Figure 2). Eleven of the 58 years had an annual number of fatalities greater than the 58-year mean plus one standard deviation ($40 \pm 24$).

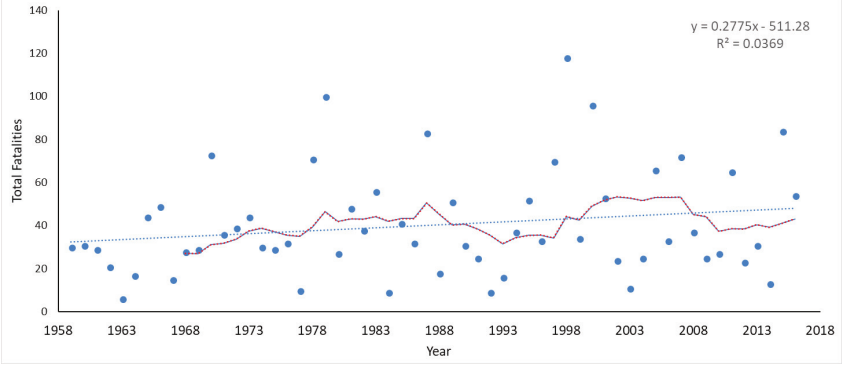


**Figure 2.** Total Fatalities from natural disasters in Texas from 1959 to 2016 with 10 year rolling average (red dashed line). The solid line represents the linear trend.

The curve of the cumulative annual fatality rate is relatively uniform with two observable spikes in 1978–1979 and 1998 driven by high fatalities resulting from heat and flooding events (Figure 3). Specifically, in 1978 Dallas County had 21 heat-related fatalities and 40 flooding fatalities that occurred in several counties including Bexar, Kerr, Shackelford, Bandera, and Randall counties. From May 1997 to August 1998 a severe heat event hit the southern region of the U.S. from Florida through Texas and

into Colorado. Conversely, several flooding events in November 1998 resulted in fatalities in Bexar, Val Verde, Caldwell, Guadalupe, and Real counties.

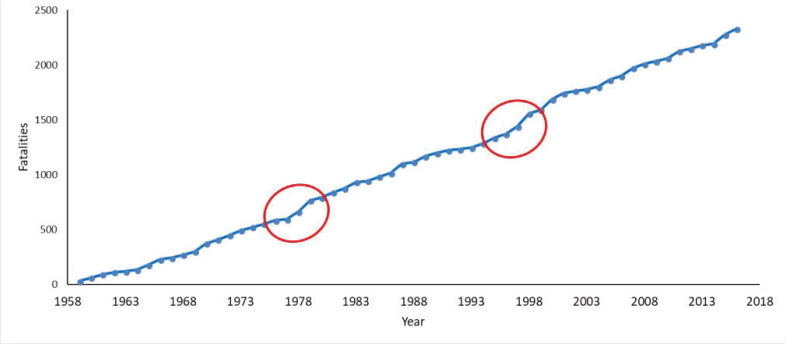


**Figure 3.** Cumulative number of fatalities (all disasters).

Normalization of the annual fatality rate by population indicates a decreasing trend with slightly better linearity ($R^2 = 0.096$, $p = 0.006$) than the raw trend and a stronger statistically relationship of fatalities over time (Spearman's $\rho = -0.355$) which suggests a gradual decrease in the risk of being killed by hydrometeorological events in Texas over the 58-year study period. The normalized fatality trend can be seen in (Figure 4), which shows the fatality rate due to hydrometeorological disasters per 100,000 Texas residents. Public awareness and educational weather safety campaigns in Texas may have contributed to this reduction of risk [13]. Although the rank order of counties by number of raw fatalities aligns with the highest populated urban centers, these regions are not necessarily the most dangerous. This is evidenced in that several of the counties in immediate proximity to the counties that experienced high fatality have very few fatalities even though the intensity and durations of the disasters were probably very similar between the counties.

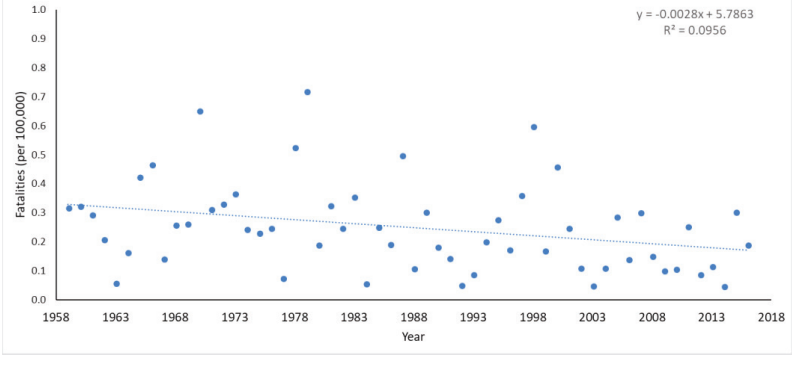


**Figure 4.** Normalized Fatality Rate from hydrometeorological disasters in Texas from 1959 to 2016. The solid line represents the linear trend.

For example, Loving County has the highest normalized fatality rate (> 4000 per 100,000) in the state due to its small and stagnant population and the fact that the county experienced several multi-fatality events of wind and hailstorm that struck the Red Bluff Lake area killing four persons by drowning when their boat capsized in the lake during a squall. Similarly, on 11 June 1965,

the city of Sanderson in Terrell county was devastated by a flash flood. As noted by the Texas State Historical Association, "A wall of water washed down Sanderson Canyon into Sanderson, destroying numerous homes and businesses. Twenty-six people died in the flood. Eleven flood-control dams were constructed to protect Sanderson against another such catastrophe" [29]. The town had a population of 1500 in 1980 and 1128 in 1990. Reduction of fatality risk in these rural counties will require an increase in awareness through weather-related emergency educational programs and resource assistance (financial and physical) to implement safety systems.

The annual fatality rate by disaster type from 1959 to 2016 for six of the eight disaster types is shown in Figure 5. There seems to be a shift in the number of fatalities at the middle of the study period, especially for tornadoes and lightning. Splitting the study period into two equal parts (1959–1987 and 1988–2016) shows the first half having a greater proportion of the total fatalities for all disasters except for heat-related events. Heat-related events show an increasing trend of 0.45 fatalities per year ($R^2 = 0.54$) from 1978 to 2016 with no data available prior to 1978. Eighty-nine percent (89%) of all heat-related fatalities (335 out of 378) occurred after 1994. The increasing trend in heat fatalities is likely a compounded effect of higher than normal average air temperatures, the urban heat island effect, and increasing population in the urban regions. The retention of heat due to the abundance of non-natural building materials results in higher temperatures in the urban center than the surrounding area. As population increases in urban centers and higher temperatures the result will be increased heat fatalities especially for the most physically vulnerable such as the elderly. As noted in Figure 11, heat fatalities occur inside permanent residences about 50% of the time. This statistic is probably a conservative estimate since heat deaths may be under-reported for a variety of reasons. Exposure to extreme heat can cause cardiac or respiratory issues that can be fatal. Therefore, the judgment of the medical professional determines the cause of death as exposure to heat or the underlying medical condition. External factors also may contribute to under-reporting variability of heat fatalities especially along the U.S./Mexico border counties and in the case of chronically ill victims where it is unclear the final cause of death. Immigrant deaths along the border are uncertain due to international policy challenges.

The difference between the early and the latter half of the study period was highest for tornadoes with 71% in the first half of the study, followed by 68% for wind, 63% for cold weather, 62% for Lightning, 57% of tropical storms, and 52% for flooding. Not all years of the 58-year study experienced fatalities from all of the hydrometeorological disasters. Fatalities due to flooding. lightning and wind events were the most consistent occurring in 57, 56, and 47 of the 58 years respectively. Fatalities due to tornadoes, cold weather and heat events occurred in 41, 38, 26 of the 58 years respectively. The year 2011 was the only year that had no reported flood-related fatalities and was also the year that experienced one of the worst droughts in Texas history. Trend analysis over the entire 58-year period indicates statistically significant change (decreasing) for flooding ($R^2 = 0.112$, $p = 0.0104$), wind ($R^2 = 0.190$, $p = 0.0006$), lightning ($R^2 = 0.346$, $p = 1.21 \times 10^{-6}$), and an increasing trend for heat ($R^2 = 0.087$, $p = 0.0243$). Fatality trends due to tornadoes ($R^2 = 0.043$, $p = 0.1190$), and cold ($R^2 = 0.009$, $p = 0.4770$), exhibited slight downward trends but were not statistically significant.

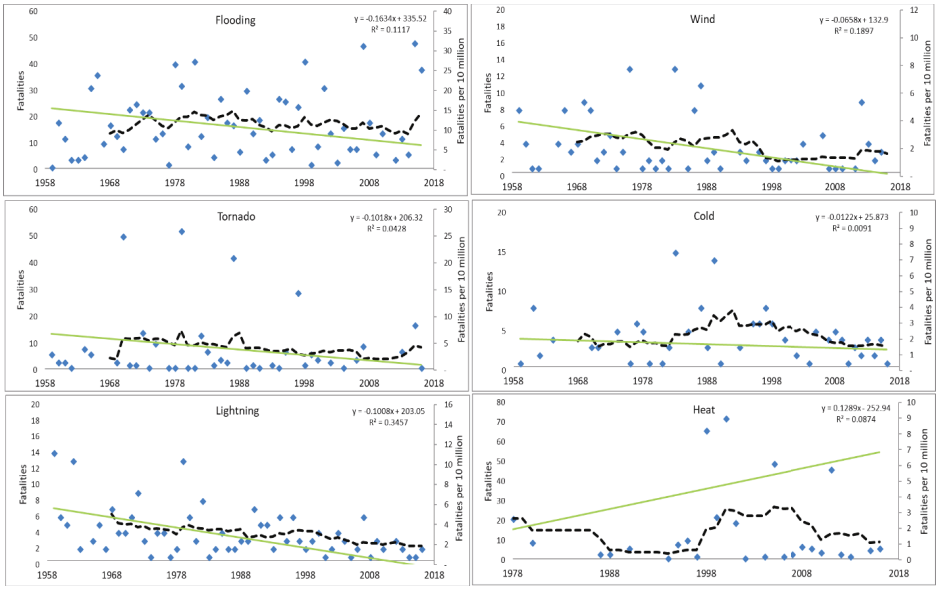


**Figure 5.** Annual fatality rate in Texas for six disaster types: flooding, wind, tornado, cold, lightning, and heat: 10-year rolling average (dashed line) and normalized (fatalities per 10 million) trend line (green solid). Note: Heat fatalities are reported from 1978 to 2016.

Fatalities due to tropical events (hurricanes and tropical storms) were mostly due to drowning and therefore were integrated into the flooding fatalities unless there was a clear distinction in the fatality record. Only seven tropical event fatalities occurred during the period 2003–2007. The disaster category "Other" includes wildfires and other secondary perils that do not frequently result in death, such as hail, water spouts, or rain that resulted in roof collapse. The "Other" disaster category indicated 71% of the years (41 out of 58 years) had zero fatalities with a steady increase in the fatality rate starting in 2004. Eighty-one percent (81%) of fatalities of this category occurred in 13 years between 2004 and 2016. Rip currents were added to the *Storm Data* in 1998. The first reported fatalities occurred in 2007 with two total fatalities at 31 deaths from 2007 to 2016 with an average of 3.4 per year and a high of 8 deaths in 2011. Five of the 8 deaths were Mexican immigrants visiting the coastal county of Cameron. More years of rip current fatality data is needed to establish any definitive temporal or spatial trends.

### 3.2.2. Monthly Distribution of Fatalities

The monthly fatality rate due to hydrometeorological disasters illustrates the seasonal variability in the number of fatalities for different types of disasters (Figure 6). A distinct peak is noticeable in May driven by flooding and tornado fatalities, which are responsible for 80% of the fatalities in the month. During the summer months, most fatalities were due to heat events while spring fatalities result primarily from flooding. Flooding fatalities were highest in the months of May, June, and October with 22%, 17%, and 13%, respectively of the total flood-related fatalities. Some disaster-related fatalities are obviously limited to certain seasons such as cold weather fatalities that occur in Winter (85% of all cold weather-related deaths occurred in December, January and February). Seventy one percent (71%) of all fatalities occurred in spring and summer with an even split between the two seasons.

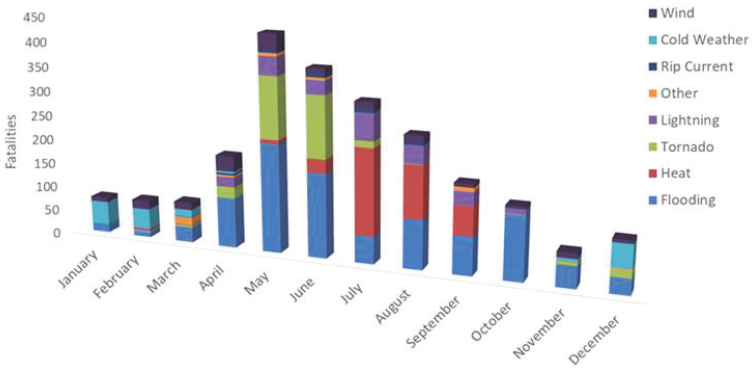


**Figure 6.** Monthly distribution of hydrometeorological disaster fatalities (all fatalities).

A grouping of the months into four seasons, Winter (December, January, February); Spring (March, April, May); Summer (June, July, August) and Fall (September, October, November), highlights the difference in rolling average fatality rates between the first half of the study period to the second half (Figure 7). The rolling averages show a slight decrease for spring and winter and increase in summer and fall with the largest difference observed in summer due primarily to an increase in heat-related fatalities that occurred between 1998 and 2008. Comparatively, all of the normalized trends for the four seasons have a decreasing trend winter (m = −0.0008, $p$ = 0.687), summer (m = −0.0037, $p$ = 0.600), fall (m = −0.0022, $p$ = 0.563) with only the spring fatality trend (m = −0.0211, $p$ = 0.019) having statistical significance.

3.2.3. Distribution of Fatalities by Time of Day

Time of day was provided for 68% of the hydrometeorological fatalities culled from the *Storm Data*. Each time of death was assigned to one of the four periods in a day: morning (6 a.m.–12 p.m.), afternoon (12 p.m.–6 p.m.), evening (6 p.m.–12 a.m.), and night (12 a.m.–6 a.m.). Of the fatalities with known time of death, 36% occurred in the afternoon, 26% in the evening, 21% in the morning, and 18% at night. Eighty percent (80%) of the fatalities with unknown time of the day were caused by flooding or heat-related events. Fifty percent (50%) of the total fatalities (562) that occurred in the afternoon were due to tornadoes and flooding. Detailed analysis shows that flooding events have a slightly higher chance of causing death at night or in the morning hours. However, tornados are much more likely to fatally strike in the afternoon/evening hours (Figure 8).

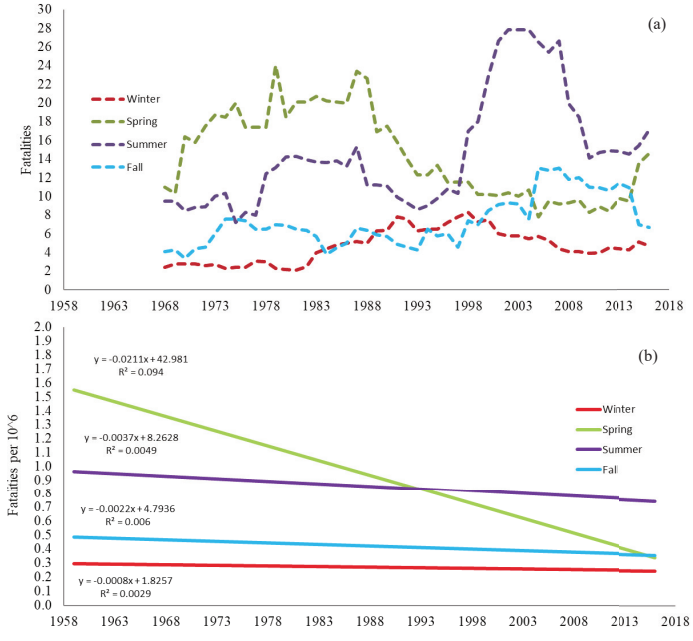


**Figure 7.** (**a**) Number of total fatalities (rolling 10-year averages) by season; (**b**) Normalized fatality rates by season.

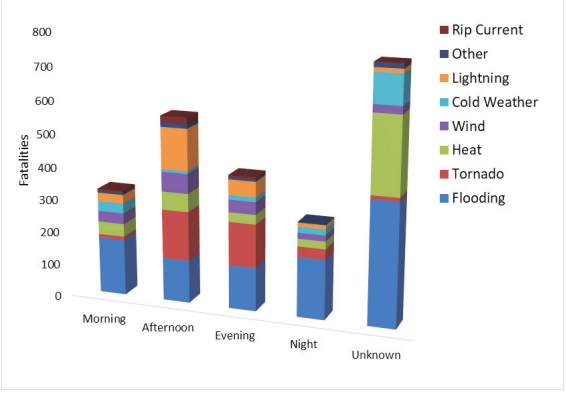


**Figure 8.** Distribution of hydrometeorological disaster fatalities by time of day.

### *3.3. Spatial Distribution*

Most hydrometeorological fatalities occurred in populated counties (Harris (Houston), Bexar (San Antonio), Dallas and Tarrant (Dallas area), Travis and Williamson (Austin) as well as rural counties in west Texas with low populations high fatality numbers are noted in the Flash Flood Alley counties and some coastal counties (Figure 9).

Table 3 provides the ranking of the top 5 counties with the highest number of hydrometeorological disaster fatalities which combined, account for 32% of the total hydrometeorological disaster fatalities. Slightly more than 3% of the total reported fatalities did not include county information.

Forty-eight percent (48%) of the fatalities in Harris County were caused by heat-related events followed by flooding (33%) and lightning (11%). Heat events also caused the highest percentage of deaths (50%) in Dallas County followed by flooding (29%). Bexar County ranked third with 103 fatalities of which 82% were caused by flooding making Bexar the county the most dangerous in the state for death from flooding (per capita).

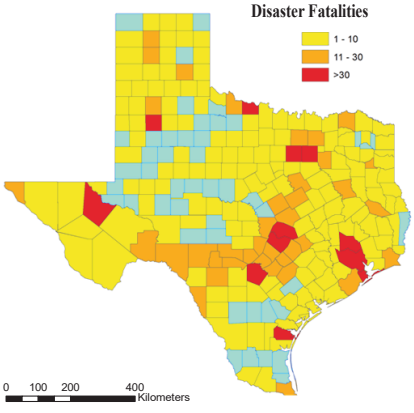


**Figure 9.** Raw number of hydrometeorological disaster fatalities by county.

**Table 3.** Top 5 Texas counties (Raw Fatality Rate). source: NOAA *Storm Data* (1959–2016) [24].

| Rank | County | Fatalities |
|---|---|---|
| 1 | Harris | 259 |
| 2 | Dallas | 228 |
| 3 | Bexar | 103 |
| 4 | Tarrant | 87 |
| 5 | Travis | 76 |

The top 5 counties within each hydrometeorological disaster type represent a significant percentage of the overall fatality rate within each of the category ranging from a high of 76% of all heat-related fatalities to a low of 28% of all wind event fatalities (Table 4). Dallas County is in the top five for six of the eight disaster types (heat, flooding, lightning, cold, wind, and others not shown in table). Harris is the only county that tops the list for more than one type of disaster and ranks number one for heat, flooding, and lightning fatalities and ranks second in wind fatalities. The top counties with the highest number of fatalities (and most populated counties) identified in Table 3 also dominate the top 5 ranking of counties in Table 4 for flooding, lightning and heat fatalities. Interestingly, although flooding is responsible for 43% of all disaster fatalities in the state, the top five counties only account for 34% indicating that flooding fatalities are extant over a high number of counties.

**Table 4.** Top 5 Texas counties with highest fatality rate (and % of total) by hydrometeorological disaster. source: NOAA *Storm Data* (1959–2016) [24].

| Heat (76%) | | Tornado (45%) | | Wind (28%) | | Flooding (34%) | | Lightning (31%) | | Cold (30%) | |
|---|---|---|---|---|---|---|---|---|---|---|---|
| Harris | 124 | Wichita | 47 | Nueces | 16 | Harris | 85 | Harris | 29 | Dallas | 16 |
| Dallas | 113 | Reeves | 30 | Harris | 10 | Bexar | 84 | Jefferson | 12 | Potter | 12 |
| Tarrant | 22 | Williamson | 29 | Dallas | 8 | Dallas | 65 | Dallas | 11 | McLennan | 7 |
| Montgomery | 16 | Lubbock | 26 | Brazoria | 7 | Travis | 59 | Tarrant | 9 | Tarrant | 7 |
| Travis | 12 | Donley | 17 | Denton | 7 | Tarrant | 43 | Bexar | 8 | Castro | 6 |

*3.4. Fatalities by Age and Gender*

Age was provided for 57% of the total reported deaths (1333 fatalities) in which "Adults" made up 52%, the "Elderly" 28%, and "Children" 20% of the known age fatalities. In this study, "Children" are defined as newborns up to 17 years, "Adults" from 18 years to 64 years, and "Elderly" as persons above 65 years of age. Adults made up 53% and children made up 27% of all flooding fatalities. This fatality statistic requires more data (age aggregation) and further research into the specifics of the situation before any defensible conclusions can be drawn. On open conjecture it can be suggested that flooding is responsible for death of families which typically includes a higher number of children than adults that either did not evacuate or were killed during the evacuation process on transportation routes. Comparing the number of fatalities and the number of people in each age group provides a measure of relative risk of death within each age group. Using the 1990 census population in each age group: children (4,857,469), adults (10,420,598), and elderly (1,708,443) the relative risk of fatality for all hydrometeorological disasters during the period covered by this paper indicates a similar risk between children (0.006%) and adults (0.007%). But the risk of the elderly dying is more than three times the level at 0.022% due to the much lower elderly population (approximately 10% of total population). The elderly were mostly at risk for heat events, accounting for 52% of all heat-related fatalities (Figure 10).

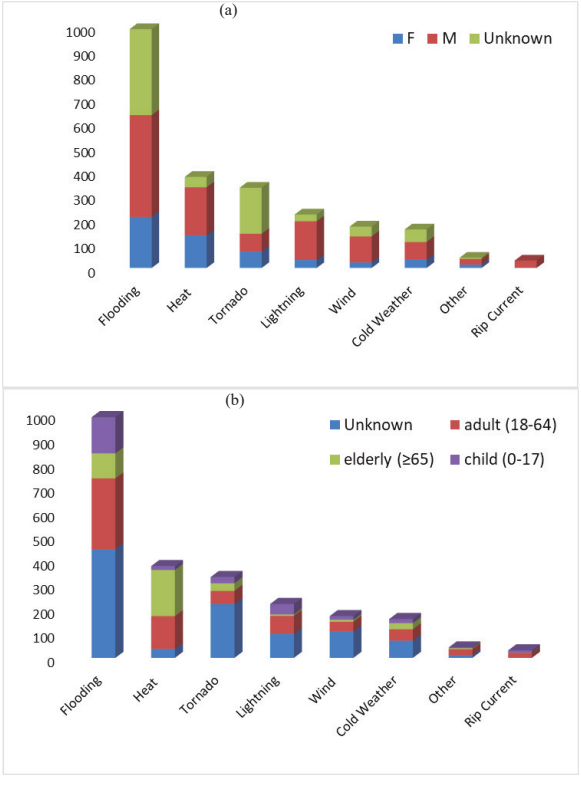


**Figure 10.** Total natural disaster fatalities considered in this study classified (**a**) by gender and (**b**) by age group

The gender of the victim was provided in 69% of the reported fatalities. Among those, males made up 68% and females 32% representing an approximate ratio of 9:5. This gender disparity has also been observed in other research, for example in flood-related fatalities [12,13,30,31] and in lightning-related fatalities [32–35]. In all cases there was a high male to female ratio of fatalities. For the current study, the ratio of male to female fatalities is approximately 2:1. The greatest disparity was found in wind and lightning fatalities that show a 5:1 ratio of male to female fatalities. Rip currents have only been tracked since 1998 but the data thus far indicates a 30:1 ratio of male to female fatalities.

### *3.5. Fatalities by Activity Location*

The *Storm Data* describes 18 potential activity fatality locations. For purposes of this study each of the disaster events reported in Texas from 1959 to 2016 was categorized within one of the following nine locations identified in based on the information provided in the incident reports (Table 5).

**Table 5.** Definitions of Hydrometeorological Disaster Fatality Locations.

| Location | Definition |
|---|---|
| In Water | Streams, river, bayous, oceans, floods, etc. and includes activities such as swimming, boating, surfing, and working on oil rigs |
| By Water | Boat docs, levies, beaches or other types of shoreline appurtenances |
| Temporary or non-Permanent Shelters | Tents, car ports, trees, and other temporary shelters that do not have a foundation (excluding umbrellas) |
| Outside | People who were outside but not in or near water, people standing in lawns, in construction sites that did not offer shelter, in ball fields, parks, golf courses, etc. People seeking shelter under umbrellas are also included. People standing/sitting near or on top of personal vehicles that are not along a transportation rout are included in outside (e.g., people walking from their home to their car who died before reaching their vehicle, people sitting on top of trucks in fields) |
| Transportation Route | Roadways, freeways or toll ways, parking lots, sidewalks or air travel routes. People walking along roads who hid behind a vehicle right before the disaster are categorized under transportation routes. Fatalities in vehicles were not assumed to be along transportation routes and were classified as unknown unless the description indicated a transportation route. Exclusion: people hiking or traveling along non-established routes by foot were not included in this category, and instead were classified as "outside" |
| Mobile Home | Standard and double-wide mobile homes |
| Permanent Residence | Domiciles that have a foundation, including but not limited to brick houses, frame houses, and apartment buildings |
| Public and Permanent Buildings | Schools, restaurants, airports, and other buildings with foundations that are not residences |
| Other/Unknown | All other locations not described by any of the other location categories listed or if the location was not specified |

The activity location in which the fatality occurred was provided in 75% of the total fatalities that were reported in Texas from 1959 to 2016. Figure 11 shows the stratification of fatalities by location of occurrence and disaster types considered in this study. Fatalities with known locations, occurred most often (38%) on transportation routes such as roadways, freeways or toll ways, parking lots, sidewalks or air travel routes. Automobile accidents are not categorized as transportation routes unless they were specified as such in the report. Eighteen percent (18%) of known location fatalities occurred in "Permanent Residence", followed by "Outside" and "In Water" at 16% and 15%, respectively. The high fatality rate in and around certain activity locations observed in Texas is also highlighted in research conducted in Switzerland for the period 1946–2015 [36] in which the researcher noted the greatest number of natural disaster fatalities occurring on transportation routes (33%), followed by in or around buildings and open terrain.

Sixty-five percent (65%) of fatalities on transportation routes were caused by flooding. This percentage is potentially underestimated since 65% of the fatalities in an unknown location were caused by flooding. As noted in other Texas flooding fatality studies [31] driving into flash flooding conditions is a significant occurrence that would make it very difficult to assign a location with no clear transportation route known. Also 25% of tornado fatalities are reported with an unknown location. Forty-eight percent (48%) of heat-related fatalities occurred in permanent residences. Tornados caused 73% of all hydrometeorological disaster fatalities reported in mobile homes. It must not be overlooked that the "Other" category included 11 deaths of children as result of being left in a car unattended and succumbing to heat exposure, a very preventable tragedy.

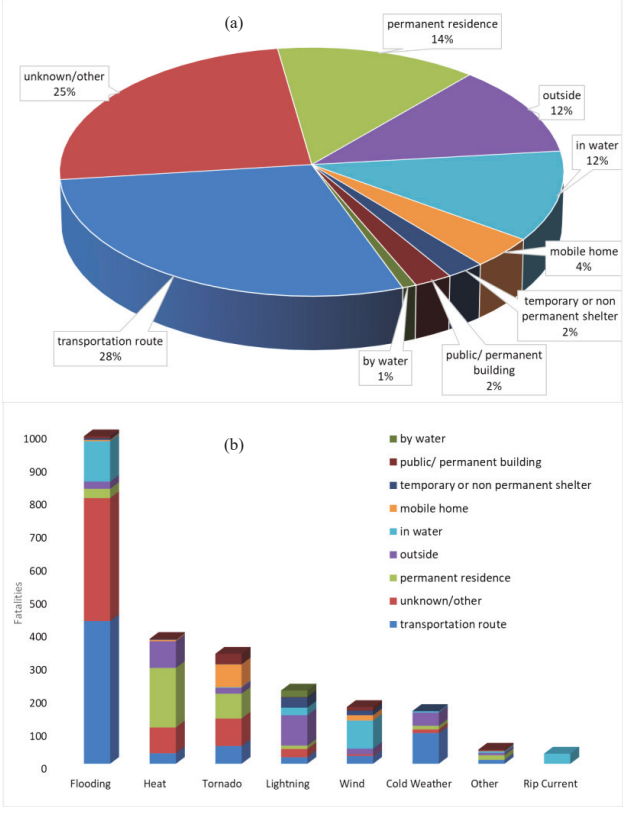


**Figure 11.** Hydrometeorological disaster fatalities classified (**a**) by reported location of occurrence and (**b**) by disaster type and location

## 4. Discussion

The predominant types of natural disasters in Texas that result in fatalities are those initiated by weather conditions such as flooding, tornadoes, and extreme temperatures. This study did not analyze the climate conditions or associate global warming to disaster events, but rather its intent was to analyze the spatial and temporal distribution of fatalities by disaster type. Regardless of the reasons for changes in frequency or intensity of the hydrometeorological disaster events, the parametric shifts can challenge the preparedness and resiliency of a region and in many cases impact the number of fatalities incurred. Analysis of these types of natural disaster trends based on historic data can enhance

predictability and preparedness planning to reduce the loss of life. Regional mortality and morbidity is also affected by the demographics and behavior of the people in the region of impact, specifically age, gender, and behavior patterns (location) have an observable relationship to the fatality rate due to hydrometeorological disasters.

*4.1. Population and Fatality Rates*

Texas exhibits regional variability in the hydrometeorological disaster fatality rate that is weighted to regions of high population. This suggests that as more people continue to move into populated urban areas or into regions that are at higher risk for hydrometeorological disasters such as flood plains, tornado alleys, or coastal regions, fatality rate will likely increase with or without an increase in the number of disaster events. Highly populated regions are more susceptible to a higher number of natural disaster fatalities than lower populated regions due to the sheer number of persons per area. As the population of Texas and the number of hydrometeorological disasters continues to increase, the result will likely be a continuing increase trend in the number of hydrometeorological fatalities. The current population growth rate for Texas is 1.8% which is the third in the U.S. According to the Texas Demographic Center [37], the vast majority of population growth since 1850 has occurred in metropolitan areas while the population in non-metropolitan counties has declined. This urban population increase coincides with an increasing trend of the annual fatalities as noted in Section 4.2.1.

The counties with the greatest population density: Harris, Dallas, Bexar, and Travis had the highest actual fatality rate, but each less than 15 fatalities per 100,000 persons over the study period. In contrast, some counties with lower populations had much higher per capita fatalities (higher risk for fatalities) although they were adjacent to the high population counties and experienced similar hydrometeorological disaster frequency and intensity. For example, Bexar county had 8.7 fatalities per 100,000 while surrounding county of Comal had 188 fatalities per 100,000 people. Harris county had 9.5 fatalities per 100,000 and the surrounding counties of Brazoria Chambers had 55 and 40 fatalities per 100,000 respectively. Figure 12 shows that per capita fatality rates are highest in sparsely populated counties in the southwestern portion of Flash Flood Alley and the Texas Panhandle in the northwestern part of the state.

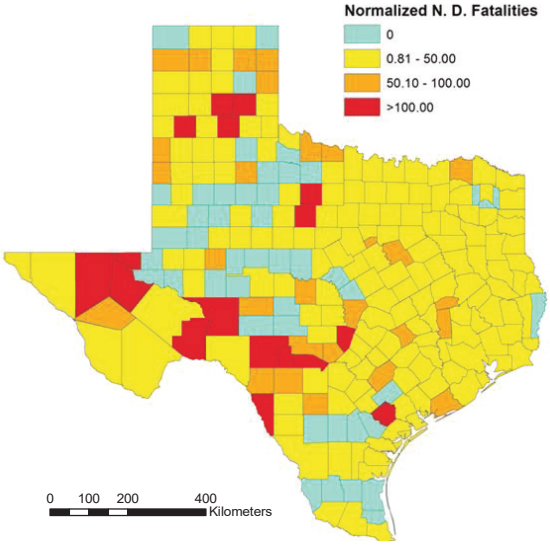


**Figure 12.** Fatalities Normalized by Population (per 100,000).

*4.2. Activity Locations for Fatality Occurrences*

Twenty-five percent (25%) of the reported fatalities did not include a specific activity location of occurrence. But even with this uncertainty the available data strongly suggests that transportation routes are a leading fatality location. Approximately 38% of the total number of hydrometeorological disaster fatalities that reported a location (1756) identified transportation route as the activity location in which the fatality occurred. Approximately two-thirds (65%) of the fatalities on transportation routes were due to flooding which implies that driving into flood conditions is a frequent high-risk activity that likely contributed to many of these deaths. This conjecture is similar to conclusions drawn from research conducted in a study of natural hazard fatalities in Switzerland for the period 1946–2015 [36]. Additionally, research conducted at the University of Texas found that 73% of all flood fatalities in Texas during the period 1959 to 2008 were vehicle related and 16.5% were due to people walking into floodwaters from [13]. Further analysis of hydrometeorological fatalities in the U.S. suggests that flood fatalities are likely underestimated. Sixty-five percent (65%) of fatalities with an unknown location were due to floods, suggesting probable vehicle related incidents with no specific transportation route established.

The number of fatalities on transportation routes are directly related to the number of people on transportation routes which is related to the economic development of the affected region and the demographics of the people professionally and personally committed to the transportation routes. Developed economies result in more transportation between place of employment, schools, commercial and recreational destinations. This skew may be offset since regions of greater wealth and communication networks are more likely (have the ability) to evacuate out of harm which reduces the fatality rate when compared to regions of lower wealth and economic development who are unable or unwilling to evacuate. The employment rate, family structure (dual income/single income), cultural norms, and habits and behavior of the affected population significantly impacts the location of individuals at any given time and thereby impacts the number of fatalities experienced by hydrometeorological disaster events.

*4.3. Gender and Age*

Although gender and age were not reported for a large number of disaster fatality victims, the available information indicates more male fatalities than female fatalities. The gender gap in the hydrometeorological fatality rate exhibited a decreasing trend from the early years of the study to the more recent years suggesting a change in exposure possibly due to shifting roles and responsibilities of men and women in society.

Gender and age are two key demographics that differentiate in lifestyle, behavior and risk tolerance that ultimately affect the fatality rate. Female fatalities due to natural disasters increased significantly from the first to the second half of the study period. The 10-year rolling average more than quadrupled from three deaths in 1969 to 13 deaths in 2016. For the male population, the 10-year rolling average only increased (180%) from 10 deaths to 28 deaths during this same period. If it is generally accepted that contemporary (2017) societal gender roles and responsibilities are not the same as they were in 1959, some reasons for this difference may be in changing situational exposure of the workforce coupled with the level of risk accepted by males versus females. A change in situational exposure is evident in the recent years which is experiencing more role reversal in traditional male/female work roles (e.g., outdoor labor/indoor service).

The impact of gender and risk tolerance is most obvious in the rip current fatality numbers albeit culled from a limited time period (1997–2016) with a 30:1 ratio of male to female fatalities. Deaths from rip currents are more likely a factor of the difference in male / female risk tolerance than in a change of societal roles with more males swimming and pursuing water sports in an area and time of rip current activity. Tornado fatalities are an outlier to the general trends exhibiting a higher female to male fatality ratio, but more data is needed since a potential skew may exist with only 50% of all tornado fatalities reporting gender.

Risk tolerance also changes with age. Within the fatalities that included age (54% of total fatalities), two high risk groups stand out with the largest number of fatalities; 20–29 years. young adult age group and the 70–79 years age group. Changes in priori-ties, family, education, and responsibilities occur for most in this 50-year span and the accepted risk taking from youthful invincibility (such is likely the case for this age group that frequently drive into flash flood conditions), typically progresses to a longer period of more stable (less risky) lifestyle, until the later years when human vulnerabilities of age-related health limitations and immobility issues results in an increase potential for succumbing to hydrometeorological disasters. The limited number of fatality reports that includes age information in this study increases the uncertainty within the trend analysis and is an area that warrants further research. But within the confines of the given data, the elderly appear to be most susceptible to hydrometeorological disaster fatalities based on the percentage of total fatalities and taking into account the relatively low overall percentage of the Texas elderly population. The Texas Demographic Center statistics indicate that Texas population is 27.3% (<18 years, child), 62.4% (18–64 years, adult), and 10.3% ($\geq$65 years, elderly) [37]. The age of the national and state populations overall is increasing and therefore the 2010 census estimates are conservative when comparing the fatality rates among the age groups from this study taking into account the much smaller number of elderly population versus younger age groups.

This study identified that the top two locations for elderly fatalities due to hydrometeorological disaster occurred in permanent residences (45%) and transportation routes (24%) which suggests a high risk to the homebound elderly segment of the population and to elderly when evacuating a disaster. Heat events and flooding were the top two disasters killing the elderly accounting for almost 80% of all elderly fatalities. The number of heat related fatalities is on the rise across all age groups but is particularly evident in the southwest of the U.S. and is usually combined with an extended drought period. Increasing global temperatures may be a factor in this trend with 2016 having the highest average temperature on record as well as the highest monthly temperatures in eight of the 12 months (January–May and July–September) [38]. With heat-related deaths heavily weighted towards the elderly that sometimes do not have family or social networks to acknowledge and report their demise, the fatality rate in this age group may be under-reported

The elderly are not only at risk of heat-related fatalities, but are also very vulnerable to flooding triggered by heavy rains and/or high winds such as exist in hurricane or tropical storm conditions. The fatality rate due to flooding ranked second for the elderly in the study but 45% of all flooding fatalities not reporting age of the victim, there is some uncertainty in this statistic. More certain is that flooding devastates a community on many levels including power interruptions and blockage of transportation routes. Medical attention is a necessity for many elderly, whether it is within a medical facility, nursing home or the need to obtain prescription drugs. All these are typically inhibited during a flooding condition. Although there is debate on whether it is safer to evacuate or shelter the elderly in place during a flood, improvement strategies to reduce fatalities should not be stalled until final consensus.

The study also found that flooding was responsible for 53% of the total hydrometeorological disaster fatalities where the victims were known to be children (<18 years). Young children tend to outnumber adults in a family unit and are dependent on the care and good decisions of parents or guardians. If the family guardian makes a decision (e.g., driving into dangerous flood waters) that result in a fatal outcome it is likely that the number of children will be greater than adult fatalities for the same incident. Data from this study indicates the top activity location for child flood fatalities is on transportation routes (38%) and seems to support the conjecture.

### *4.4. Evacuation or Shelter in Place*

In response to a pending flood or hurricane event, unless there is a mandatory evacuation order given by the city or county jurisdiction, the critical questions to consider is whether it is safer to evacuate by driving or walking to the evacuation location or if there is less risk of harm to shelter

in place. For example, although flood fatalities are most likely to occur on transportation routes, all 68 fatalities (except one) during Hurricane Harvey occurred inside homes. Several factors should be considered when deciding to evacuate or shelter in place such as the perceived risk to the specific area of residence, number of children and elderly in the family, health condition and mobility of each family member, condition of the shelter residence, condition and availability of transportation, and evacuation destination distance. The decision to evacuate during a hurricane or flood can be the difference between life and death.

This decision becomes especially critical with regards to the elderly residing in nursing homes and long-term care facilities (LTCF). Research conducted in 2017 by Pierce on disaster preparedness of LTCF [39] found deficiencies in integrated and coordinated disaster planning, staff training, practical consideration before governments order mandatory evacuations, and accurate assessment of the increased medical needs of LTCF residents following a disaster. Previous research on the management of nursing home residents [40] found that, "the decision to completely evacuate, partially evacuate (including transfers of individual residents), or to shelter in place must be based on the integration of real-time data regarding the disaster event, the facility in question, and the clinical profiles of the residents at risk". Similar research by Dosa et al. [41] specific to Hurricane Katrina and Rita based on a survey of LCTF administrative directors noted a much higher mortality rate with evacuation actions than with shelter in place that was attributed to lack of governmental assistance, unsupported technical and physical requirements for transportation, and difficulty in retaining adequate staff.

*4.5. Temporal Distribution*

The fatality rate of annual raw fatalities increased from 1959 to 2016 with a maximum of 118 fatalities in 1998 due primarily to heat events in the months of July and August and flooding in August and October. Stratification of total fatalities by season indicated that the majority (70%) of all fatalities occurred in spring and summer with floods as the predominant disaster in spring and heat-related deaths in Summer. Monthly variation indicates the highest risk for flooding and tornado fatalities in April and May and the highest risk of heat events in August and September. Within the 68% of the hydrometeorological disaster fatalities that reported the time of day, the data in this study suggests that the afternoon period has the highest risk of fatality from tornado, flooding, or lightning.

Based on the current level of understanding in the relationship between earth sciences and meteorological conditions there is limited scientific predictability of disaster impacts. Predicting hydrometeorological disasters is challenging not only from a scientific basis but also because the fatality rate is not solely a factor of the type of the disaster but is impacted by societal activities of the region in which the disaster event may occur. In general, hurricanes have some level of temporal probability and typically make landfall at night when the storm strengthens due to the latent heat release in the upper and middle atmosphere. Tornadoes also tend to occur in the late afternoon and early evening hours, when the atmospheric conditions are most ripe for supercell thunderstorms and are most common from 4 p.m. to 9 p.m. in the evening [42]. Disaster events such as flooding are dependent on the amount and rate of precipitation and location of adjacent bodies of water (coastal, riverine, or inland). The resulting impact of such a disaster is a function of the activities occurring in the community affected at the time of the flood such as transportation density. Other factors include the level of early warning and evacuation, the time of the day of the flooding to accommodate or hinder rescue and transport efforts.

Similarly, if tornadoes strike during the day (especially a weekday) more people are at work or school and are in buildings where there are adequate public shelter facilities that are typically more disaster resilient than a private residence. Although one quarter of tornado deaths did not include an activity location, within the known study data, only 12% of the fatalities occurred in public/permanent buildings to support this conjecture. The study data also identified that more than 80% of lightning fatalities occur outside, in or around water, and temporary shelters. The extent of fatalities due to lightning is an example of the combined effect of the disaster and the victims location.

Lightning fatalities have decreased significantly on a national and state level in the last several decades as a result of a decrease in exposure (outdoor labor, agricultural work) and the strengthening of OSHA (Occupation-al Safety and Health Agency) safety protocols. Children and adults are the high-risk age groups for lightning fatalities and mitigation efforts to reduce the fatality rate can include increased public awareness in school and at the workplace to move or stay indoors during lightning events. This is especially critical for early morning lightning storms which have the greatest killing potential due to the electric charge build-up overnight [43].

**5. Conclusions and Recommendations**

This study reviewed the fatality rates due to hydrometeorological disasters in Texas over a 58-year study period (1959–2016) with the objective of providing perspectives and information to enhance public awareness, support investment in infrastructure improvement, and serve as input to state and regional disaster mitigation plans. The ability to reduce the number of hydrometeorological fatalities in Texas should not be underestimated. Resources are available but require political will to drive prioritized allocation to ensure weighted coverage in the highest risk areas. Information gleaned from the review of trends from historic hydro-meteorological disasters analyzed in this study can assist decision-makers in determining the best allocation of resources to provide maximum mitigation potential for high risk disasters and regions.

Based on the *Storm Data* analyzed in this study the normalized fatality rates are decreasing for all hydrometeorological disasters except for heat fatalities. The overall growth in population and urban centers plays a key role in the decreasing normalized fatality rates. But population growth appears to have an increasing effect on heat fatalities. The study results show that heat fatalities have a strong correlation to counties with high population density as well as disproportionately effecting the elderly segment of the population. Dedicated financial support can improve emergency preparedness for the elderly in nursing homes, long-term care facilities and private residences to ensure backup power, channels of communication, and available transportation to address immobility issues for the elderly in the case of mandatory evacuation or the necessity to shelter in place.

In addition to the elderly being susceptible to heat fatalities, they are also vulnerable to flooding. The main reasons appear to be related to mobility issues and interruption in medical care. Senior residences and long-term care facilities must have the ability to safely evacuate all their residents if required or be able to shelter in place with all necessary medical staff, medication and back-up power for prolonged medical assistance. Adequate early warning and funding to build a preparedness plan and inventory are vital components to this cause. Requirements for emergency staffing and assistance must be mandated through policy with preparation and training funded before a disaster strikes. Flooding is also the leading killer of adults and children in Texas especially on transportation routes. Adequate road, bridge, and waterway maintenance and improvement to reduce roadway flooding should be an ongoing approved budget item in lieu of recreational upgrades or other low risk projects.

Conversely to populated urban centers that have a higher number of actual fatalities, regions with a low population density exhibit a higher normalized fatality risk. Although the normalized fatality risk is inversely proportional to the population due to the low number of people, the options for survival can still be improved through better preparation. Low population counties are typically rural and do not receive as much funding for road and water management projects. Engineering building codes also maybe more lax contributing to devastation from tornado or other high wind events especially on the coast during hurricane season. Coastal land development must be managed to avoid permanent or non-permanent housing being established in high risk hurricane and storm surge zones. Rural poverty should not be directly related to the risk of death due to a hydrometeorological disaster. The county and state should focus disaster preparation awareness and ensure basic funding is made available to those low population areas with high fatality rates.

Flooding, heat, and tornado events rank as the top three causes of hydrometeorological disaster fatalities in Texas. Regions that are prone to non-coastal flooding are predominantly in the counties within the regions known as Flash Flood Alley and incur a high number of fatalities on transportation routes. Therefore, risk reduction can be supported by investment in roadway flood control improvement including early warning flash flood signage, establishing alternate routes in case of emergencies and mandatory evacuation, preemptive emergency public transportation protocols, and public awareness through educational programs. Tornadoes occur most often in the northeastern counties of Texas, particularly in the months of April and May, and predominantly affect those in temporary or non-permanent shelter (e.g., mobile homes). Contingency planning for the segment of society that is vulnerable to tornadoes can include more frequent public awareness and information campaigns during these months along with practice drills for what to do and where to go when a tornado touchdown is likely. Ensuring that emergency shelters in proximity to mobile home communities are available, accessible, and publicized during these high-risk months also has the potential to save lives. Similar basic considerations can also reduce the risk of fatalities for cold weather, wind events and other types of natural hazards. It is imperative that research builds on historic data to better understand the synergy between high risk disasters, regions and vulnerable segments of society to reduce the risk of hydrometeorological disaster fatalities in Texas.

**Author Contributions:** A.M.C. provided manual aggregation of fatality data contained in archived pdf files and electronic files from the NOAA *Storm Data* repository from 1959 to 2016. H.O.S. provided interim review, comments, and professional guidance in all aspects of writing this paper. S.H.P. performed the quantitative data analysis, qualitative interpretation of results and discussion, and wrote this paper

**Acknowledgments:** We are grateful to the University of Texas at San Antonio for faculty and technical support and the Nuclear Regulatory Commission for financial support of this research.

## References

1. Munich Re. NatCatSERVICE, Natural Catastrophe Know-how for Risk Management and Research. Natural Catastrophe Online Tool. Available online: http://natcatservice.munichre.com/ (accessed on 17 May 2018).
2. Hahn, D.; Viaud, E.; Corotis, R. Multihazard Mapping of the United States. *ASCE-ASME J. Risk Uncertain. Eng. Syst. A Civ. Eng.* **2016**, *3*, 04016016. [CrossRef]
3. Borden, K.; Cutter, S. Spatial patterns of natural disasters mortality in the United States. *Int. J. Health Geogr.* **2008**, *7*, 1–13. [CrossRef] [PubMed]
4. Chowdhury, A.; Mushtaque, R.; Bhuyia, A.; Choudhury, A.; Sen, R. The Bangladesh cyclone of 1991: Why so many people died. *Disasters* **1993**, *17*, 291–304. [CrossRef] [PubMed]
5. Gerritsen, H. What happened in 1953? The Big Flood in the Netherlands in retrospect. *Philos. Trans. R. Soc.* **2005**, *A363*, 1271–1291. [CrossRef] [PubMed]
6. Jonkman, S.; Maaskant, B.; Boyd, E.; Levitan, M. Loss of life caused by the flooding of New Orleans after hurricane Katrina: Analysis of the relationship between flood characteristics and mortality. *Risk Anal. Int. J.* **2009**, *29*, 676–698. [CrossRef] [PubMed]
7. Kure, S.; Jibiki, Y.; Quimpo, M.; Manalo, U.; Ono, Y.; Mano, A. Evaluation of the Characteristics of Human Loss and Building Damage and Reasons for the Magnification of Damage Due to Typhoon Haiyan, Coastal. *Eng. J.* **2016**, *58*, 1640008. [CrossRef]
8. Ashley, S.; Ashley, W. Flood fatalities in the United States. *J. Appl. Meteorol. Climatol.* **2008**, *47*, 805–818. [CrossRef]
9. Singh, O.; Kumar, M. Flood events, fatalities and damages in India from 1978 to 2006. *Nat. Disasters* **2013**, *69*, 1815–1834. [CrossRef]
10. Paulikas, M.; Rahman, M. A temporal assessment of flooding fatalities in Pakistan (1950–2012). *J. Flood Risk Manag.* **2015**, *8*, 62–70. [CrossRef]

11. FitzGerald, G.; Du, W.; Jamal, A.; Clark, M.; Hou, X. Flood fatalities in contemporary Australia (1997–2008). *Emerg. Med. Australas.* **2010**, *22*, 180–186. [CrossRef] [PubMed]
12. Sharif, H.; Jackson, T.; Hossain, M.; Zane, D. Analysis of Flood Fatalities in Texas. *Nat. Disasters Rev.* **2014**, *16*, 04014016. [CrossRef]
13. Sharif, H.; Jackson, T.; Hossain, M.; Bin-Shafique, S.; Zane, D. Motor Vehicle-related Flood Fatalities in Texas, 1959–2008. *J. Trans. Saf. Secur.* **2010**, *2*, 325–335. [CrossRef]
14. Fox News. Fox Facts: Hurricane Katrina Damage. 2006. Available online: http://www.foxnews.com/story/2006/08/29/fox-facts-hurricane-katrina-damage.html (accessed on 2 April 2018).
15. Wikipedia: Hurricane Harvey. Available online: https://en.wikipedia.org/wiki/Hurricane_Harvey (accessed on 2 April 2018).
16. Spatial Disaster Events and Losses Database for the United States (SHELDUS); Hazards and Vulnerability Research Institute. U.S. Hazard Losses (1960–2015) Summary Report. 2017. Available online: http://hvri.geog.sc.edu/SHELDUS/index.cfm?page=reports (accessed on 2 April 2018).
17. National Oceanic and Atmospheric Administration. NOAA. U.S. Tornado Climatology. 2017. Available online: https://www.ncdc.noaa.gov/climate-information/extreme-events/us-tornado-climatology (accessed on 2 April 2018).
18. Ashley, W.S. Spatial and temporal analysis of tornado fatalities in the United States: 1880–2005. *Weather Forecast.* **2007**, *22*, 1214–1228. [CrossRef]
19. Changnon, A.; Pielke, R.; Changnon, D.; Sylves, R.; Pulwarty, R. Human factors explain the increased losses from weather and climate extremes. *Bull. Am. Meteorol. Soc.* **2000**, *81*, 437–442. [CrossRef]
20. Cutter, S.L.; Finch, C. Temporal and spatial changes in social vulnerability to natural disasters. *Proc. Natl. Acad. Sci. USA* **2008**, *105*, 2301–2306. [CrossRef] [PubMed]
21. Cutter, S.; Emrich, C.; Gall, M.; Reeves, R. Flash Flood Risk and the Paradox of Urban Development. *Nat. Disasters Rev.* **2017**, *19*, 05017005. [CrossRef]
22. Milch, K.; Broad, K.; Orlove, B.; Meyer, R. Decision Science Perspectives on Hurricane Vulnerability: Evidence from the 2010–2012 Atlantic Hurricane Seasons. *Atmosphere* **2018**, *9*, 32. [CrossRef]
23. Sault, S. Why the Hill Country Is A.K.A. 'Flash Flood Alley' **2016**. Texas Hill Country. Available online: http://texashillcountry.com/why-the-hill-country-is-a-k-a-flash-flood-alley/ (accessed on 2 April 2018).
24. National Oceanic and Atmospheric Administration (NOAA). National Centers for Environmental Information. Storm Events Database 2017. Available online: https://www.ncdc.noaa.gov/stormevents/ (accessed on 2 April 2018).
25. Border Patrol. Southwest Border Sectors. 2018. Available online: https://www.cbp.gov/sites/default/files/assets/documents/2017-Dec/BP%20Southwest%20Border%20Sector%20Deaths%20FY1998%20-%20FY2017.pdf (accessed on 2 April 2018).
26. Lomonaco, C. U.S. Mexico Border: The Season of Death. *PBS Frontline World*. 2006. Available online: https://www.pbs.org/frontlineworld/blog/2006/06/usmexico_border_1.html (accessed on 2 April 2018).
27. United Nations Education, Scientific, and Cultural Organization (UNESCO), Disaster Risk Reduction. Available online: http://www.unesco.org/new/en/natural-sciences/special-themes/disaster-risk-reduction/natural-hazards/hydro-meteorological-hazards/ (accessed on 2 April 2018).
28. National Weather Service (NWS). Storm Events Database. Directives Systems. 2018. Available online: http://www.nws.noaa.gov/directives/010/010.php (accessed on 2 April 2018).
29. Pitts, Swanya H., Texas State Historical Association (TSHA). Sanderson, Tx. Available online: https://tshaonline.org/handbook/online/articles/hjs07 (accessed on 2 April 2018).
30. Coates, L. Flood Fatalities in Australia, 1788–1996. *Aust. Geogr.* **1999**, *30*, 391–408. [CrossRef]
31. Sharif, H.; Hossain, M.; Jackson, T.; Bin-Shafique, S. Person-Place-Time Analysis of Vehicle Fatalities Caused by Flash Floods in Texas. *Geomat. Nat. Disasters Risk* **2012**, *3*, 311–323. [CrossRef]
32. Singh, O.; Singh, J. Lightning fatalities over India: 1979–2011. *Meteorol. Appl.* **2015**, *22*, 770–778. [CrossRef]
33. Navarrete-Aldana, N.; Cooper, M.A.; Holle, R.L. Lightning fatalities in Colombia from 2000 to 2009. *Nat. Disasters* **2014**, *74*, 1349–1362. [CrossRef]
34. Elsom, D. Deaths and injuries caused by Lightning in the United Kingdom: Analyses of two databases. *Atmos. Res.* **2001**, *56*, 325–334. [CrossRef]

35. Curran, E.; Holle, R.; Lopez, R. Lightning Casualties and Damage in the United States from 1959 to 1994. *J. Clim.* **2001**, *13*, 3448–3464. [CrossRef]
36. Badoux, A.; Andres, N.; Techel, F.; Hegg, C. Natural Disaster Fatalities in Switzerland from 1946 to 2015. *Nat. Disasters Earth Syst. Sci.* **2016**, *16*, 2747–2768. [CrossRef]
37. Texas Demographic Center. Projections of the Population of Texas and Counties in Texas by Age, Sex and Race/Ethnicity for 2010–2050. 2014. Available online: http://txsdc.utsa.edu/Data/TPEPP/Projections/ (accessed on 2 April 2018).
38. Shaftel, H. NASA, Global Climate Change, Vital Signs of the Planet, (2018). Climate Change: How Do We Know? Available online: https://climate.nasa.gov/evidence/ (accessed on 2 April 2018).
39. Pierce, J.; Morley, S.; West, T.; Upton, L.; Banks, L. Improving Long-Term Care Facility Disaster Preparedness and Response: A Literature Review. *Disaster Med. Public Health Preparedness* **2017**, *11*, 140–149. [CrossRef] [PubMed]
40. Dosa, D.; Hyer, K.; Brown, L.; Artenstein, A.; Polivka-West, L.; Mor, V. The controversy inherent in managing frail nursing home residents during complex hurricane emergencies. *J. Am. Med. Dir. Assoc.* **2008**, *9*, 599–604. [CrossRef] [PubMed]
41. Dosa, D. To Evacuate or Not to Evacuate: Lessons Learned from Louisiana Nursing Home Administrators Following Hurricanes Katrina and Rita. *J. Am. Med. Dir. Assoc.* **2007**, *8*, 142–149. [CrossRef] [PubMed]
42. Weather Underground. Prepare for a Tornado. Available online: https://www.wunderground.com/prepare/tornado (accessed on 16 April 2018).
43. Woollaston, V. Lightning is at its most powerful at 8am in the morning but more storms occur in the afternoon, Daily Mail 2015. Available online: http://www.dailymail.co.uk/sciencetech/article-2998781/Lightning-powerful-8am-morning-storms-occur-afternoon.html (accessed on 16 April 2018).

# 5

# Examples of Application of $^{GA}$*SAKe* for Predicting the Occurrence of Rainfall-Induced Landslides in Southern Italy

**Oreste Terranova [1], Stefano Luigi Gariano [2,*], Pasquale Iaquinta [1], Valeria Lupiano [1], Valeria Rago [1] and Giulio Iovine [1]**

[1] Istituto di Ricerca per la Protezione Idrogeologica (IRPI), Consiglio Nazionale delle Ricerche (CNR), via Cavour 6, 87036 Rende (CS), Italy; oreste.terranova@irpi.cnr.it (O.T.); pasquale.iaquinta@irpi.cnr.it (P.I.); valeria.lupiano@irpi.cnr.it (V.L.); valeria.rago@irpi.cnr.it (V.R.); giulio.iovine@irpi.cnr.it (G.I.)

[2] Istituto di Ricerca per la Protezione Idrogeologica (IRPI), Consiglio Nazionale delle Ricerche (CNR), via Madonna Alta 126, 06128 Perugia, Italy

* Correspondence: gariano@irpi.cnr.it

**Abstract:** $^{GA}$*SAKe* is an empirical-hydrological model aimed at forecasting the time of occurrence of landslides. Activations can be predicted of either single landslides or sets of slope movements of the same type in a homogeneous environment. The model requires a rainfall series and a set of dates of landslide activation as input data. Calibration is performed through genetic algorithms, and allows for determining a family of optimal kernels to weight antecedent rainfall properly. As output, the mobility function highlights critical conditions of slope stability. Based on suitable calibration and validation samples of activation dates, the model represents a useful tool to be integrated in early-warning systems for geo-hydrological risk mitigation purposes. In the present paper, examples of application to three rock slides in Calabria and to cases of soil slips in Campania are discussed. Calibration and validation are discussed, based on independent datasets. Obtained results are either excellent for two of the Calabrian rock slides or just promising for the remaining case studies. The best performances of the model take advantage of an accurate knowledge of the activation history of the landslides, and a proper hydrological characterization of the sites. For such cases, $^{GA}$*SAKe* could be usefully employed within early-warning systems for geo-hydrological risk mitigation and Civil Protection purposes. Finally, a new release of the model is presently under test: its innovative features are briefly presented.

**Keywords:** landslide forecasting; threshold; hydrological model; genetic algorithms; Calabria; Campania

## 1. Introduction

Rainfall-induced landslides often cause significant economic loss and casualties in Calabria, as in most part of the Italian Peninsula [1,2]. Therefore, their prediction assumes a crucial role in geo-hydrological risk mitigation. The timing of activation of such phenomena is usually predicted by means of either empirical (e.g., [3] and references therein) or physically-based [4–6] approaches. To relate rainfall to time of slope instability, the extent of the landslide and the physical characteristics of both rainfall and involved materials (soil/rock) must be considered—e.g., in terms of intensity, duration, amount, and of infiltration capacity. Unfortunately, because of the high cost of field investigations, the parameters required by the physically-based approach are known only for a very limited number of case studies. Therefore, to model the triggering conditions of slope movements—either shallow or deep-seated—a threshold-based modelling approach can be employed [7,8]. Empirical thresholds can be expressed in terms of curves, delimiting the portion

of Cartesian planes containing rainfall or hydrological conditions related to known activations. Examples of definition and application of empirical rainfall thresholds in Southern Italy are provided by [9–13]. In hydrological models, kernels (or filter functions) are commonly employed to express the influence of rainfall on runoff and groundwater dynamics: they are usually defined in terms of a simple, continuous analytical function. The base time ($t_b$) of a given kernel expresses the temporal extent in which rainfall seems to have a significant effect on slope stability. The shape and the base time of the kernel are related to magnitude of the landslide and to hydro-geological complexity of the site under investigation. Finally, the predictive tool (named mobility function) can be obtained through the convolution integral between the kernel and the rainfall series [14–16].

**2. Materials and Methods**

$^{GA}$*SAKe* (Genetic-Algorithm-based Self Adaptive Kernel) is an empirical-hydrological model for predicting the timing of activation of slope movements of different types [17]. A linear and steady slope-stability response to rainfall and a classic threshold scheme are assumed in the model: the exceedance of the threshold determines the triggering of the landslide [18]. Though inspired by the *FLaIR* (Forecasting Landslides Induced by Rainfall) model [19,20] (already applied in several case studies, see [21–23]), it differs for several features and is suitable to handle complex cases: in fact, the model adopts a discrete kernel, instead of a continuous one, and is based on a genetic-algorithm procedure that allows for an effective, automated, self-adaptive calibration. The model can be applied either to single landslides, characterized by several historical activations, or to a set of similar slope movements in a homogeneous geomorphological context. Case studies may be of any depth, from shallow to deep-seated. The inputs of the model are: (i) the rainfall series and (ii) the set of known dates of landslide activation. Regarding rainfall data, $^{GA}$*SAKe* needs as input a single rainfall series at a given time scale (e.g., daily, hourly, sub-hourly rainfall); the series can be derived from one only rain gauge or by combining rainfall data from different gauges into a "synthetic" series (e.g., by means of geostatistical techniques). The temporal extent of the rainfall series must start before the first landslide activation date and terminate after the last date (e.g., at the beginning and at the end of hydrological years). The mobility function—i.e., the output of the model as obtained through calibration—highlights the most critical conditions for the stability of the considered case study: its values depend on both rainfall amounts and shape/base time of the kernel. Triggering conditions occur when the value of the mobility function exceeds a given threshold.

More in detail, calibration of the model is based on genetic algorithms ("GA", in the following;[24,25]), which allow to obtain families of optimal, discretized solutions (kernels) that maximize the fitness function. At the beginning of a given optimization experiment, a family of kernels is randomly generated. The application to such kernels of a sequence of genetic operators—namely *selection*, *crossover* and *mutation*—constrained by prefixed probabilities, allows to generate a new population of candidate solutions (genotypes), to be tested as kernels in the successive GA iteration. A mobility function (phenotype) is then obtained by convolution between each kernel and rainfall, and its performance is evaluated by applying a suitable fitness function. Thanks to inherent proprieties of GA (cf., Fundamental Theorem [24]), better individuals (i.e., characterized by higher fitness values) can be obtained over time through iterations.

In $^{GA}$*SAKe* the evaluation of the phenotypes (and, therefore, of the related genotypes) is primarily based on the *fitness values*, $\Phi$, defined on the relative position (*rank*, $k_i$) of the peaks of the mobility function corresponding to the L dates of landslide activation [17]. It is:

$$\Phi = \frac{\sum_{i=1}^{L} k_i^{-1}}{\sum_{i=1}^{L} i^{-1}}. \quad (1)$$

When two (or more) mobility functions share the same value of fitness, a further distinction can be made based on the safety margin, $\Delta z_{cr}$, defined as:

$$\Delta z_{cr} = \left(z_{j-\min} - z_{cr}\right) / z_{j-\min}, \tag{2}$$

in which $z_{j\text{-}min}$ is the height of the lowest peak of the mobility function that corresponds to one of the activation dates, and $z_{cr}$ is the critical height, i.e., the height of the highest peak of the mobility function located just below $z_{j\text{-}min}$. Kernels with similar $\Phi$ can therefore be distinguished, and those more useful for predictive purposes selected, being characterized by larger separations among the peaks of the mobility function either corresponding to dates of activation or not.

Over several GA iterations, the mobility function is forced toward a shape characterized by peaks coinciding with the dates of landslide occurrence. An optimal kernel leads to a mobility function having the highest peaks in correspondence to such dates; further peaks may also be present, but characterized by lower values.

The best Q kernels obtained in the calibration phase can be utilized to synthetize "average" kernels to be employed for validation, by considering further dates of landslide activation (and appropriate rainfall series). Up to date, a set of Q = 100 optimal kernels has been employed during tests and first applications of the model to several case studies in Southern Italy. Once validated, the model can finally be applied—e.g., in support of an early-warning system—to estimate the timing of future landslide activations in the same study area, by employing measured or forecasted rainfall. In Figure 1, the calibration and validation procedures are schematically shown. For the sake of brevity, a complete description of the model is not reported here; however, a more detailed overview of its main features and of the calibration/validation procedures can be found in [3].

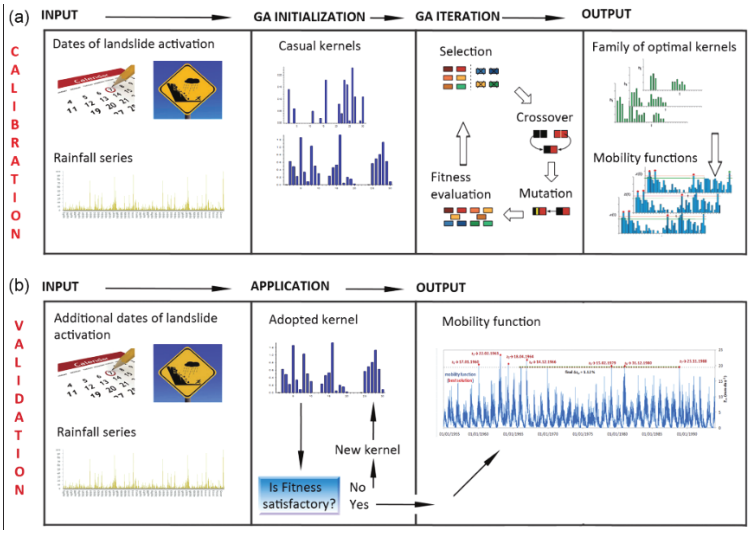


**Figure 1.** Schematic sketch of: (**a**) the calibration and (**b**) the validation procedures of $^{GA}SAKe$.

## 3. Case Studies

The model was applied to different case studies in Southern Italy (Figure 2), and precisely to 3 rock slides in northern Calabria and to a set of shallow landslides (soil slip-debris flows) in Campania. Table 1 lists the average rainfall recorded near the considered case studies, while Tables 2 and 3 list the main characteristics of the considered slope movements.

**Table 1.** Average monthly and annual rainfall (MR, in mm) and number of rainy days (MRD) at rain gauges near the considered case studies. Key: (AC) Acri rain gauge (750 m a.s.l.); (MU) Montalto Uffugo rain gauge (468 m a.s.l.); (GR) Gragnano rain gauge (185 m a.s.l.).

| Rain Gauge | Variable | September | October | November | December | January | February | March | April | May | June | July | August | Year |
|---|---|---|---|---|---|---|---|---|---|---|---|---|---|---|
| AC | MR | 57.9 | 105.7 | 130.5 | 160.1 | 141.4 | 120.8 | 102.4 | 73.6 | 54.8 | 24.4 | 16.2 | 24.7 | 1012.4 |
| | MRD | 6 | 9 | 10 | 13 | 13 | 11 | 10 | 9 | 6 | 3 | 2 | 3 | 96 |
| MU | MR | 70.4 | 125.1 | 187.9 | 220.8 | 198.1 | 160.3 | 132.8 | 98.9 | 64.6 | 27.8 | 18.3 | 28.6 | 1333.6 |
| | MRD | 7 | 11 | 13 | 14 | 14 | 13 | 13 | 11 | 8 | 5 | 3 | 4 | 114 |
| GR | MR | 90.1 | 144.8 | 202.1 | 209.3 | 181.1 | 152.8 | 119.0 | 106.4 | 62.7 | 31.8 | 23.2 | 36.4 | 1359.7 |
| | MRD | 6 | 9 | 12 | 10 | 11 | 10 | 9 | 9 | 7 | 4 | 3 | 3 | 94 |

**Table 2.** Main characteristics of the Calabrian case studies. In Italics, the dates of activation used for validation. Employed data series range from the beginning of the calibration periods to the end of the validation period (cf. last column). No missing data characterize the considered rain series.

| Landslide (Involved Lithotype) | Landslide Type | Dimensions | Activation Dates | Optimization Periods (Rain Gauge, Distance from Landslides) |
|---|---|---|---|---|
| Acri—Serra di Buda (Palaeozoic metamorphic and intrusive rocks) | rock slide | length: 550 m<br>width: 400 m<br>depth: 45–50 m | (1) 20.11.1937<br>(2) 29.12.1937<br>(3) 12.1944–01.1945<br>(4) 01.12.1980<br>(5) 28.11.1984<br>*(6) 01.04.1985* | calibration period:<br>01.01.1932–31.01.1985<br>validation period:<br>01.02.1985–01.06.1985<br>(Acri, 1.2 km) |
| San Benedetto Ullano—San Rocco (Palaeozoic metamorphic rocks) | rock slide | length: 550 m<br>width: 300 m<br>depth: 15–35 m | (1) 28.01.2009<br>(2) 31.01.2010<br>*(3) 15.03.2013* | calibration period:<br>01.01.1970–30.04.2010<br>validation period:<br>01.05.2010–30.04.2013<br>(Montalto Uffugo, 3.5 km) |
| San Fili—Uncino (Miocene sedimentary rocks overlaying Palaeozoic metamorphic rocks) | rock slide | length: 650 m<br>width: 200 m<br>depth: 25–30 m | (1) 16.01.1960<br>(2)<br>01.11.1962–14.04.1963<br>(3) 15.04.1964<br>(4) 14.12.1966<br>(5) 13.02.1979<br>*(6) 12.1980* | calibration period:<br>01.09.1959–31.08.1980<br>validation period:<br>01.09.1980–31.03.1981<br>(Montalto Uffugo, 8 km) |

**Table 3.** Main characteristics of the considered Campanian case studies. Key: (M) multiple activation; (S) single activation. In Italics, the date of activation used for validation. Employed data series range from the beginning of the calibration periods to the end of the validation period (cf. last column). The Gragnano rain gauge was employed for the Campanian cases. Missing values (about 2% of the whole set) were taken from the Castellammare and Tramonti-Chiunzi gauges.

| Landslide (Involved Lithotype) | Landslide Type | Average Dimensions | Activation Dates (Type)/Affected Site | Optimization Periods (Rain Gauge, Average Distance from Landslides) |
|---|---|---|---|---|
| Sorrento Peninsula (Pleistocene volcanic and volcanoclastic deposits overlaying Mesozoic limestone) | soil slip | source area: 100–20000 $m^2$ source depth: 0.5–4 m | (1) 17.02.1963 (M)/Gragnano, Pimonte, Castellammare.<br>(2) 23.11.1966 (S)/Vico Equense (Scrajo), Arola, Ticciano.<br>(3) 15–24.03.1969 (M)/Cava de' Tirreni, Agerola, Scrajo Seiano.<br>(4) 02.01.1971 (S)/Gragnano.<br>(5) 21.01.1971 (S)/Gragnano.<br>(6) 04.11.1980 (S)/Vico Equense (Scrajo).<br>(7) 14.11.1982 (S)/Pozzano.<br>(8) 22.02.1986 (M)/Palma Campania, Castellammare, Vico Equense.<br>(9) 23.02.1987 (S)/Gragnano, Castellammare.<br>(10) 23.11.1991 (S)/Pozzano.<br>*(11) 10.01.1997 (M)/Pozzano, Castellammare, Nocera, Pagani, Amalfitana Coast.* | calibration: 17.01.1963–10.12.1996 validation: 11.12.1996–10.02.1997 (Gragnano, Castellammare, and Tramonti-Chiunzi, 4.5 km) |

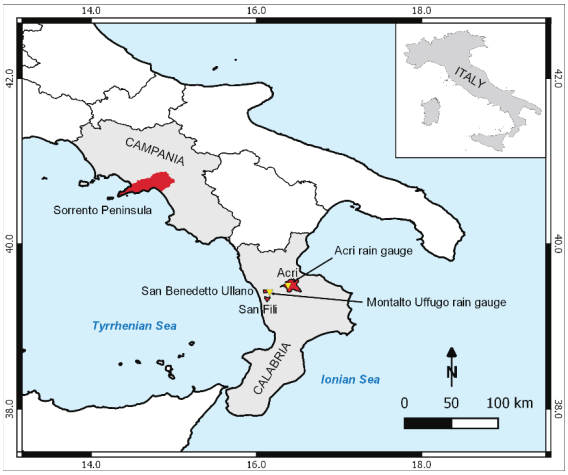


**Figure 2.** Location of the case studies (marked in red) in Calabria and Campania regions (marked in grey). Yellow triangles indicate Acri and Montalto Uffugo rain gauges.

### *3.1. Calabrian Case Studies*

Calabria is an accretionary wedge made of a series of Jurassic to Early Cretaceous ophiolite-bearing tectonic units, plus overlying Hercynian and pre-Hercynian basement nappes [26]. Because of its geodynamic history [27–30], the lithological units that make up the Calabrian Arc are commonly characterized by pervasive fracture systems that favored the development of severe weathering processes. The combined effect of tectonic disturbance, differentiated uplift, erosive processes, and chemical-physical alteration influenced physiographic setting of the region, allowing for widespread slope movements of various types and extensions. In addition to earthquakes, meteoric events represent the main triggering factor of landslides in Calabria [31]. These latter pose serious risk conditions in much of the region [32–39]. The climate is Mediterranean (Csa, according to [40]). The Tyrrhenian sector is rainier than the Ionian one (1200–2000 mm vs. 500 mm); nevertheless, the most severe storms occur more frequently on the Ionian side of the region [41]. According to [42], heavy and frequent winter rainfall, caused by cold fronts mainly approaching from NW, and autumn rains, determined by cold air masses from NE, affect the region. In spring, rains show lower intensities than in autumn, while strong convective storms are common at the end of summer. Average yearly rainfall varies between 1000 and 2000 mm/y in mountainous and internal areas, and between 600 and 900 mm/y in coastal areas, with a mean regional value of about 1150 mm/y. Over 70% of the yearly precipitation occurs from October to March, with negligible monthly values from June to September. Concerning the effects of climate change in Calabria, a reduction of annual and winter amounts and an increase of summer rainfall has been recorded in the past decades (e.g., [43,44]).

#### 3.1.1. The Acri—Serra di Buda Landslide

The village of Acri (Figure 3) is located on the Sila Massif, on the right flank of the Crati Graben, a tectonic depression belonging to the Calabrian-Sicilian Rift Zone [27]. The area is marked by a couple of regional, recent/active systems, made of N–S trending normal faults and of WNW–ESE trending strike-slip faults [45,46]. Along the N–S trending system, Palaeozoic metamorphic and igneous rocks (gneiss and granite, commonly weathered) of the Sila Massif, to the East, give place to Late Miocene-Quaternary sediments (mainly conglomerate, sand and clay) of the graben, to the West [47].

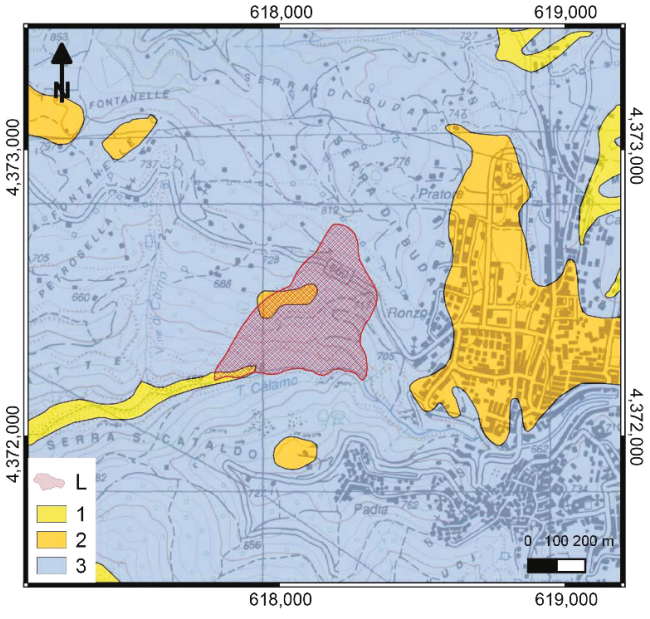


**Figure 3.** Lithological sketch of the Serra di Buda landslide at Acri. Key: (1) Alluvium, colluvium and residual soil; (2) conglomerate and sandstone; (3) Igneous and medium-high grade metamorphic rock. The landslide (L) is marked by a red hatched polygon. Topographic base map after 1:25,000 IGMI sheets; lithological map after [47], Geological map of Calabria (scale 1:25,000), mod.

The translational rock slide of Serra di Buda is a portion of a Sackung [48] that threatens the surroundings of the village of Acri. The landslide involves weathered gneissic and granitic rocks. In the last 100 years, it suffered from several reactivations and the Civil Authorities had to close the state road to traffic on several occasions, thus causing serious connection problems with the main urban centers of the area (mainly located in the nearby valley). In the present study, only a subset of the known dates of activation are considered: based on hydrological analyses, [49] showed either scarce or no direct correlation between some of the historical dates of mobilization and rainfall amounts. For such dates, further analyses are needed to better evaluate the possible causes of activation [50].

### 3.1.2. The San Benedetto Ullano—San Rocco Landslide

The village of San Benedetto Ullano (Figure 4) is located on the left flank of the Crati Graben, at the base of the Coastal Chain. The area is marked by the San Fili-San Marco Argentano normal fault, a N–S trending active structure ca. 30 km long. Along the fault, the metamorphic rocks (mainly gneiss, schist and phyllite) of the Coastal Chain, to the West, give place to Pliocene-Quaternary sediments (conglomerate, sand and clay) and subordinate Miocene outcrops (conglomerate and evaporate rocks), to the East [47]. Note that, at the rain gauge of Montalto Uffugo (in the surroundings of San Benedetto Ullano), the highest Calabrian amounts of mean annual rainfall are recorded.

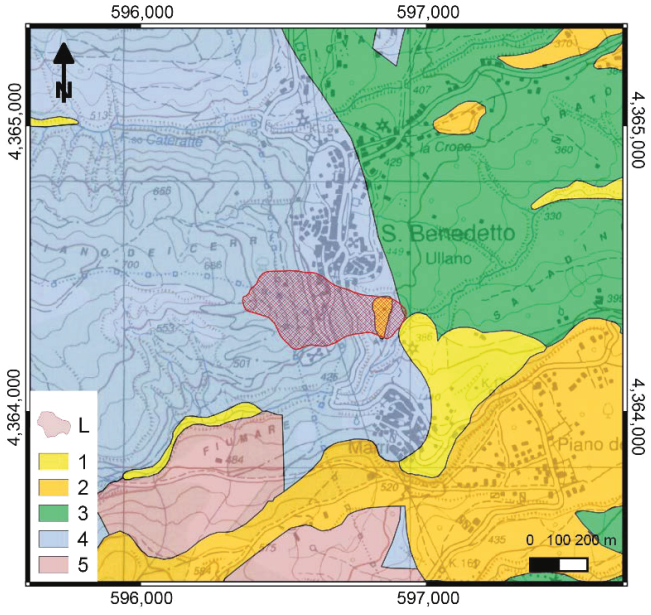


**Figure 4.** Lithological sketch of the San Rocco landslide at San Benedetto Ullano. Key: (1) Alluvium, colluvium, and residual soil; (2) conglomerate and sandstone; (3) Clay and clayey flysch; (4) Igneous and medium-high grade metamorphic rock; (5) Argillite and low-grade metamorphic rock. The landslide (L) is marked by a red hatched polygon. Topographic base map after 1:25,000 IGMI sheets; lithological map after [47], Geological map of Calabria (scale 1:25,000), mod.

The San Rocco translational rock slide developed mainly in gneissic rocks at the southern margin of the village, between the historical center and the cemetery [14,51,52]. Between January 2009 and March 2013, a series of 3 major re-activations was observed, with serious damage to the provincial road; the Cemetery and several buildings at the southern margin of the village were also affected by widespread opening of fissures and fractures.

3.1.3. The San Fili—Uncino Landslide

The village of San Fili (Figure 5) is located on the left flank of the Crati graben. In the area, N–S trending normal faults mark the transition between Palaeozoic weathered metamorphic rocks of the Coastal Chain (migmatitic gneiss and biotitic schist), mantled by a late Miocene sedimentary cover of conglomerate, arenite and marly clay, to the West, and Pliocene–Quaternary sediments (sand and clay) of the graben, to the East [47]. The village lies in the intermediate sector between two faults, cut by a NE–SW trending connection fault delimiting Miocene sediments, to the North, from gneissic rocks, to the South.

The Uncino rock slide developed at the western margin of San Fili, involving Miocene sediments (clay and subordinate sandstone) overlaying Palaeozoic metamorphic rocks (gneiss and biotitic schist). In historical time, the slope movements repeatedly affected the village, damaging the railway and the local road network, as well as some buildings: the most ancient known activation dates to the beginning of the twentieth century [53]; from 1960 to 1990, the regional railroad was frequently damaged or even interrupted [54]. Cumulated antecedent rains corresponding to known activations of the Uncino landslide were analyzed by considering the records of the Montalto Uffugo rain gauge [17].

Based on trends of antecedent rains in the 30–180 days before activations, the activation dates to be used for hydrological analyses could be selected.

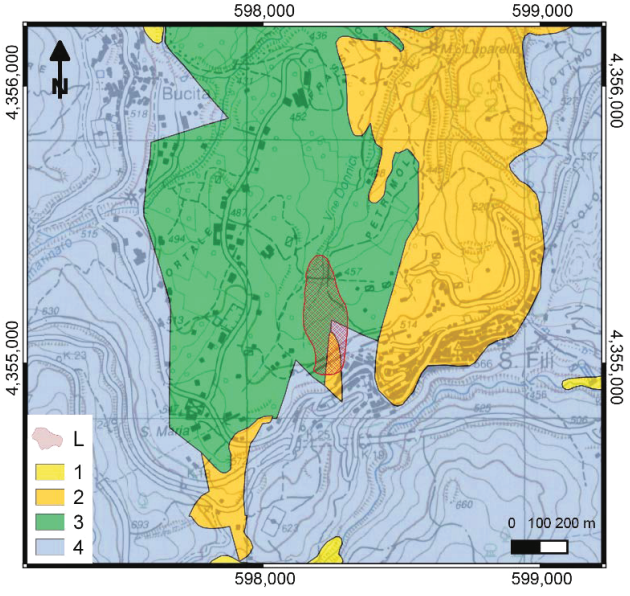


**Figure 5.** Lithological sketch of the Uncino landslide at San Fili. Key: (1) Alluvium, colluvium, and residual soil; (2) conglomerate and sandstone; (3) Clay and clayey flysch; (4) Igneous and medium-high grade metamorphic rock. The landslide (L) is marked by a red hatched polygon. Topographic base map after 1:25,000 IGMI sheets; lithological map after [47], Geological map of Calabria (scale 1:25,000), mod.

*3.2. Campanian Ccase Studies*

The Sorrento Peninsula (Figure 6) is in western Campania, Southern Italy, within the frame of the Neogene Apennine Chain [55]. In the area, Mesozoic limestone mainly crops out, covered by Miocene flysch, Pleistocene volcanic deposits (pyroclastic fall, ignimbrite), and Pleistocene detrital–alluvial deposits [56]. The carbonate bedrock constitutes a monocline, gently dipping towards WNW, mantled by sedimentary and volcanoclastic deposits, with thicknesses ranging from a few decimeters to tens of meters.

Hot, dry summers and moderately cold and rainy winters characterize the study area; its climate is Mediterranean (Csa, according to [40]). Average annual rainfall varies from 900 mm, west of Sorrento, to 1500 mm at Mt. Faito; moving inland to the East, it reaches 1600 mm at Mt. Cerreto and 1700 mm at the Chiunzi pass [57]. On average, annual totals are concentrated on about 95 rainy days. During the driest 6 months (from April to September), only 30% of the annual rainfall is recorded in about 30 rainy days. During the three wettest months (November, October, and December), a similar amount is recorded in about 34 rainy days [58]. In the area, convective rainstorms commonly occur at the beginning of the rainy season (from September to October). In autumn–winter, either high intensity or long duration rainfall are usually recorded, while uniformly distributed rains generally occur in spring. Both at sea level and higher elevations, the southern slopes of the Peninsula are characterized by smaller average annual maxima of daily rainfall with respect to the northern slopes [59]. Severe storms frequently trigger shallow landslides in the volcanoclastic cover of the Peninsula. Landslide sources show a wide range of planforms (i.e., elongated, triangular, grape-like

and compound), extensions (from 100 m up to 20,000 $m^2$), and depths (from 0.5 to 4 m). Soil slips usually propagate seaward as either debris flows or avalanches, often increasing their original volume by entraining material along the tracks, and eventually causing casualties and serious damage to urbanized areas and transportation facilities [60–62].

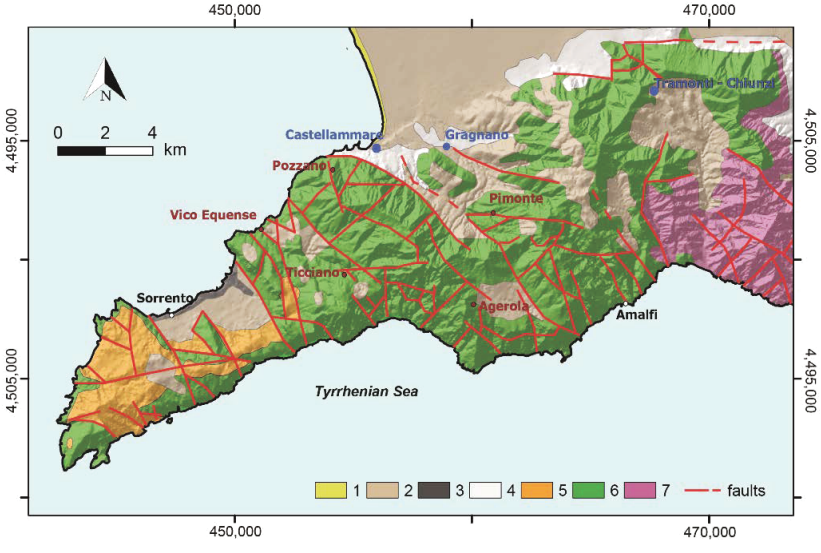


**Figure 6.** Lithological sketch of the Sorrento Peninsula. Key: (1) beach deposit (Holocene); (2) pyroclastic fall deposit (late Pleistocene–Holocene); (3) Campanian ignimbrite (late Pleistocene); (4) detrital alluvial deposit (Pleistocene); (5) flysch deposit (Miocene); (6) limestone (Mesozoic); (7) dolomitic limestone (Mesozoic). Red lines mark the main faults; red circles and red labels, the sites affected by shallow landslide activations; blue circles, the rain gauges; white circles, the main localities (after [17], mod.).

In the second half of the 20th century, shallow landslides activated on several occasions nearby Castellammare di Stabia: in Table 3, the major events recorded between Vico Equense and Gragnano are listed, with details on types of events and affected sites. All such events occurred between November and March, a period characterized by a medium to low suction range and included in the rainy season (October to April), according to [63]. Rainfall responsible for landslide occurrences in the Sorrento Peninsula were extracted from the records of the nearest gauges (i.e., Gragnano, Castellammare, and Tramonti-Chiunzi; Figure 6). The trends of antecedent rains look quite different. Based on hydrological consideration, the dates of activation were selected for calibration and validation of the model.

## 4. Results and Discussion

For each case study, the model was optimized by considering a subset of calibration dates, and then validated against further dates of activation. The calibration and validation periods were defined based on rainfall data availability, seasonality, and quality of information on activation dates (Tables 2 and 3). More in detail, optimal kernels were obtained in calibration by averaging the best 100 filter functions. Validation was then performed by applying such average kernels to the remaining activation dates (i.e., a temporal validation was performed). The optimal kernels and mobility functions for the considered case studies are shown in Figures 7–10. Calibration and validation results are synthetized in Table 4.

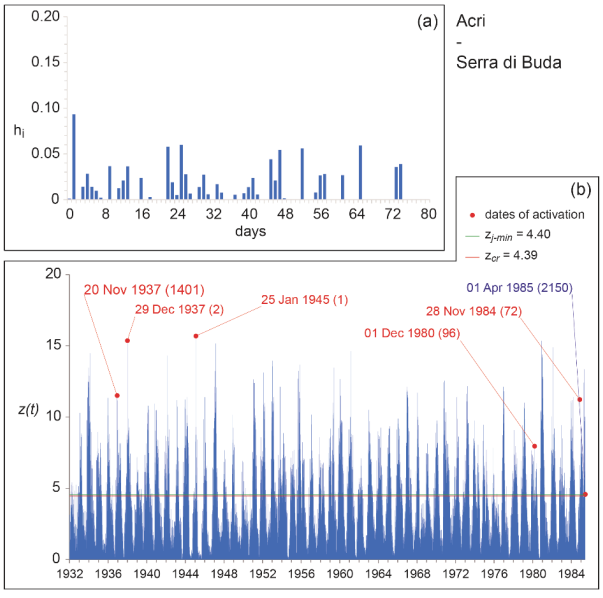


**Figure 7.** Acri—Serra di Buda case study: (**a**) optimal kernel; (**b**) mobility function obtained by applying the optimal kernel to the entire set of available activation dates (cf. [50]).

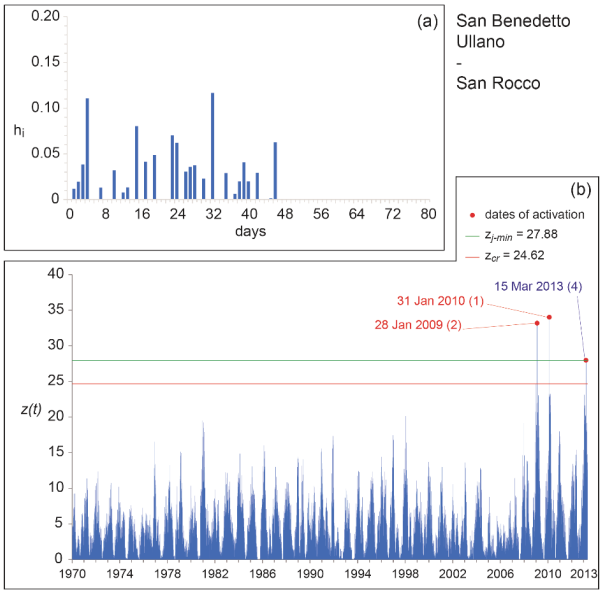


**Figure 8.** San Benedetto Ullano—San Rocco case study: (**a**) optimal kernel; (**b**) mobility function obtained by applying the optimal kernel to the entire set of available activation dates (cf. [54,64]).

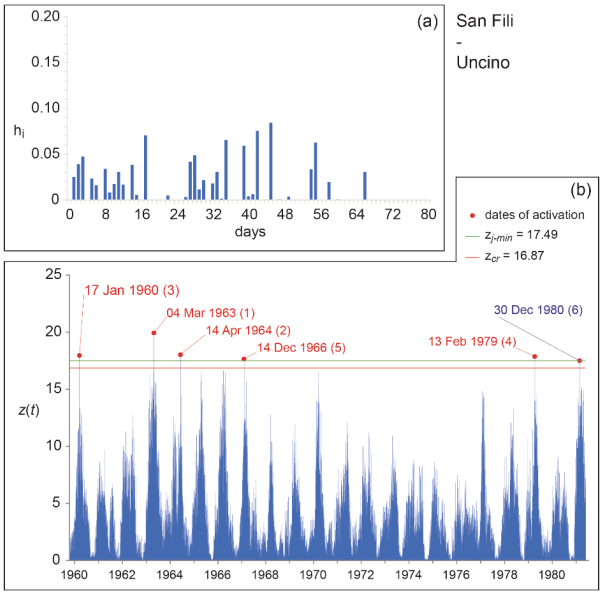


**Figure 9.** San Fili—Uncino case study: (**a**) optimal kernel; (**b**) mobility function obtained by applying the optimal kernel to the entire set of available activation dates (cf. [17]).

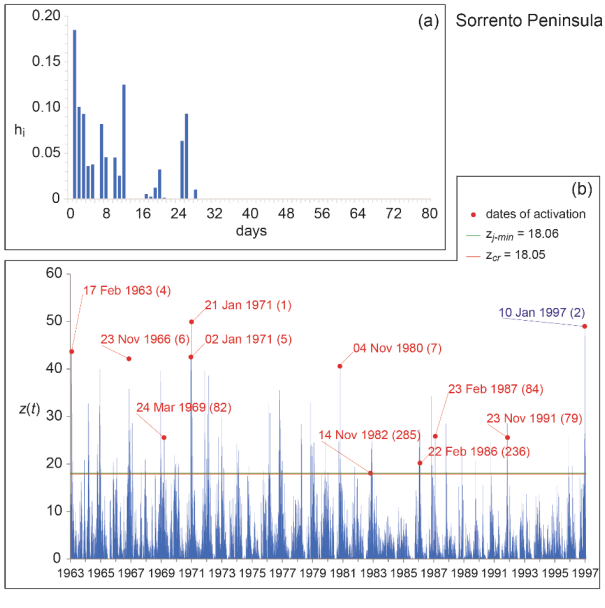


**Figure 10.** Sorrento Peninsula case study: (**a**) optimal kernel; (**b**) mobility function obtained by applying the optimal kernel to the entire set of available activation dates (cf. [17]).

**Table 4.** Model results for the considered case studies. For each case, the following details are listed: landslide type; number of activation dates employed for calibration and validation; base time of the optimal kernel; maximum fitness obtained in calibration and in validation.

| Case Study | Landslide Type | Activation Dates (Calibration + Validation) | $t_b$ (Days) | $\Phi_c$ (Calibration) | $\Phi_v$ (Validation) |
|---|---|---|---|---|---|
| Acri —Serra di Buda | rock slide | 5 + 1 | 74 | 82.8% | 62.2% |
| San Benedetto Ullano—San Rocco | rock slide | 2 + 1 | 46 | 100% | 96.2% |
| San Fili—Uncino | rock slide | 5 + 1 | 66 | 100% | 100% |
| Sorrento Peninsula | soil slip | 10 + 1 | 28 | 80.6% | 76.3% |

The base times of the optimal kernels for the considered case studies are quite consistent with landslide magnitudes, being $t_b$ of the Sorrento Peninsula about a half of the Calabrian cases. Base times also reflect permeability and extent of underground water patterns of the drainage basins feeding the landslide sites. In the case of the shallow landslides of the Sorrento Peninsula, shorter base times and higher influence of most recent rainfall can be observed with respect to the Calabrian rock slides, evidencing a faster slope stability response to rainfall as potential triggering factor.

As for the case studies considered in this paper, calibration and validation results show fitness values ranging from 81% to 100 % and from 62% to 100%, respectively. The best model performances were obtained for the case studies of San Fili—Uncino and San Benedetto Ullano—San Rocco, while less satisfactorily results characterize the Sorrento Peninsula and Acri—Serra di Buda cases. It should be noticed that, for the San Rocco landslide, the fitness obtained in validation is affected by a false alarm predicted by the model just the day before the activation of the phenomenon (as known from local archives).

Generally speaking, case studies characterized by fewer activation dates are simpler to model. On the other hand, model performances are known to be hampered by quality or completeness of input data (e.g., missing dates of activation; dates related to other triggering factors; unsuitability of the rain gauge network) [65]. Furthermore, available rain gauges are usually far from the sites of interest, and located at either different elevations or aspects. Uncertainty in rainfall estimation has a strong impact on the identification of the triggering rainfall [66,67]. Still, information regarding activation dates is commonly incomplete or poorly accurate [10]. As a whole, such uncertainties may strongly affect the calibration and the validation of the models.

In this study, the best results obtained were presumably favored by:

- accurate recording of damaging events along the railway track, for the Uncino rock slide;
- accurate monitoring of landslide activations and damaging events at the margin of the village, for the San Rocco rock slide;
- good representativeness of the rainfall series recorded at the Montalto Uffugo rain gauge, for both the Uncino and the San Rocco rock slides.

As for the weakest results, they may be explained by considering the following issues:

- for the Sorrento Peninsula case study, significant heterogeneities in slope materials and differences in extent of shallow landslides reasonably affected model performances. In addition, dates of landslide activation may be missing, especially for soils slips triggered in remote areas. Rainfall events responsible for shallow landslide activations are usually short and spatially limited (e.g., convective storms), and can barely be recorded by the rain gauge network. Consequently, the representativeness of the rain series cannot be guaranteed for such type of meteoric events.

- for the Acri case study, some of the considered activations may refer to secondary portions of the rock slide. For some dates, historical archives are not, in fact, detailed enough to permit an accurate understanding of the mobilized volumes. Consequently, movements affecting only portions of the rock slide—or even other nearby landslides developed in the same Sackung—may be erroneously attributed to the investigated phenomenon.

**5. Conclusions and Perspectives**

In the present paper, examples of application of $^{GA}SAKe$ have been presented, with reference to soil slips and rock slides in Southern Italy. For all cases, both calibration and validation of the model were performed using independent datasets. Obtained results sound either excellent (cf. San Fili—Uncino and San Benedetto Ullano—San Rocco cases) or just promising (Sorrento Peninsula, and Acri—Serra di Buda cases).

For the Uncino and the San Rocco landslides, the activation dates are correctly predicted by the model, evidently thanks to an accurate knowledge of the activation history of the landslide, and a proper hydrological characterization of the site. For such case, $^{GA}SAKe$ could be applied to predict the timing of activation of future landslide activations in the same areas. Thanks to kernels obtained in calibration, the model could be usefully employed within early-warning systems for geo-hydrological risk mitigation and Civil Protection purposes, also based on predicted rainfall.

Conversely, for the Serra di Buda and the Sorrento Peninsula cases, weaker model performances appear to be influenced by an inaccurate knowledge of the activation dates and/or rainfall series—as generally occurs with hydrological models. Nevertheless, such results still sound encouraging, provided that quality and completeness of data were improved. For past activations, further investigations may allow to better define the history of landslide mobilizations in the considered areas; rainfall data recorded at the surface by the gauge network may profitably be combined with weather radar prospections (cf. e.g., [68,69]). Moreover, it would be desirable that regional geological and hydrographic services were strengthened to guarantee adequate activities of surveying and monitoring of the geo-hydrological events, by implementing and updating suitable data bases on triggered slope movements (including details such as location, type, type of involved materials, dates of activation, damage). As for the rains, the networks may be improved by adding further gauges and/or radar installations.

It is worth observing that, due to its empirical/hydrological nature, $^{GA}SAKe$ needs a representative sample of data for calibration and validation. Such phases are both crucial for properly tuning any prediction model, particularly when it is aimed at being implemented into an early-warning system. In some of the cases analyzed in this paper, the number of available activation dates was not large enough to permit the selection of different sub-samples, thus only one date of activation (i.e., the last) was considered for all validations. Nevertheless, such type of approach can be viewed in terms of an "operative" application of the model in an operational warning system (i.e., used to predict the "next" activation, based on the known history of landslide movements in a given area).

With respect to other empirical/hydrological models, the main advantages implemented in $^{GA}SAKe$ are: (i) the automatic calibration of the model by means of genetic algorithms; (ii) the high degrees of freedom of the kernel (in fact, a fixed mathematical function is not required). The adoption of Genetic Algorithms allows for a thorough exploration of the "solution space", and guarantees that best solutions to any problem can be obtained (following Holland's Fundamental Theorem [24]). Moreover, the initial shape of the kernel can be suggested from the operator or even left at random. During model iterations, the shape of the kernels evolves (as their length), thanks to genetic operators, and can reach any type of final configuration. The above features are deemed of outmost value, as they allow to limit subjectivity in the application of a model [70].

If analyzed in detail, the kernels obtained with $^{GA}SAKe$ may appear difficult to understand in physical terms. Nevertheless, in most real cases, slope instability needs to be explained by a complex interplay of several groundwater paths. These latter commonly result in kernels with

quite irregular patterns, and cannot be simulated by simplified analytical functions. According to [71], kernels characterized by complex patterns (and many parameters) are commonly needed to simulate groundwater dynamics. Being characterized by higher complexity, resulting kernels do not necessarily imply greater predictive uncertainties [72,73].

A new release of the model is presently being tested against a set of case studies of different types and extent, selected in diverse geological contexts. Among the improvements, some concern the Genetic Algorithms utilized for the optimization: in particular, a set of selection criteria (roulette, ranking, stochastic tournament, deterministic tournament) will be available shortly, also considering different combinations of ordering criteria (by including the safety margin, the base time, and the first-order momentum to the main fitness of the kernel). Obtained kernels can be post-processed and analyzed in terms of either control points or analytical functions, to allow for deeper hydro-geological ruminations. The final regression of kernels into analytical functions may allow a better understanding of complex groundwater behaviors, and hence landslide responses to antecedent rainfall. Finally, some computational improvements concern smaller requirements of storage capacity and higher execution speed, thanks to parallel optimization that allows for reducing elaborations by ca. 1/50, which will allow improvements in the model performances for an effective implementation in early-warning systems.

**Acknowledgments:** Authors are grateful to Alessio De Rango, Donato D'Ambrosio, William Spataro, and Rocco Rongo (Department of Mathematics and Informatics, University of Calabria, Italy) for discussions and support in the development and testing phases of the model. Authors acknowledge the Editor and three anonymous Referees for their comments and suggestions that allowed improvements to the original version of the manuscript.

**Author Contributions:** All the authors contributed to the design and implementation of the research, to the analysis of the results and to the preparation of the manuscript.

## References

1. Guzzetti, F. Landslides fatalities and the evaluation of landslide risk in Italy. *Eng. Geol.* **2000**, *58*, 89–107. [CrossRef]
2. Iovine, G.; Gariano, S.L.; Terranova, O. Alcune riflessioni sull'esposizione al rischio da frane superficiali alla luce dei recenti eventi in Italia meridionale. *Geologi Calabria* **2009**, *10*, 4–31. (In Italian)
3. Peruccacci, S.; Brunetti, M.T.; Gariano, S.L.; Melillo, M.; Rossi, M.; Guzzetti, F. Rainfall thresholds for possible landslide occurrence in Italy. *Geomorphology* **2017**, *290*, 39–57. [CrossRef]
4. Greco, R.; Comegna, R.; Damiano, E.; Guida, A.; Olivares, L.; Picarelli, L. Hydrological modelling of a slope covered with shallow pyroclastic deposits from field monitoring data. *Hydrol. Earth Syst. Sci.* **2013**, *17*, 4001–4013. [CrossRef]
5. Peres, D.J.; Cancelliere, A. Derivation and evaluation of landslide-triggering thresholds by a Monte Carlo approach. *Hydrol. Earth Syst. Sci.* **2014**, *18*, 4913–4931. [CrossRef]
6. Alvioli, M.; Baum, R.L. Parallelization of the TRIGRS model for rainfall-induced landslides using the message passing interface. *Environ. Modell. Softw.* **2016**, *81*, 122–135. [CrossRef]
7. Rossi, M.; Peruccacci, S.; Brunetti, M.T.; Marchesini, I.; Luciani, S.; Ardizzone, F.; Balducci, V.; Bianchi, C.; Cardinali, M.; Fiorucci, F.M. SANF: National warning system for rainfall-induced landslides in Italy. In *Landslides and Engineered Slopes: Protecting Society through Improved Understanding*; Taylor & Francis Group: London, UK, 2012; pp. 1895–1899.
8. De Luca, D.; Versace, P. Diversity of rainfall thresholds for early warning of hydro-geological disasters. *Adv. Geosci.* **2017**, *44*, 53–60. [CrossRef]
9. Vennari, C.; Gariano, S.L.; Antronico, L.; Brunetti, M.T.; Iovine, G.; Peruccacci, S.; Terranova, O.; Guzzetti, F. Rainfall thresholds for shallow landslide occurrence in Calabria, southern Italy. *Nat. Hazards Earth Syst. Sci.* **2014**, *14*, 317–330. [CrossRef]

10. Gariano, S.L.; Brunetti, M.T.; Iovine, G.; Melillo, M.; Peruccacci, S.; Terranova, O.; Vennari, C.; Guzzetti, F. Calibration and validation of rainfall thresholds for shallow landslide forecasting in Sicily, southern Italy. *Geomorphology* **2015**, *228*, 653–665. [CrossRef]
11. Pisano, L.; Vennari, C.; Vessia, G.; Trabace, M.; Amoruso, G.; Loiacono, P.; Parise, M. Data collection for reconstructing empirical rainfall thresholds for shallow landslides: Challenges and improvements in the Daunia Sub-Apennine (Southern Italy). *Rend. Online Soc. Geol. Ital.* **2015**, *35*, 236–239. [CrossRef]
12. Melillo, M.; Brunetti, M.T.; Peruccacci, S.; Gariano, S.L.; Guzzetti, F. Rainfall thresholds for the possible landslide occurrence in Sicily (Southern Italy) based on the automatic reconstruction of rainfall events. *Landslides* **2016**, *13*, 165–172. [CrossRef]
13. Piciullo, L.; Gariano, S.L.; Melillo, M.; Brunetti, M.T.; Peruccacci, S.; Guzzetti, F.; Calvello, M. Definition and performance of a threshold-based regional early warning model for rainfall-induced landslides. *Landslides* **2017**, *14*, 995–1008. [CrossRef]
14. Iovine, G.; Iaquinta, P.; Terranova, O. Emergency management of landslide risk during Autumn-Winter 2008/2009 in Calabria (Italy). The example of San Benedetto Ullano. In Proceedings of the 18th World IMACS Congress and MODSIM09 International Congress on Modelling and Simulation, Cairns, Australia, 13–17 July 2009; pp. 2686–2693.
15. Iovine, G.; Petrucci, O.; Rizzo, V.; Tansi, C. The March 7th 2005 Cavallerizzo (Cerzeto) landslide in Calabria-Southern Italy. In Proceeding of the 10th IAEG Congress: Engineering Geology for Tomorrow's Cities, Nottingham, UK, 6–10 September 2006.
16. Terranova, O.; Lollino, P.; Gariano, S.L.; Iaquinta, P.; Iovine, G. Un sistema integrato di sorveglianza per la mitigazione del rischio da frana. *Geologi Calabria* **2010**, *11*, 6–28. (In Italian)
17. Terranova, O.; Gariano, S.L.; Iaquinta, P.; Iovine, G. $^{GA}$SAKe: Forecasting landslide activations by a genetic-algorithms-based hydrological model. *Geosci. Model Dev.* **2015**, *8*, 1955–1978. [CrossRef]
18. Terranova, O.; Iaquinta, P.; Gariano, S.L.; Greco, R.; Iovine, G. $^{CM}$SAKe: A hydrological model to forecasting landslide activations. In *Landslide Science and Practice*; Springer: Berlin, Germany, 2013; pp. 73–79.
19. Sirangelo, B.; Versace, P. A real time forecasting for landslides triggered by rainfall. *Meccanica* **1996**, *31*, 1–13. [CrossRef]
20. Capparelli, G.; Versace, P. FLaIR and SUSHI: Two mathematical models for early warning of landslides induced by rainfall. *Landslides* **2011**, *8*, 67–79. [CrossRef]
21. Peres, D.J.; Cancelliere, A. Defining rainfall thresholds for early warning of rainfall-triggered landslides: The case of North-East Sicily. In *Landslide Science and Practice*; Springer: Berlin, Germany, 2013; pp. 257–263.
22. Capparelli, G.; Giorgio, M.; Greco, R. Shallow landslides risk mitigation by early warning: The Sarno case. In *Landslide Science and Practice*; Springer: Berlin, Germany, 2013; pp. 767–772.
23. Greco, R.; Giorgio, M.; Capparelli, G.; Versace, P. Early warning of rainfall-induced landslides based on empirical mobility function predictor. *Eng. Geol.* **2013**, *153*, 68–79. [CrossRef]
24. Holland, J.H. *Adaptation in Natural and Artificial Systems: An Introductory Analysis with Applications to Biology, Control and Artificial Intelligence*; MIT Press: Cambridge, MA, USA, 1992; ISBN 0262082136.
25. D'Ambrosio, D.; Spataro, W.; Rongo, R.; Iovine, G. Genetic algorithms, optimization, and evolutionary modeling. In *Treatise on Geomorphology. Quantitative Modeling of Geomorphology*; Shroder, J., Baas, A.C.W., Eds.; Academic Press: San Diego, CA, USA, 2013; pp. 74–97.
26. Amodio-Morelli, L.; Bonardi, G.; Colonna, V.; Dietrich, D.; Giunta, G.; Ippolito, F.; Liguori, V.; Lorenzoni, S.; Paglionico, A.; Perrone, V. L'arco calabro-peloritano nell'orogene appenninico-maghrebide. *Mem. Soc. Geol. Ital.* **1976**, *17*, 1–60. (In Italian)
27. Monaco, C.; Tortorici, L. Active faulting in the Calabrian Arc and eastern Sicily. *J. Geodyn.* **2000**, *29*, 407–424. [CrossRef]
28. Tortorici, L.; Monaco, C.; Tansi, C.; Cocina, O. Recent and active tectonics in the Calabrian Arc (southern Italy). *Tectonophysics* **1995**, *243*, 37–55. [CrossRef]
29. Van Dijk, J.P.; Bello, M.; Brancaleoni, G.P.; Cantarella, G.; Costa, V.; Frixa, A.; Golfetto, F.; Merlini, S.; Riva, M.; Torricelli, S.; Toscano, C.; Zerilli, A. A regional structural model for the northern sector of the Calabrian Arc (southern Italy). *Tectonophysics* **2000**, *324*, 267–320. [CrossRef]
30. Tansi, C.; Muto, F.; Critelli, S.; Iovine, G. Neogene-Quaternary strike-slip tectonics in the central Calabrian Arc (southern Italy). *J. Geodyn.* **2007**, *43*, 393–414. [CrossRef]

31. Sorriso-Valvo, G.M. Mass movements and slope evolution in Calabria. Proceedings of 4th International Conference and Field Workshop on Landslides, Tokyo, Japan, 23–31 August 1985; pp. 23–30.
32. Carrara, A.; Catalano, E.; Sorriso-Valvo, G.M.; Reali, C.; Merenda, L.; Rizzo, V. Landslide morphometry and typology in two zones, Calabria, Italy. *Bull. Eng. Geol. Environ.* **1977**, *16*, 8–13.
33. Carrara, A.; Merenda, L.; Nicoletti, P.G.; Sorriso-Valvo, G.M. Slope instability in Calabria, Italy. In Proceedings of the Polish-Italian Seminar on Superficial Mass Movement in Mountain Regions, Szymbark, Poland, 17–19 May 1979; pp. 47–62.
34. Crescenzi, E.; Grassi, D.; Iovine, G.; Merenda, L.; Miceli, F.; Sdao, F. Fenomeni di instabilità franosa nei centri abitati calabri: Esempi rappresentativi. *Geol. Appl. Hydrogeo.* **1996**, *31*, 203–226. (In Italian)
35. Iovine, G.; Merenda, L. Nota illustrativa alla "Carta delle frane e della mobilizzazione diastrofica dal 1973 ad oggi nel bacino del Torrente Straface (Alto Jonio; Calabria)". *Geol. Appl. Hydrogeol.* **1996**, *31*, 107–128. (In Italian)
36. Iovine, G.; Petrucci, O. Effetti sui versanti e nel fondovalle indotti da un evento pluviale eccezionale nel bacino di una fiumara calabra (T. Pagliara). *Boll. Soc. Geol. Ital.* **1998**, *117*, 821–840. (In Italian)
37. Iovine, G.; Parise, M.; Tansi, C. Slope movements and tectonics in North-Eastern Calabria (Southern Italy). In Proceedings of the 7th International Symposium on Landslides (ISL'96): Landslides Glissements de Terrain, Trondheim, 17–21 June 1996; pp. 785–790.
38. Ferrari, E.; Iovine, G.; Petrucci, O. Evaluating landslide hazard through geomorphologic, hydrologic and historical analyses in north-eastern Calabria (southern Italy). In Proceedings of the EGS Plinius Conference on Mediterranean Storms, Maratea, Italia, 14–16 October 1999; pp. 425–438.
39. Tansi, C.; Iovine, G.; Folino-Gallo, M. Tettonica attiva e recente; e manifestazioni gravitative profonde; lungo il bordo orientale del graben del Fiume Crati (Calabria settentrionale). *Boll. Soc. Geol. Ital.* **2005**, *124*, 563–578. (In Italian)
40. Köppen, W.P. *Climatologia con un Estudio de los Climas de la Tierra*; Fondo de Cultura Economica: Ciudad de Mexico City, Mexico, 1948; p. 479.
41. Terranova, O. Caratteristiche degli eventi pluviometrici a scala giornaliera in Calabria. In Proceeding of the XXIX Convegno di Idraulica e Costruzioni Idrauliche, Trento, Italy, 7–10 September 2004; pp. 343–350. (In Italian)
42. Terranova, O.; Gariano, S.L. Rainstorms able to induce flash floods in a Mediterranean-climate region (Calabria, southern Italy). *Nat. Hazard Earth Syst. Sci.* **2014**, *14*, 2423–2434. [CrossRef]
43. Ferrari, E.; Terranova, O. Non-parametric detection of trends and change point years in monthly and annual rainfalls. In Proceedings of the 1st Italian-Russian Workshop on New Trend in Hydrology, Rende (CS), Italy, 24–26 September 2002; pp. 177–188. (In Italian)
44. Terranova, O.; Gariano, S.L. Regional investigation on seasonality of erosivity in the Mediterranean environment. *Environ. Earth Sci.* **2015**, *73*, 311–324. [CrossRef]
45. Iovine, G.; Tansi, C.; Folino-Gallo, M. Strutture da accomodamento tettono-gravitativo nell'evoluzione tardiva dei sistemi di catena: Il caso di studio di Acri (Calabria settentrionale). *Boll. Soc. Geol. Ital.* **2004**, *123*, 39–51. (In Italian)
46. Tansi, C.; Talarico, A.; Iovine, G.; Folino Gallo, M.; Falcone, G. Interpretation of radon anomalies in seismotectonic and tectonic-gravitational setting of the south-eastern Crati Graben (Northern Calabria, Italy). *Tectonophysics* **2005**, *396*, 181–193. [CrossRef]
47. *Carta Geologica della Calabria*; CASMEZ: Ercolano, Napoli, Italia, 1967. (In Italian)
48. Sorriso-Valvo, G.M. *1:250,000 Scale Map of the Large Landslides and of the Deep-Seated Gravitational Slope Deformations of Calabria*; Selca: Firenze, Italia, 1996.
49. Terranova, O.; Antronico, L.; Gullà, G. Landslide triggering scenarios in homogeneous geological contexts: The area surrounding Acri (Calabria, Italy). *Geomorphology* **2007**, *87*, 250–267. [CrossRef]
50. Gariano, S.L.; Terranova, O.G.; Greco, R.; Iaquinta, P.; Iovine, G. Forecasting the timing of activation of rainfall-induced landslides. An application of GA-SAKe to the Acri case study (Calabria, Southern Italy). *Geophys. Res. Abstr.* **2013**, *15*, EGU2013-678.
51. Iovine, G.; Lollino, P.; Gariano, S.L.; Terranova, O. Coupling limit equilibrium analyses and real-time monitoring to refine a landslide surveillance system in Calabria (southern Italy). *Nat. Hazard Earth Syst. Sci.* **2010**, *10*, 2341–2354. [CrossRef]

52. Capparelli, G.; Iaquinta, P.; Iovine, G.; Terranova, O.G.; Versace, P. Modelling the rainfall-induced mobilization of a large slope movement in northern Calabria. *Nat. Hazards* **2012**, *61*, 247–256. [CrossRef]
53. Sorriso-Valvo, G.M.; Antronico, L.; Catalano, E.; Gullà, G.; Tansi, C.; Dramis, F.; Ferrucci, F.; Fantucci, R. *The Temporal Stability and Activity of Landslides in Europe with Respect to Climatic Change (TESLEC)*; Final Report; Istituto di Ricerca per la Protezione Idrogeologica (IRPI): Turin, Italy, 1996.
54. Iovine, G.; De Rango, A.; Gariano, S.L.; Terranova, O. Forecasting landslide activations by means of GA-SAKe. An example of application to three case studies in Calabria (Southern Italy). *Geophys. Res. Abstr.* **2016**, *18*, 4645.
55. Ippolito, F.; D'Argenio, B.; Pescatore, T.; Scandone, P. Structural–stratigraphic units and tectonic framework of Southern Apennines. In *Geology of Italy*; Squyres, C., Ed.; Earth Sciences Society of the Libyan Arab Republic: Tripoli, Libya, 1975; pp. 317–328.
56. Di Crescenzo, G.; Santo, A. Analisi morfologica delle frane da scorrimento-colata rapida in depositi piroclastici della Penisola Sorrentina (Campania). *Geogr. Fis. Dinam. Quat.* **1999**, *22*, 57–72. (In Italian)
57. Ducci, D.; Tranfaglia, G. L'impatto dei cambiamenti climatici sulle risorse idriche sotterranee in Campania. *Boll Ordine Geol. Campania* **2005**, *1–4*, 13–21. (In Italian)
58. *Servizio Idrografico. Annali Idrologici: Parte I*; Compartimento di Napoli, Istituto poligrafico e Zecca dello Stato: Rome, Italy, 1948–1999.
59. Rossi, F.; Villani, P. *Valutazione Delle Piene in Campania*; CNR-GNDCI publications No. 1470; Grafica Metelliana: Cava de' Tirreni, Italia, 1994. (In Italian)
60. Mele, R.; Del Prete, S. Lo studio della franosità storica come utile strumento per la valutazione della pericolosità da frane. Un esempio nell'area di Gragnano (Campania). *Boll. Soc. Geol. Ital.* **1999**, *118*, 91–111. (In Italian)
61. Calcaterra, D.; Santo, A. The January 10, 1997 Pozzano landslide, Sorrento Peninsula, Italy. *Eng. Geol.* **2004**, *75*, 181–200.
62. Di Crescenzo, G.; Santo, A. Debris slides-rapid earth flows in the carbonate massifs of the Campania region (Southern Italy): Morphological and morphometric data for evaluating triggering susceptibility. *Geomorphology* **2005**, *66*, 255–276.
63. Cascini, L.; Sorbino, G.; Cuomo, S.; Ferlisi, S. Seasonal effects of rainfall on the shallow pyroclastic deposits of the Campania region (southern Italy). *Landslides* **2014**, *11*, 779–792. [CrossRef]
64. Terranova, O.; Greco, V.R.; Gariano, S.L.; Pascale, S.; Rago, V.; Caloiero, P.; Iovine, G. Monitoring and modelling for landslide risk mitigation and reduction. The case study of San Benedetto Ullano (Northern Calabria-Italy). *Geophys. Res. Abstr.* **2016**, *18*, 4708.
65. Peres, D.J.; Cancelliere, A.; Greco, R.; Bogaard, T.A. Influence of uncertain identification of triggering rainfall on the assessment of landslide early warning thresholds. *Nat. Hazards Earth Syst. Sci. Discuss.* **2017**. [CrossRef]
66. Nikolopoulos, E.I.; Crema, S.; Marchi, L.; Marra, F.; Guzzetti, F.; Borga, M. Impact of uncertainty in rainfall estimation on the identification of rainfall thresholds for debris flow occurrence. *Geomorphology* **2014**, *221*, 286–297. [CrossRef]
67. Marra, F.; Destro, E.; Nikolopoulos, E.I.; Zoccatelli, D.; Creutin, J.D.; Guzzetti, F.; Borga, M. Impact of rainfall spatial aggregation on the identification of debris flow occurrence thresholds. *Hydrol. Earth Syst. Sci.* **2017**, *21*, 4525–4532. [CrossRef]
68. Gabriele, S.; Terranova, O.; Pascale, S.; Rago, V.; Chiaravalloti, F.; Sabatino, P.; Brocca, L.; Laviola, S.; Baldini, L.; Federico, S. RAMSES: A nowcasting system for mitigating geo-hydrological risk along the railway. *Geophys. Res. Abstr.* **2016**, *18*, 8462.
69. Rago, V.; Chiaravalloti, F.; Chiodo, G.; Gabriele, S.; Lupiano, V.; Nicastro, R.; Pellegrino, A.D.; Procopio, A.; Siviglia, S.; Terranova, O.G.; Iovine, G. Geomorphic effects caused by heavy rainfall in southern Calabria (Italy) on 30 October–1 November 2015. *J. Maps* **2017**, *13*, 836–843. [CrossRef]
70. D'Ambrosio, D.; Spataro, W.; Rongo, R.; Iovine, G. Genetic algorithms, optimization, and evolutionary modeling. In *Treatise on Geomorphology, Volume 2, Quantitative Modeling of Geomorphology*; Baas, A., Ed.; Academic Press: San Diego, CA, USA, 2013; pp. 74–97.
71. Pinault, J.-L.; Plagnes, V.; Aquilina, L. Inverse modeling of the hydrological and the hydrochemical behavior of hydrosystems: Characterization of karst system functioning. *Water Resour. Res.* **2001**, *37*, 2191–2204. [CrossRef]

72. Fienen, M.N.; Doherty, J.E.; Hunt, R.J.; Reeves, H. *Using Prediction Uncertainty Analysis to Design Hydrologic Monitoring Networks: Example Applications from the Great Lakes Water Availability Pilot Project*; Scientific Investigations Report 2010-5159, U.S. Geological Survey: Reston, VA, USA, 2010.
73. Long, A.J. RRAWFLOW: Rainfall-response aquifer and watershed flow model (v1.15). *Geosci. Model Dev.* **2015**, *8*, 865–880. [CrossRef]

# 6

# Hydrological Hazard: Analysis and Prevention

**Tommaso Caloiero**

National Research Council—Institute for Agricultural and Forest Systems in Mediterranean (CNR-ISAFOM), Via Cavour 4/6, 87036 Rende (CS), Italy; tommaso.caloiero@isafom.cnr.it

**Abstract:** As a result of the considerable impacts of hydrological hazard on water resources, on natural environments and human activities, as well as on human health and safety, climate variability and climate change have become key issues for the research community. In fact, a warmer climate, with its heightened climate variability, will increase the risk of hydrological extreme phenomena, such as droughts and floods. The Special Issue "Hydrological Hazard: Analysis and Prevention" presents a collection of scientific contributions that provides a sample of the state-of-the-art and forefront research in this field. In particular, innovative modelling methods for flood hazards, regional flood and drought analysis, and the use of satellite and climate data for drought analysis were the main topics and practice targets that the papers published in this Special Issue aimed to address.

**Keywords:** catchment; climate; drought; flood; forecast; hazards; landslide; modelling; precipitation; temperature

## 1. Introduction

As a result of economic and population growth in the world, the fifth Intergovernmental Panel on Climate Change (IPCC) report [1] evidenced an increase in anthropogenic greenhouse gas emissions (carbon dioxide, methane, and nitrous oxide) whose atmospheric concentrations reached values never touched in at least the past 800,000 years. Consequently, the IPCC report showed an increase of about 0.9 °C in the Earth's surface temperature in the twentieth century and forecasted a further increase for the twenty-first century, with natural and anthropic consequences [1]. In fact, anthropic systems and terrestrial ecosystems are becoming more vulnerable to environmental phenomena and an increase in floods, heat waves, forest fires, and droughts can be expected [2,3]. Within such a purview, scholarly investigation has primarily focused on multiple analyses of meteorological, hydrological, and climatological variables based on different methodologies.

Given the above scenario, the call for papers for publication in the Special Issue "Hydrological Hazard: Analysis and Prevention", which was launched in October 2017, aimed to consider innovative approaches to the analysis, prediction, prevention, and mitigation of hydrological extremes. With this aim, interdisciplinary original research articles highlighting new ideas, approaches, and innovations in the analysis of various types of droughts (e.g., meteorological, agricultural, and hydrological drought) and various types of floods (e.g., fluvial, coastal, and pluvial) were welcomed.

Potential topics of this Special Issue of Geosciences included, but were not limited to, the following:

- Regional flood and drought analysis
- Case studies and comparative studies in different parts of the world
- Analyses of regional/global patterns and trends
- Effects of land-use or land-cover change on hydrological extremes
- Prediction and prevention of hydrological extremes
- Use of satellite and climate data for drought analysis
- Innovative modelling methods for flood hazards

- Strategies for reducing the vulnerability to hydrological extremes
- Climate change and hydrogeological risk

## 2. Some Data of the Special Issue

From early January 2018 to late September 2018, a total of 18 papers have been submitted for consideration for publication in the Special Issue. After a rigorous editorial check and peer-review processes, which involved external and independent experts in the field, 4 papers were rejected, 1 paper has been withdrawn, and 13 papers have been accepted, with an acceptance rate of about 72%.

Among the 13 articles published in the Special Issue, 1 is a Technical Note (Terranova et al. [4]), 11 are Research Articles [5–15], and one is a Case Report (Schmid-Breton et al. [16]).

Figure 1 compares the geographic distribution of the authors and research teams publishing in the Special Issue (Figure 1a), as well as of the case studies and demonstration sites (Figure 1b). The analysis of this figure allows one to have an idea of the scientific community working on hydrological hazards, although it is just a sample and thus is not an exhaustive representation. Thirty-nine authors from three different continents (North America, Europe, and Oceania) contributed to the Special Issue, showing results of case studies and demonstration sites involving five continents (North America, Europe, Africa, Asia, and Oceania).

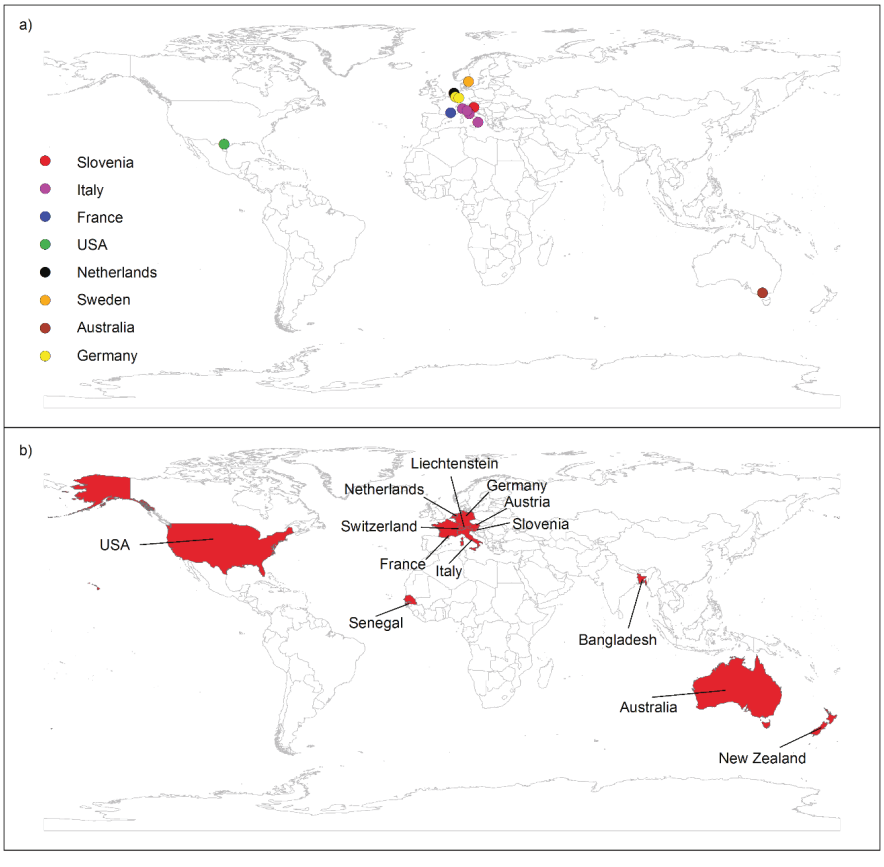


**Figure 1.** Geographic distribution of (**a**) authors and research teams publishing in the Special Issue; (**b**) case studies and demonstration sites that are discussed in the papers.

Figure 2 shows the word cloud of the keywords published in the papers of the Special Issue. From the analysis of the word cloud, it can be easily seen that "Flood" is the predominant keyword, cited in 8 out of 13 articles, followed by "Modelling" (6 out of 13), and "Catchment" (or basin) and "Precipitation" (or rainfall), which have each been cited in 3 papers.

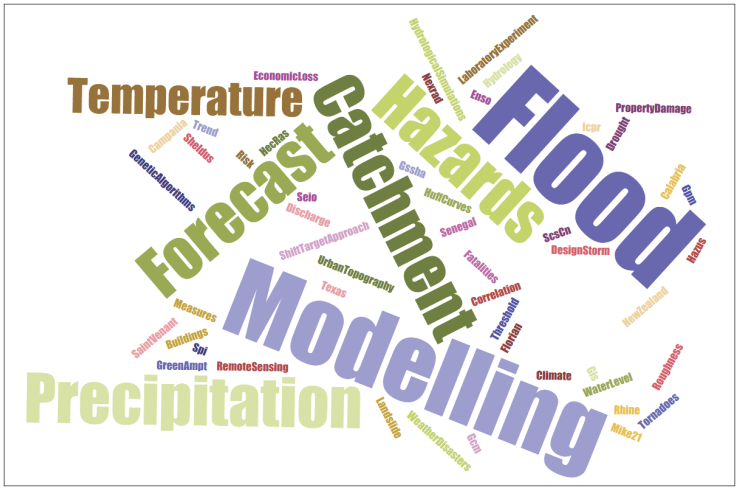


**Figure 2.** Word cloud of the keywords published in the papers [4–14] of this Special Issue.

### 3. Overview of the Special Issue Contributions

Terranova et al. [4] applied the GASAKe, an empirical-hydrological model that aims at forecasting the time of occurrence of landslides, in four case studies in two different regions of Italy—three rock slides in Calabria and one soil slip in Campania. As a result, for two of the Calabrian rock slides, the activation dates were correctly predicted by the model, probably thanks to an accurate knowledge of the activation history of the landslide and a proper hydrological characterization of the site. For such cases, GASAKe could be applied to predict the timing of activation of future landslide activations in the same areas. In the other two cases, weaker model performances have been detected, probably because of an inaccurate knowledge of the activation dates and/or rainfall series.

Bezak et al. [5] investigated the impact of the design rainfall on the combined 1D/2D hydraulic modelling results in the Glinščica Stream catchment (Slovenia), which is ungauged in terms of discharges. In particular, Bezak et al. [5] evaluated 10 different design rainfall events (scenarios) that were used as inputs to the hydrological model. Using calibrated and validated hydrological models, the inputs for the hydraulic model were determined. The results indicated that the selection of the design rainfall event should be regarded as an important step, as the hydraulic modelling results for different scenarios differ significantly. As an example, the maximum flooded area extent was twice as large as the minimum one, and the maximum water velocity over flooded areas was more than 10 times larger than the minimum one. This means that the design rainfall definition can significantly influence the hydraulic modelling results, leading to the production of very different flood hazard maps, and consequently the planning of very different flood protection schemes.

Beretta et al. [6] tested three different methods to simulate the influence of buildings on flood inundation by performing a number of laboratory experiments carried out with a simplified urban district physical model, and reconstructing results with a hydraulic mathematical model considering both the solution of the full shallow water equations and the diffusive simplification. Simplified methods were also tested for the simulation of a real flood event, which occurred in 2013 in the city of

Olbia, Italy. The results showed that use of a 2D diffusive model and setting a high friction instead of detailed building geometry are effective methods to assess flood inundation extent.

Lombardi et al. [7] suggested a low computational cost method to produce a probabilistic flood prediction system using a single forecast precipitation scenario perturbed via a spatial shift. The method was applied to three basins located in the northern part of Milan city (northern Italy): Seveso, Olona, and Lambro. To produce hydro-meteorological simulations and forecasts, a flood forecasting system, which comprises the physically-based rainfall-runoff hydrological model FEST-WB and the MOLOCH meteorological model, has been used. In particular, the performance of the shift-target approach was compared with the "unperturbed" MOLOCH forecast over a period of four years. The results showed how the shift-target approach complements the deterministic MOLOCH-based flood forecast for warning purposes.

Bouvier et al. [8] analyzed the skill of two well-known event-based models, the Soil Conservation Service model and the Green-Ampt model, in reproducing the flood processes in a semi-arid agricultural catchment of Senegal (Ndiba). In particular, twenty-eight flood events have been extracted and modelled. As a result, both the models were able to reproduce the flood events after calibration, but they had to account for the fact that the infiltration processes are highly dependent on the tillage of the soils and the growing of the crops during the rainy season, which made the initialization of the event-based models difficult. Specifically, the Soil Conservation Service model performed better than the Green-Ampt model, because the latter was very sensitive to the variability of the hydraulic conductivity at saturation. The variability of the parameters of the models highlights the complexity of this kind of cultivated catchment, with highly non-stationary conditions.

Caloiero [9] studied dry and wet periods in New Zealand using the Standardized Precipitation Index (SPI) and by means of a new graphical technique, the Innovative Trend Analysis (ITA), which allows trend identification of the low, medium, and high values of a series. The results show that, in every area currently subject to drought, an increase of this phenomenon can be expected. Specifically, the results of the paper highlighted that agricultural regions on the eastern side of the South Island, as well as the north-eastern regions of the North Island, are the most consistently vulnerable areas. In fact, in these regions, the trend analysis mainly showed a general reduction in all the values of the SPI; that is, a tendency toward heavier droughts and weaker wet periods.

Paul et al. [10] analyzed the fatality rates caused by hydrometeorological disasters in Texas for the period 1959–2016 in an effort to identify counties and metropolitan areas that have a greater risk for particular hydrometeorological disasters. The study examined temporal trends, spatial variations, and demographic characteristics of the victims from 1959–2016. The results showed that the number of hydrometeorological fatalities in Texas has increased over the 58-year study period, but the per capita fatalities have significantly decreased. Moreover, seasonal and monthly stratification identifies spring and summer as the deadliest seasons, with the month of May registering the highest number of total fatalities dominated by flooding and tornado fatalities. Finally, demographic trends of hydrometeorological disaster fatalities indicated approximately twice the amount of male fatalities than female fatalities from 1959–2016 and that adults are the highest fatality risk group overall.

Hossain et al. [11] assessed the efficiency of a non-linear regression technique in predicting long-term seasonal rainfall. The non-linear models were developed using the lagged (past) values of the climate drivers, which have a significant correlation with rainfall. More specifically, the capabilities of south-eastern Indian Ocean and El Nino Southern Oscillation were assessed in reproducing the rainfall characteristics using the non-linear regression approach. Three rainfall stations located in the Australian Capital Territory were selected as a case study. The analysis suggested that the predictors that have the highest correlation with the predictands do not necessarily produce the least errors in rainfall forecasting. The outcomes of the analysis could help the watershed management authorities to adopt an efficient modelling technique by predicting long-term seasonal rainfall.

Furl et al. [12] investigated the performance of several satellite precipitation products with respect to gauge corrected ground-based radar estimations for nine moderate to high magnitude events

across the Guadalupe River system in south Texas. The analysis was conducted across three nested watersheds (with area ranging from 200 to 10,000 $km^2$) to capture and quantify the effect of the scale on the propagation of the error. In order to understand the propagation of rainfall error into the predicted runoff, hydrologic model simulations were implemented. In particular, the Gridded Surface Subsurface Hydrologic Analysis, a physically-based fully distributed hydrologic model, forced with those ten satellite-based precipitation products, was used to simulate the rainfall-runoff relationship for the basins. The results showed that the satellite-based precipitation products provide very high spatiotemporal resolution precipitation estimates. However, the estimates lack accuracy, especially at a local scale. The products underestimate heavy storm events significantly, and the errors were amplified in the runoff hydrographs generated.

Islam et al. [13] assessed the present and future water level and discharge in the Betna River (Bangladesh) by applying a process-based hydrodynamic model (MIKE 21 FM) to simulate water level and discharge under different future climate conditions. The MIKE 21 FM model for the Betna River was set up, calibrated, and validated using the observed water level and discharge data. The model was then used to project the future (2040s and 2090s) water level and discharge. The modelling results indicated that, compared with the baseline year (2014–2015), both the water level and the monsoon daily maximum discharge are expected to increase by the 2040s and by the 2090s, with the sea level rise mostly responsible for the increase in water level.

Ferrari et al. [14] carried out a joint analysis of temperature and rainfall data by comparing time series recorded in some gauges located in Calabria (Southern Italy) over two distinct 30-year sub-periods (1951–1980 and 1981–2010). In particular, the anomalies of the seasonal values of temperature and precipitation, standardized by means of the mean values and the standard deviations of the period 1961–1990, were analyzed. The series has been selected based on the normality hypothesis. The isocontour lines of the probability density function for the bivariate Gaussian distribution have been considered as ellipses centered on the vector mean of each sub-period. Specifically, the displacements of the ellipses have been quantified and tested for each season, passing from the first sub-period to the following one. The main results concern a decreasing trend of both the temperature and the rainfall anomalies, predominantly in the winter and autumn seasons.

Paul and Sharif [15] tried to verify the assertion that the increase in property damage is a combined contribution of stronger disasters as predicted by climate change models and increases in urban development in risk prone regions such as the Texas Gulf Coast. Within this aim, the study intended to provide a review of historic trends and types of damage and economic losses caused by hydrometeorological disasters impacting the coastal and inland property and infrastructure of Texas from 1960–2016. Spatial analysis of actual and normalized damage, as well as a supplemental assessment of three major disasters causing extensive damage in Texas (Hurricanes Carla 1961, Hurricane Alicia 1983, and Hurricane Ike 2008), highlight the risk as a function of wind or flooding damage and the growth of exposure in hazard prone regions.

Schmid-Breton et al. [16] presented the method and the GIS-tool named "ICPR FloRiAn (Flood Risk Analysis)", developed by the International Commission for the Protection of the Rhine (ICPR) to enable the broad-scale assessment of the effectiveness of flood risk management measures on the Rhine. Moreover, the first calculation results have been also shown. The tool uses flood hazard maps and associated recurrence periods for an overall damage and risk assessment for four receptors: human health, environment, culture heritage, and economic activity. For each receptor, a method is designed to calculate the impact of flooding and the effect of measures. The tool consists of three interacting modules: damage assessment, risk assessment, and measures. Calculations using this tool showed that the flood risk reduction target defined in the Action Plan on Floods of the ICPR in 1998 could be achieved with the measures already taken and those planned until 2030.

**Acknowledgments:** The Guest Editor thanks all the authors, Geosciences' editors, and reviewers for their great contributions and commitment to this Special Issue. A special thank goes to Daisy Hu, Geoscience's Assistant Editor, for her dedication to this project and her valuable collaboration in the design and setup of the Special Issue.

## References


1. IPCC. Summary for Policymakers. In *Fifth Assessment Report of the Intergovernmental Panel on Climate Change*; Cambridge University Press: Cambridge, UK, 2013.
2. Estrela, T.; Vargas, E. Drought management plans in the European Union. *Water Resour. Manag.* **2010**, *26*, 1537–1553. [CrossRef]
3. Kreibich, H.; Di Baldassarre, G.; Vorogushyn, S.; Aerts, J.C.J.H.; Apel, H.; Aronica, G.T.; Arnbjerg-Nielsen, K.; Bouwer, L.M.; Bubeck, P.; Caloiero, T.; et al. Adaptation to flood risk: Results of international paired flood event studies. *Earths Future* **2017**, *5*, 953–965. [CrossRef]
4. Terranova, O.; Gariano, S.L.; Iaquinta, P.; Lupiano, V.; Rago, V.; Iovine, G. Examples of Application of $^{GA}$SAKe for Predicting the Occurrence of Rainfall-Induced Landslides in Southern Italy. *Geosciences* **2018**, *8*, 78. [CrossRef]
5. Bezak, N.; Šraj, M.; Rusjan, S.; Mikoš, M. Impact of the Rainfall Duration and Temporal Rainfall Distribution Defined Using the Huff Curves on the Hydraulic Flood Modelling Results. *Geosciences* **2018**, *8*, 69. [CrossRef]
6. Beretta, R.; Ravazzani, G.; Maiorano, C.; Mancini, M. Simulating the Influence of Buildings on Flood Inundation in Urban Areas. *Geosciences* **2018**, *8*, 77. [CrossRef]
7. Lombardi, G.; Ceppi, A.; Ravazzani, G.; Davolio, S.; Mancini, M. From Deterministic to Probabilistic Forecasts: The 'Shift-Target' Approach in the Milan Urban Area (Northern Italy). *Geosciences* **2018**, *8*, 181. [CrossRef]
8. Bouvier, C.; Bouchenaki, L.; Tramblay, Y. Comparison of SCS and Green-Ampt Distributed Models for Flood Modelling in a Small Cultivated Catchment in Senegal. *Geosciences* **2018**, *8*, 122. [CrossRef]
9. Caloiero, T. SPI Trend Analysis of New Zealand Applying the ITA Technique. *Geosciences* **2018**, *8*, 101. [CrossRef]
10. Paul, S.H.; Sharif, H.O.; Crawford, A.M. Fatalities Caused by Hydrometeorological Disasters in Texas. *Geosciences* **2018**, *8*, 186. [CrossRef]
11. Hossain, I.; Esha, R.; Imteaz, M.A. An Attempt to Use Non-Linear Regression Modelling Technique in Long-Term Seasonal Rainfall Forecasting for Australian Capital Territory. *Geosciences* **2018**, *8*, 282. [CrossRef]
12. Furl, C.; Ghebreyesus, D.; Sharif, H.O. Assessment of the Performance of Satellite-Based Precipitation Products for Flood Events across Diverse Spatial Scales Using GSSHA Modeling System. *Geosciences* **2018**, *8*, 191. [CrossRef]
13. Islam, M.M.M.; Hofstra, N.; Sokolova, E. Modelling the Present and Future Water Level and Discharge of the Tidal Betna River. *Geosciences* **2018**, *8*, 271. [CrossRef]
14. Ferrari, E.; Coscarelli, R.; Sirangelo, B. Correlation Analysis of Seasonal Temperature and Precipitation in a Region of Southern Italy. *Geosciences* **2018**, *8*, 160. [CrossRef]
15. Paul, S.H.; Sharif, H.O. Analysis of Damage Caused by Hydrometeorological Disasters in Texas, 1960–2016. *Geosciences* **2018**, *8*, 384. [CrossRef]
16. Schmid-Breton, A.; Kutschera, G.; Botterhuis, T.; ICPR Expert Group 'Flood Risk Analysis'. A Novel Method for Evaluation of Flood Risk Reduction Strategies: Explanation of ICPR FloRiAn GIS-Tool and Its First Application to the Rhine River Basin. *Geosciences* **2018**, *8*, 371. [CrossRef]

# 7

# Comparison of SCS and Green-Ampt Distributed Models for Flood Modelling in a Small Cultivated Catchment in Senegal

**Christophe Bouvier *, Lamia Bouchenaki and Yves Tramblay**

Institut de Recherche pour le Développement (IRD), HydroSciences Montpellier, UMR 5569 CNRS-IRD-UM, 34000 Montpellier, France; bouchenaki.lamia@gmail.com (L.B.); yves.tramblay@ird.fr (Y.T.)
* Correspondence: jean-christophe.bouvier@umontpellier.fr

**Abstract:** The vulnerability to floods in Africa has increased over the last decades, together with a modification of land cover as urbanized areas are increasing, agricultural practices are changing, and deforestation is increasing. Rainfall-runoff models that properly represent land use change and hydrologic response should be useful for the development of water management and mitigation plans. Although some studies have applied rainfall-runoff models in West Africa for flood modelling, there is still a need to develop such models, while many data are available and have not still been used for modelling improvement. The Ndiba catchment (16.2 $km^2$), which is located in an agricultural area in south Senegal, is such catchment, where a lot of hydro-climatic data has been collected between 1983 and 1992. Twenty-eight flood events have been extracted and modelled by two event-based rainfall-runoff models that are based on the Soil Conservation Service (SCS) or the Green-Ampt (GA) models for runoff, both coupled with the distributed Lag and Route (LR) for routing. Both models were able to reproduce the flood events after calibration, but they had to account for that the infiltration processes are highly dependent on the tillage of the soils and the growing of the crops during the rainy season, which made the initialization of the event-based models difficult. The most influent parameters for both models (the maximal water storage capacity for SCS, the hydraulic conductivity at saturation for Green-Ampt) were mostly related to the development stage of the vegetation, described by a Normalized Difference Vegetation Index (NDVI) anomaly. The SCS model performed finally better than the Green-Ampt model, because Green-Ampt was very sensitive to the variability of the hydraulic conductivity at saturation. The variability of the parameters of the models highlights the complexity of this kind of cultivated catchment, with highly non stationary conditions. The models could be improved by a better knowledge of the tillage practices, and a better integration of these practices in the parameters predictors.

**Keywords:** flood modelling; Agricultural Small Catchment; SCS-CN; Green-Ampt; Senegal

## 1. Introduction

The vulnerability to floods in Africa has increased over the last decades, in terms of human fatalities and economic losses [1], while in most of African countries, flood warning and prevision systems are not existent [2]. Consequently, there is a need for a better knowledge of these events and to improve rainfall-runoff models that could be used in the development of prevision systems. However, up to now, only a few studies have applied rainfall-runoff models in West Africa for flood modelling (e.g., [3,4]) or the analysis of the hydrological processes in small catchments less than some tenth or hundreds of squared kilometers [5,6]. In West Africa, flood prediction usually derive from synthetic guidelines [7] or regional studies [8–10]. But, such works are now ancient and could be

revisited or developed, while many data are available in West Africa and have not still been used for modelling improvement.

The small agricultural area Thysse Kaymor is one of these catchments that have not been the object of modelling studies at the catchment scale, despite that many hydro-climatic data have been collected. Five nested catchments have been monitored during the period 1982–1992, including rainfall, runoff, and water content and hydrodynamic properties of the soils. The role of the agriculture on the runoff was clearly shown by [11], who claimed that the runoff conditions are first high before the tillage, and then reduce along the rainy season due to the growth of the crops. They also found that the Normalized Difference Vegetation Index (NDVI) could be a good predictor of the runoff conditions. However, modelling was only performed at the plot scale [12], and not at the catchment scale.

The aim of this study is to assess the skill of two well-known event-based models—the Soil Conservation Service (SCS) model and the Green-Ampt (GA) model in reproducing the flood processes in a semi-arid agricultural catchment of Senegal. To understand the behavior of a watershed during a specific rainfall episode, event-based models are often preferred over continuous models since they require less input data [13] and they possibly reduce the complexity of the hydrological processes. However, the event-based models need to set the initial condition for each event, and to relate this condition to an external predictor [14,15]. Therefore, an event-based model must not only be assessed from its skill to reproduce the floods, but also from the goodness of the relationship between the initial condition of the model and the external predictor, which is linked with. The latter part is often neglected, whereas it is the most important. This dual calibration of an event-based model is addressed in this paper, focusing on the relationship of the initial condition and external predictor, such as antecedent precipitation, event-rainfall characteristics, or satellite-derived normalized difference vegetation index (NDVI) to represent the vegetation stage.

## 2. Study Area and Data Collection

This study was conducted using data and catchment description from hydrological campaign reports done between 1983 and 1990 by two institutions (Office de la Recherche Scientifique et Technique Outre-Mer (now IRD) and the Institut Sénégalais de Recherche Agricole) in the Thysse Kaymor area.

### *2.1. Ndiba Catchment*

The Ndiba catchment (16.2 $km^2$) is situated in the rural community of Thysse Kaymor, in the Sine Saloum region in southern Senegal (Figure 1). The elevations range between 13 and 45 m, and the slope is about 1%. The Ndiba catchment is mostly (over 50%) cultivated (millet and groundnut), and the other parts are bush areas [16].

The Ndiba catchment, as most of the Thysse Kaymor's region, is characterized by sandy soils at the surface, but the proportion of clay increases with depth especially between 0.6 and 1.5 m depth [17]. The soil porosity was assumed to decrease with the depth between 0.31 and 0.25 $cm^3 \cdot cm^{-3}$ [18]: these values were obtained from experimental measurements of both water content $\theta$ and head pressure $h$ at depths 10, 20, 30, 40, 60, 80, 100, 120, 140, 160 cm, in two sites, with either artificial rainfall or Müntz experiment; when the soil saturation was not reached, the water content at saturation was extrapolated from the experimental points ($h$,$\theta$). The hydraulic conductivities at saturation ranged between 10 and 50 $mm \cdot h^{-1}$, depending on the type of tillage (perpendicular or parallel to the slope) and the cumulative rainfall since the last tillage [19]; the results were obtained from 48 infiltration tests that were performed by a disk infiltrometer, each test for a different site within an 900 $m^2$ area; the potential storage of water in these areas was estimated to 170 mm in the first 170 cm. During the first rainfall events at the beginning of the wet season, before tillage, the runoff coefficients are usually high since the soils are almost bare due to animal grazing and soil crusting. Then, the runoff coefficient tends to decrease gradually as the amount of vegetation increase during the growing season [11,20].

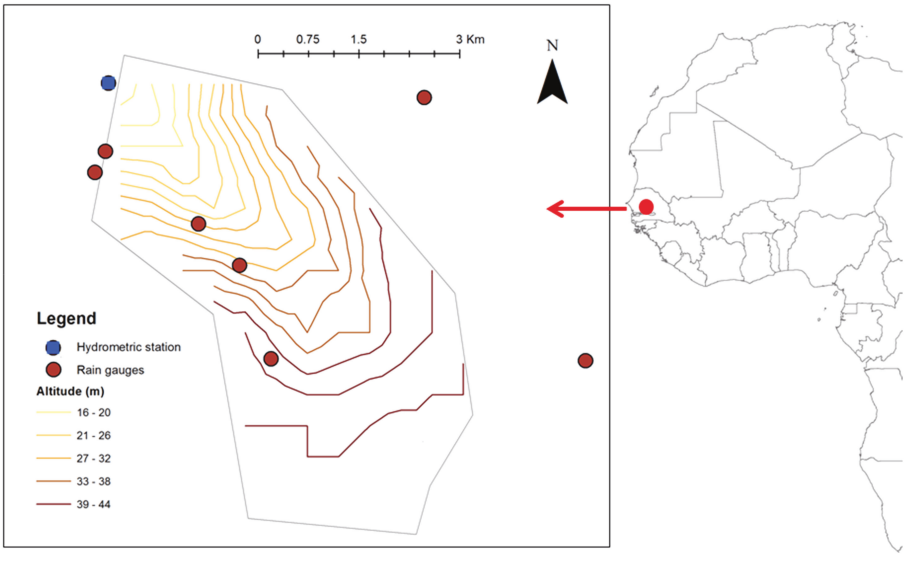


**Figure 1.** Map of the Ndiba catchment.

*2.2. Rainfall and Runoff Data*

Ndiba rainfalls were continuously registered from seven rain gauges (Precis-Mecanique with tipping buckets, surface 400 $cm^2$, graphical recording with daily rotation) in and around the catchment (Figure 1). The mean rainfall for the catchment during the period 1983–1990 was 612.5 mm, and years 1983 and 1984 were particularly dry, as the annual rainfall was less than 500 mm. These years were characterized by a severe drought that affected West Africa since the 1970's. The rainy season occurred during summer months, the maximal rainfall generally occurred in August and its mean value is 183 mm.

Gauging information was available at the hydrometric station of Ndiba (altitude = 13 m). The water levels were continuously recorded by a mechanical OTT 10 stream gauge, between 1983 and 1990. Sixty-four gauging have been performed between 1985 and 1988, up to the water level 160 cm, corresponding to a discharge of 58 $m^3 \cdot s^{-1}$. Those gauging were correctly located around a unique and reliable rating curve. Rainfall and runoff data for Ndiba catchment were extracted from the SIEREM database (http://www.hydrosciences.fr/sierem/) for the period 1983–1990, with a 5-min time interval. Twenty-eight rainfall-runoff events were selected for the study, and were delimited by periods of 48 h when rain intensity did not exceed 1 $mm \cdot h^{-1}$; in addition, the events were definitely selected if the maximal rainfall amount was more than 10 mm and the peak flow more than 1 $m \cdot s^{-1}$. Table 1 shows their main characteristics.

**Table 1.** Flood event characteristics.

| Event | Starting Date | Ending Date | Maximum Discharge ($m^3/s$) | Rainfall Depth (mm) | Maximum Rainfall Intensity (mm/5 min) | Runoff Coefficient (%) | API (mm) | NDVI |
|---|---|---|---|---|---|---|---|---|
| 1 | 13/07/1983 | 14/07/1983 | 35.1 | 77.6 | 139 | 11.0 | 146.0 | 0.164 |
| 2 | 19/07/1983 | 20/07/1983 | 1.28 | 28.8 | 75 | 1.2 | 166.4 | 0.381 |
| 3 | 24/08/1983 | 25/08/1983 | 1.35 | 50.5 | 79 | 0.8 | 219.5 | 1.081 |
| 4 | 2/06/1984 | 3/06/1984 | 56.6 | 32 | 32 | 37.0 | 48.0 | −0.648 |

**Table 1.** *Cont.*

| Event | Starting Date | Ending Date | Maximum Discharge ($m^3/s$) | Rainfall Depth (mm) | Maximum Rainfall Intensity (mm/5 min) | Runoff Coefficient (%) | API (mm) | NDVI |
|---|---|---|---|---|---|---|---|---|
| 5 | 8/06/1984 | 9/06/1984 | 1.06 | 24.7 | 22 | 1.6 | 69.4 | −0.496 |
| 6 | 14/07/1984 | 15/07/1984 | 2.06 | 30.4 | 85 | 3.8 | 189.8 | 1.219 |
| 7 | 19/07/1985 | 20/07/1985 | 15.7 | 32.1 | 138 | 13.0 | 141.4 | 0.311 |
| 8 | 18/08/1985 | 19/08/1985 | 1.64 | 56.5 | 96 | 1.6 | 290.3 | 1.303 |
| 9 | 1/09/1985 | 2/09/1985 | 11 | 63.2 | 107 | 7.1 | 388.4 | 1.558 |
| 10 | 2/08/1986 | 3/08/1986 | 44.2 | 96.3 | 112 | 11.0 | 179.1 | −0.244 |
| 11 | 3/08/1986 | 4/08/1986 | 7.77 | 41.9 | 34 | 6.4 | 230.5 | −0.283 |
| 12 | 12/09/1986 | 13/09/1986 | 4.07 | 50.9 | 116 | 4.8 | 446.7 | 1.684 |
| 13 | 16/06/1987 | 17/06/1987 | 3.87 | 32.2 | 67 | 3.9 | 91.0 | −0.457 |
| 14 | 1/07/1987 | 2/07/1987 | 1.3 | 35 | 48 | 1.3 | 152.9 | 0.767 |
| 15 | 8/08/1987 | 9/08/1987 | 2.29 | 53.3 | 86 | 2.2 | 361.1 | 0.460 |
| 16 | 13/07/1988 | 14/07/1988 | 56.7 | 78 | 100 | 16.0 | 148.2 | 0.115 |
| 17 | 28/07/1988 | 29/07/1988 | 14.6 | 90.5 | 83 | 5.6 | 219.2 | 0.805 |
| 18 | 1/08/1988 | 2/08/1988 | 23.9 | 61.4 | 100 | 13.0 | 245.7 | 0.176 |
| 19 | 2/08/1988 | 3/08/1988 | 12.6 | 52.4 | 46 | 8.8 | 288.2 | 0.038 |
| 20 | 8/08/1988 | 9/08/1988 | 2.23 | 29.2 | 46 | 2.7 | 311.9 | 0.655 |
| 21 | 15/06/1989 | 16/06/1989 | 1.33 | 20.9 | 32 | 1.4 | 23.6 | −0.055 |
| 22 | 17/06/1989 | 18/06/1989 | 55.5 | 38.7 | 77 | 58.0 | 70.1 | −0.070 |
| 23 | 20/06/1989 | 21/06/1989 | 1.04 | 12.4 | 40 | 1.7 | 81.3 | −0.354 |
| 24 | 17/07/1990 | 18/07/1990 | 19.8 | 47.1 | 146 | 9.9 | 116.7 | −0.365 |
| 25 | 20/07/1990 | 21/07/1990 | 1.03 | 38.9 | 105 | 0.5 | 163.2 | −0.020 |
| 26 | 8/08/1990 | 9/08/1990 | 20.5 | 64.2 | 140 | 8.9 | 197.8 | 1.229 |
| 27 | 13/08/1990 | 14/08/1990 | 1.71 | 26.7 | 75 | 2.8 | 214.2 | 1.334 |
| 28 | 17/08/1990 | 18/08/1990 | 4.73 | 39.7 | 118 | 3.9 | 258.6 | 0.613 |

The durations of the events ranged from 0.5 to 14.25 h. The rainfall intensity was generally important at the beginning of the precipitations and decreased along the event. The peak flows ranged from 1.06 to 56.7 $m^3 \cdot s^{-1}$ at the outlet of Ndiba catchment. The runoff coefficients ranged from 0.01 to 0.58. Three events had a maximal discharge that was higher than 50 $m^3 \cdot s^{-1}$: these events were the first floods occurring at the beginning of the rainy season, and had the highest runoff coefficient (cf. Table 1).

### *2.3. Initial Soil Moisture Predictor*

Event-based models predictions often depend on the initial moisture condition of the catchment [13], which should be assessed by measurements, or, in our case, reliable predictors. The base flow at the beginning of an event can be used as a predictor of initial moisture conditions in humid climates, but not in most of Sahelian small catchments because there is no flow before the floods. Other predictors are commonly used to define soil moisture conditions, such as the Antecedent Precipitation Index (API), which is given by [21]:

$$API_j = k \cdot API_{j-1} + P_j \quad (1)$$

where $P_j$ is the rainfall occurring the day $j$ and $API_{j-1}$ the index of the previous day. It is multiplied by $k$, which is a factor that has to be calibrated. The API is computed from daily measurements that were available at the rain gauges.

### *2.4. Normalized Difference Vegetation Index*

For cultivated catchments, the growth of the vegetation often induces a non-stationarity of the hydrological behavior of the catchment, and consequently, of the model parameters [22,23]. Such variability requires to be related to a reliable descriptor of the growth of the vegetation. The Normalized Differential Vegetation Index (NDVI) was used here as a proxy to monitor the seasonal evolution of vegetation, as shown by [11]. The NDVI daily time series have been retrieved

from the NASA's land long term data record (LTDR) project (available online at: https://ltdr.modaps.eosdis.nasa.gov), which aims to produce a global set of data at a 0.05° spatial resolution, which were collected from AVHRR and MODIS instruments for climate studies [24]. The algorithms used to derive the Normalized Differential Vegetation Index (NDVI) from daily surface reflectance are described in [25,26]. The whole database processing is detailed in [24].

The temporal evolution for the years 1983 to 1988 of NDVI over the Ndiba catchment indicates a very close annual cycle with the maximum vegetation development during the summer (Figure 2).

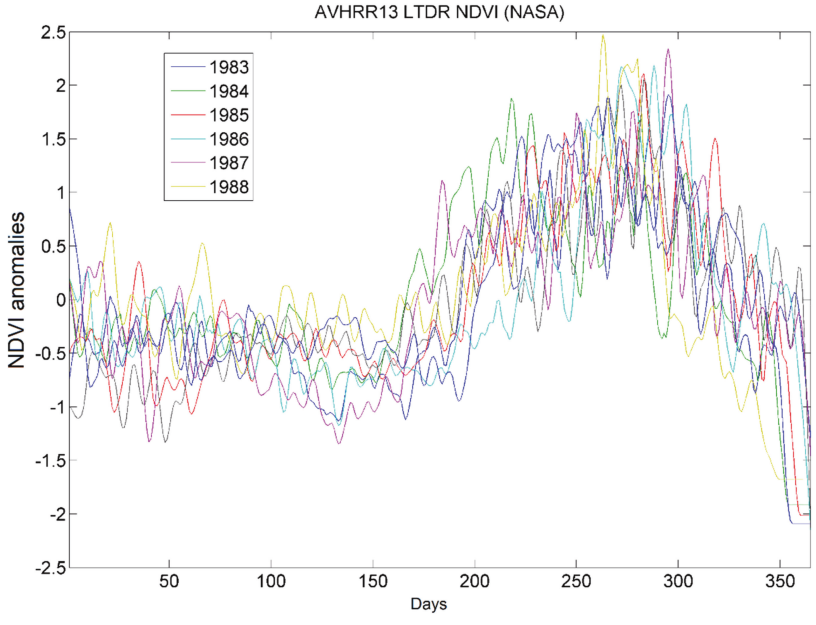


**Figure 2.** Seasonal cycle of long term data record (LTDR)-normalized difference vegetation index (NDVI) over the Ndiba catchment.

### 3. Rainfall-Runoff Modelling

The models were performed within the Atelier Hydrologique Spatialisé (ATHYS) modelling platform, which was developed at the Hydrosciences Montpellier laboratory [27,28]. ATHYS brings together a large set of distributed models within a consistent and easy-to-use environment, including processing of hydrometeorological and geographical data. ATHYS is an open software, which can be downloaded for Windows or Linux (www.athys-soft.org).

The distributed models operated over a grid mesh of regular squared cells. The basic information was brought by a Digital Elevation Model (DEM), which supplied elevation, slope, upstream area, and flowpath for each cell. Here, we used the Advanced Spaceborne Thermal Emission and Reflection Parameter (ASTER) DEM, projected to a UTM horizontal resolution of 30 m. Then, the rainfall was interpolated over the grid cells via the inverse distance interpolation method, at every time step, here 5 min. The runoff models (here, SCS and Green-Ampt) operated thus with 30 m cell size and 5 min time step. Each cell produced a cell-hydrograph at the outlet of the catchment, depending on the runoff model and the routing model (here, the distributed lag and route model). The complete flood hydrograph at the outlet of the catchment was finally obtained as the sum of the cell-hydrographs.

### 3.1. SCS Runoff Model

The United States Soil Conservation Service developed an empirical model to estimate runoff losses [29]. To date, the SCS method is one of the most popular runoff models, and it was the object of many improvements as well in the formulation of the model as in the interpretation of its parameters (see [30] for a review).

Although it was first designed to relate the cumulated runoff and rainfall at the event scale, it is possible to integrate time into this model to predict infiltration rates [31,32]. The SCS model that is considered here gives the instantaneous runoff at any time of the event [32]:

$$P_e(t) = P_b(t)\left(\frac{P(t) - 0.2S}{P(t) + 0.8S}\right)\left(2 - \frac{P(t) - 0.2S}{P(t) + 0.8S}\right) \tag{2}$$

where $P_e(t)$ is the effective rainfall at time $t$, $P_b(t)$ the precipitation at time $t$, $P(t)$ the cumulative rainfall since the beginning of the event. $S$ is the maximal water storage capacity at the beginning of the event. The runoff coefficient is expressed by the quantity that multiplies $P_b(t)$, in the second member of the previous equation; it increases with the cumulative rainfall and tends to 1 when the cumulative rainfall tends to infinity.

To consider that the runoff coefficient decreases during periods when no rain occurs, a linear decrease of the cumulated rainfall was considered through a discharge coefficient $ds$ [$T^{-1}$] [13,33]:

$$\frac{dP(t)}{d(t)} = P_b(t) - ds \cdot P(t) \tag{3}$$

The parameters of the model are $S$ and $ds$. The $S$ parameter directly controls the main flood peak and volume, while $ds$ contributes to adjust the different flood peaks and volumes resulting from successive rainfalls within a given event. Note that the $ds$ parameter emulates some kind of variable infiltration rate, which depends on the cumulated rainfall $P(t)$. The $S$ and $ds$ parameters were considered to be constant over the catchment, so that the distribution only concerned the rainfall interpolated for each cell.

### 3.2. Green-Ampt Model

Green-Ampt model [34] is based on physical measurable parameters and describes a hortonian process of water infiltration. The infiltration capacity $f(t)$ is expressed by the following equation:

$$f(t) = Ks \cdot \left(\frac{(\theta_s - \theta_i) \cdot \Psi}{F(t)} + 1\right) \tag{4}$$

where $F(t)$ is the cumulated infiltration [L], $\theta_s$ the saturated soil moisture [$L^3 \cdot L^{-3}$], $\theta_i$ the initial soil moisture [$L^3 \cdot L^{-3}$], $K_s$ the hydraulic conductivity at saturation [$L \cdot T^{-1}$] and $\Psi$ the suction [L].

As for the SCS runoff model, the GA parameters were considered to be constant over the catchment, although the land use and the soil types were probably not homogeneous over the catchment. The parameters were thus considered as averaged values over the catchment, in order to be coherent with sparse data about the soil properties.

### 3.3. Routing Model

SCS and Green-Ampt models were coupled to a lag and route model at the cell scale, to produce a cell-hydrograph at the outlet of the catchment, calculated by:

$$Q_m(t) = A \cdot \int_{t_0}^{t - T_m} \frac{Pe(\tau)}{K_m} \cdot exp\left(-\frac{t - T_m - \tau}{K_m}\right) d\tau \tag{5}$$

where $A$ was the cell-area [$L^2$], $P_e$ the effective rainfall [L], $T_m$ the routing time [T]), and $K_m$ the lag time [T] from the cell m to the outlet.

This model, available in ATHYS, was already used by [33]. It simply enables the Unit Hydrograph theory, by using the impulse response function:

$$h(t) = 0 \quad \text{if } t < T_m$$

$$h(t) = \frac{1}{K_m} \cdot exp\left(\frac{t - T_m}{K_m}\right) \quad \text{if } t > T_m$$

The routing time $T_m$ was calculated from the length $l_k$ and the flux velocity $V_k$ of each $k$-cell between the $m$-cell and the outlet of the catchment. The lag time $K_m$ was assumed to be linearly dependent of the routing time $T_m$: $K_m = K_0 \cdot T_m$. In the following, the velocity $V_k$ was considered as the same for all of the cells: $V_k = V_0$, and $K_0$ as a constant of the catchment.

The routing time $T_m$ and lag time $K_m$ induced an actual distribution of the travel times of the runoff over the catchment: the farther from the outlet the cell m is, the larger the routing time and the lag time are. As mentioned above, the complete flood hydrograph at the outlet of the catchment was obtained by the sum of all the cell-hydrographs.

The complete models were denoted after either SCS-LR or SCS, and GA-LR or Green-Ampt.

### *3.4. Model Calibration*

SCS-LR and GA-LR models parameters were either preset from field measurements or empirical/physical consideration, or calibrated using the BLUE (Best Linear Unbiased Estimator) method. In this latter case, the objective consists of minimizing the cost function, J(**x**) in order to obtain the optimal values of the variables that are stored in a control vector, **x** [35]:

$$\mathrm{J}(\mathbf{x}) = \frac{1}{2}(\mathbf{x} - \mathbf{x}^{\mathrm{b}})^T \mathbf{B}^{-1}(\mathbf{x} - \mathbf{x}^{\mathrm{b}}) + \frac{1}{2}(\mathbf{y}^{\mathrm{o}} - H(\mathbf{x}))^T \mathbf{R}^{-1}(\mathbf{y}^{\mathrm{o}} - H(\mathbf{x})) \tag{6}$$

The control vector **x**, size n, contains the set of n variables to be optimized, i.e., the model parameters; $\mathbf{x}^{\mathrm{b}}$ is the background vector of size n, which contains the a priori values of the control vector variables. $\mathbf{y}^{\circ}$ is a vector of size p, which contains the p observations to be considered. $H$ is the observation operator, i.e., the rainfall-runoff model, and supplies the predicted runoff. **B** (size n × n) and **R** (size p × p) are the error covariance matrices, respectively, associated to the background, $\mathbf{x}^{\mathrm{b}}$, and the observations, $\mathbf{y}^{\mathrm{o}}$. The cost function J(**x**) thus quantifies both the distance between the control vector, **x**, and the background, $\mathbf{x}^{\mathrm{b}}$, and the distance between the runoff predicted by the model and the observed runoff, $\mathbf{y}^{\circ}$, weighted, respectively, by the error covariance matrices **B** and **R**. The smaller the covariance in **B** is, the closer to the background the control vector is; the smaller the covariance in **R** is, the closer to the observation the output of the model is.

As a gradient method, the BLUE method allows for a quick computation of the optimized parameters. The parameters were in our case considered as independent (null covariance) and a large variance was considered in the **B** matrix, in order that the parameters would be low related with the background. This made that the cost function J(**x**) was actually equivalent to any form of quadratic error between the predicted and observed runoff.

For sake of simplicity, the efficiency of the model was also expressed by the Nash-Sutcliffe coefficient *NS*:

$$NS = 1 - \frac{\sum_i (X_i - Y_i)}{\sum_i (Y_i - \overline{Y})} \tag{7}$$

where $X_i$ and $Y_i$ are the observed and simulated discharges for $i$-time steps, and $\overline{Y}$ the mean value of the observed discharges during the event. The closer *NS* is from 1, the better the correlation between the observed and simulated discharges.

## 4. Results

### *4.1. SCS-Model Calibration*

#### 4.1.1. Estimation of the SCS-Model Parameters

As said above, the SCS-LR parameters were either preset from field measurements or empirical/methodological consideration, or calibrated by using the BLUE method. The *ds* parameter was set in order to remove the small floods due to secondary rainfalls, which were not seen in the observed data. A convenient value $ds = 8\ d^{-1}$ was kept as a constant for all of the events. The parameters $V_0$ and $K_0$ were found to be strongly dependent, so the $K_0$ parameter was empirically set as $K_0 = 0.75$ for all of the events.

Then, a simultaneous calibration of $S$ and $V_0$ parameters was realized by using the BLUE method for each event. For the 28 selected events, *NS* values ranged from 0.30 to 0.99 (median = 0.87), showing for most events a good agreement between observed and calibrated discharges. $S$ parameter values ranged from 15.2 to 175.2 mm (median = 92 mm) and $V_0$ from 0.85 $m{\cdot}s^{-1}$ to 5.8 $m{\cdot}s^{-1}$ (median = 1.68 $m{\cdot}s^{-1}$), Table 2.

**Table 2.** Models results.

| | SCS-LR | | | GA-LR | | |
|---|---|---|---|---|---|---|
| **Event** | **$S$ (mm)** | **$V_0$ ($m{\cdot}s^{-1}$)** | ***NS*** | **$K_s$ ($mm{\cdot}h^{-1}$)** | **$V_0$ ($m{\cdot}s^{-1}$)** | ***NS*** |
| 1 | 134.1 | 1.37 | 0.59 | 54.2 | 1.21 | 0.54 |
| 2 | 104.9 | 1.98 | 0.82 | 38.1 | 1.71 | 0.71 |
| 3 | 161.9 | 4.06 | 0.83 | 47.1 | 3.02 | 0.45 |
| 4 | 16.8 | 5.54 | 0.67 | 1.8 | 3.96 | 0.95 |
| 5 | 56.7 | 0.86 | 0.65 | 6.9 | 0.42 | 0.56 |
| 6 | 92.0 | 1.14 | 0.92 | 35.1 | 1.05 | 0.94 |
| 7 | 81.4 | 1.34 | 0.97 | 39.5 | 1.05 | 0.97 |
| 8 | 136.3 | 1.19 | 0.82 | 30.0 | 0.87 | −2.19 |
| 9 | 159.5 | 1.70 | 0.95 | 64.3 | 1.58 | 0.93 |
| 10 | 122.4 | 2.53 | 0.96 | 31.0 | 2.21 | 0.9 |
| 11 | 70.2 | 2.16 | 0.95 | 15.7 | 1.68 | 0.94 |
| 12 | 136.6 | 0.94 | 0.87 | 78.1 | 1.03 | 0.7 |
| 13 | 89.4 | 1.32 | 0.7 | 28.8 | 1.16 | 0.48 |
| 14 | 116.8 | 1.22 | 0.68 | 28.9 | 1.32 | 0.71 |
| 15 | 145.4 | 0.90 | 0.83 | 53.9 | 0.77 | 0.7 |
| 16 | 153.7 | 14.28 | 0.77 | 43.1 | 4.96 | 0.88 |
| 17 | 172.9 | 2.29 | 0.98 | 32.5 | 1.36 | 0.93 |
| 18 | 159.4 | 1.88 | 0.93 | 48.7 | 1.62 | 0.91 |
| 19 | 92.0 | 1.73 | 0.84 | 22.9 | 1.14 | 0.89 |
| 20 | 89.9 | 0.95 | 0.91 | 28.8 | 0.93 | 0.86 |
| 21 | 62.8 | 3.70 | 0.88 | 6.9 | 3.43 | 0.85 |
| 22 | 3.7 | 1.62 | 0.61 | 3.3 | 1.61 | 0.9 |
| 23 | 34.8 | 1.88 | 0.57 | 6.6 | 2.01 | 0.6 |
| 24 | 73.9 | 1.44 | 0.86 | 35.0 | 1.17 | 0.87 |
| 25 | 89.1 | 2.37 | 0.97 | 25.4 | 0.97 | 0.83 |
| 26 | 103.6 | 2.20 | 0.98 | 56.5 | 2.10 | 0.98 |
| 27 | 74.3 | 1.37 | 0.94 | 28.9 | 1.20 | 0.91 |
| 28 | 86.2 | 1.65 | 0.94 | 35.2 | 1.52 | 0.93 |
| Median | 92.0 | 1.68 | 0.87 | 31.8 | 1.34 | 0.88 |
| Average | 100.7 | 2.34 | 0.84 | 33.1 | 1.68 | 0.70 |

No correlation could be found between the velocity $V_0$ and other event feature, such as peak flow and initial water content. The variation of the velocity might be mainly due to uncertainties in time of the recording mechanical gauges. Such uncertainty can reach some tenth of minutes, and due to the short response time of the catchment, can impact the $V_0$ value a lot.

4.1.2. Relation between *S* and Antecedent Moisture Indicator

The calibrated values of *S* for SCS-model for all of the flood events were compared with the previous soil moisture indicator described before (API). For this model, the relation *S*-API was significant, although weak ($R^2 = 0.38$, $P_{Fisher} < 1\%$), but exhibited an opposite correlation to what could be expected (Figure 3). The maximal capacity of retention was indeed supposed to decrease with increased wetness conditions. For example, in a small mountainous Mediterranean catchment, [13] found a negative correlation between *S* and API, with a Pearson correlation coefficient $r = -0.68$). But, in the Ndiba catchment, the wetter the soil initially was, the lesser the runoff was. It was probably due because the classical role of the water content before the flood should be here a secondary factor, and that other phenomena would play a major role in the hydrological response of the catchment. It was clear that the tillage of the soil indeed modified a lot the runoff: for example, the highest runoff, consequently, a small *S*, was obtained for the first floods of the rainy season, consequently, a low API, when no tillage has been made. But, as we had no data about the tillage practices during the rainy season, it was not possible to precisely quantify the role of the tillage on the runoff.

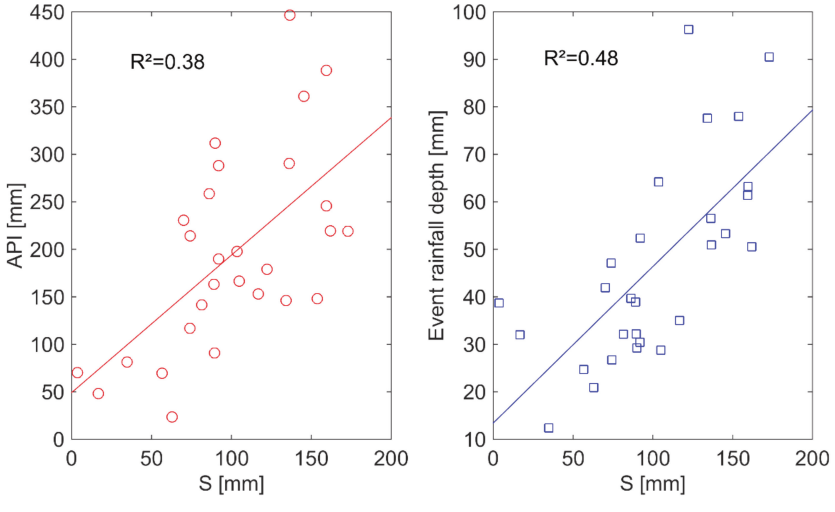


**Figure 3.** Correlation between *S*, Antecedent Precipitation Index (API), and rainfall depth.

4.1.3. Relation between *S* and NDVI

As pointed out by [11], the Sahelian agricultural catchments are prone to highly non stationary conditions due to the tillage of the soils and the growth of the plants. The calibrated values of *S* were then related to the NDVI index, which was associated to the development of the vegetation. A significant, but weak ($R^2 = 0.29$, $P_{Fisher} < 1\%$), correlation was found again, which denoted the role of the vegetation in the increase of the maximal water storage capacity of the soil when the plants grow. Note that API and NDVI were dependent, since a linear relationship could be drawn between both indexes, with $R^2 = 0.47$, when considering the values that are corresponding to our 28 events data base. Thus, the positive correlation between the calibrated *S* values and API would be an artefact due to the development of the vegetation.

4.1.4. Relation between *S* and Rainfall Depth

The calibrated *S* parameter of SCS-model was also correlated with the rainfall depth. As shown in Figure 3, *S* tended to increase with rainfall depth giving almost a linear relation between *S* and rainfall depth ($R^2 = 0.48$, $P_{Fisher} < 1\%$). The relation between rainfall depth and the *S* parameter was

not expected whilst using the SCS-model; but, some studies (among other [36,37]) showed a relation between the *CN* curve number (consequently *S*) and the rainfall depth, for high infiltration sandy soils: *CN* decreases (consequently *S* increases) with rainfall depth. A possible explanation was given by [38], who claimed that higher rainfall depths increase the flooded part of the soil, and that water rises up to the plants bottom and infiltrates more than in the crusted soil.

### *4.2. Green-Ampt Model Calibration*

An alternative model set-up was considered, with the Green-Ampt model for infiltration. As for the SCS model, the Green-Ampt parameters were either preset or calibrated by the BLUE method. A mean constant value of the soil moisture at saturation state was applied, $\theta_s$ = 0.30 $cm^3$ $cm^{-3}$, according the field measurements [18]. The initial soil moisture value at the beginning of an event was considered empirically as a linear function of the API index: $\theta_i$ = API/2000; the initial water content thus ranged between 0.02 and 0.22 $cm^3 \cdot cm^{-3}$. A suction value of 75 mm was applied, which corresponds to a mean value found in literature for the sandy loam soils [39]. The $K_0$ parameter was set as $K_0$ = 0.75, the same value than for SCS-LR.

Then, simultaneous calibration of hydraulic conductivity $K_s$ and velocity $V_0$ was performed by using the BLUE method. The median *NS* coefficient was 0.88. The median calibrated $K_s$ value was 31.8 $mm \cdot h^{-1}$, which looked in agreement with the values measured in the catchment [19]. However, the calibrated $K_s$ values varied widely between 1 and more than 60 $mm \cdot h^{-1}$ at the event scale. The median calibrated $V_0$ was 1.34 $m \cdot s^{-1}$.

### *4.3. Seasonal Evolution of the $K_s$ Parameter Linked with NDVI Anomalies*

The calibrated values of the $K_s$ parameter were correlated with the NDVI anomalies ($R^2$ = 0.44, $P_{Fisher}$ < 1%, Figure 4). This result indicates that the variation that was observed through the year in hydraulic conductivity was partly driven by the evolution of vegetation growth during the rainy season, as pointed out by [11]. This hydrologic behaviour can thus be reproduced by the Green Ampt model with varying infiltration rates during the wet season, according to the NDVI anomalies. Note that the Green-Ampt model scored better than the SCS model, when considering the relationship with NDVI and the main variable parameter of each model: *S* for SCS and $K_s$ for Green-Ampt.

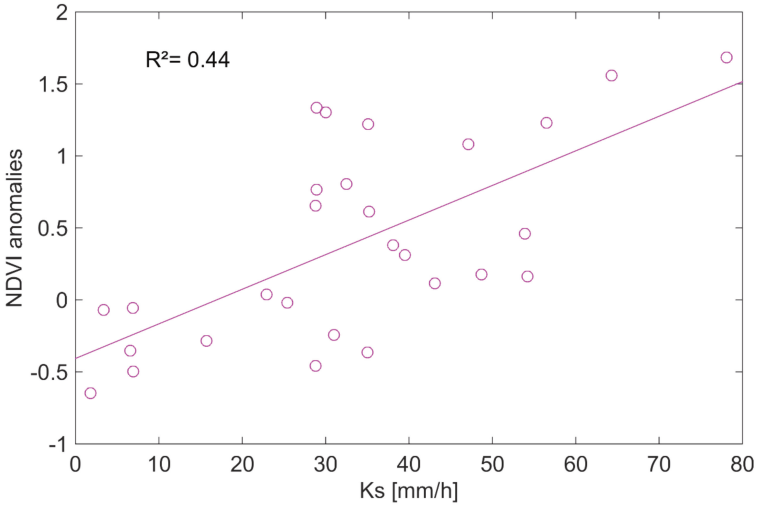


**Figure 4.** Correlation between hydraulic conductivities ($K_s$) and NDVI.

*4.4. Predictive Scores of the Models*

The actual goodness of the models was expressed by the predictive scores, i.e., the NS values that were obtained with the predicted values of $S$ (for SCS) or $K_s$ (for Green-Ampt). The NS values of the 28 events were sorted by descendant order for each model, using the different relationships that were considered as significant (Figure 5): $S$-NDVI and $S$-P for SCS, $K_s$-NDVI for GA. The best predictive scores were achieved for SCS when using the $S$-P relationship (median $NS = 0.33$), whereas Green-Ampt when using the $K_s$-NDVI relationship offered the worst predictive score (media $NS = -0.21$); SCS scored better when using NDVI (median $NS = 0.08$), although the $R^2$ was higher for $K_s$-NDVI than for $S$-NDVI. This result is due to the fact that GA is very sensitive to $K_s$, whereas the sensitivity of SCS with $S$ is less. So, SCS globally scored better than Green-Ampt, in terms of predictive scores. However, using a predictor of $S$, like the rainfall amount, is not appropriate for applications, such as flood forecasting, because the rainfall amount is not known at the moment of the forecast. In this case, it would be preferable to use SCS with the NDVI predictor for $S$.

The predictive scores of the model, however, remained rather low. It could be because the calibrations of the models were not optimal: maybe it would be worth to consider that some other parameters had to vary from an event to another (e.g., $ds$ or $\Psi$); or, because the models were not enough appropriate for this kind of catchment; but we think that the low predictive scores were mostly due because we had not information about the dates and the kind of tillage. Ndiaye et al. [19] showed indeed that tillage had a significant effect on runoff, depending on the type (along or across the slope), and that the effect of the tillage disappeared after nearly 170 mm of cumulated rainfall since the date of tillage. Although vegetation growth should be clearly conditioned by tillage, the NDVI index was probably not efficient enough to restore accurately the tillage practices during the rainy season. We suggest first searching in this direction for improving the models.

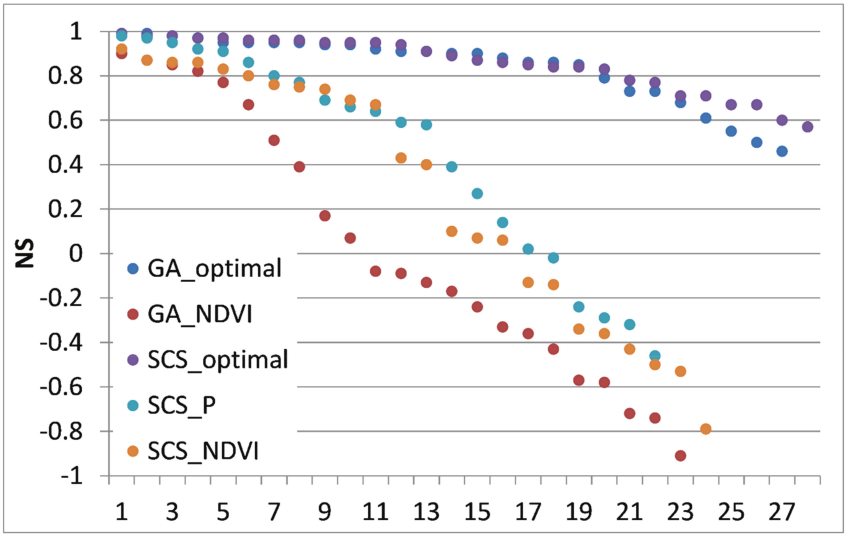


**Figure 5.** Optimal and predictive scores of the models. GA_optimal corresponds to the calibrated values of $K_s$; Green-Ampt (GA)_NDVI to the $K_s$ predicted by the relationship $K_s$-NDVI; Soil Conservation Service (SCS)_optimal to the calibrated values of $S$; SCS_NDVI to the $S$ predicted by the relationship $S$-NDVI; SCS_P to the $S$ predicted by the cumulated rainfall of the event. For a given model, the same values of $V_0$ were applied, and corresponded to the calibrated values of $V_0$ for SCS or Green-Ampt.

## 5. Conclusions

The goal of this study was to evaluate the efficiency of event-based rainfall-runoff model, such as SCS-LR or GA-LR for flood prediction in a small catchment that is located in south Senegal. Twenty-eight flood events were chosen to compare the efficiency of both event-based models.

The application of the SCS-model was found satisfactory to reproduce the observed discharges after calibration of its parameters. However, the initial condition of the model could not be predicted as usual, in relation with the water content of the soil at the beginning of the event. The API index, derived from the antecedent rainfalls, was positively correlated with the $S$ parameter, whereas the SCS model usually considers that the correlation should be negative. The $S$ values were also correlated to the NDVI during the event. That is in agreement with the role of the growth of the plants, which induces highly non-stationary conditions for the hydrological response of the catchment, as noted by various authors, and the initial soil moisture conditions should be a secondary factor. The $S$ values were also related to the cumulated rainfall of the event, which finally appeared as the best predictor for $S$.

The Green-Ampt model results indicated its adequacy to reproduce the flood events in the catchment. As for the SCS-CN model, the correlation of the model parameters with antecedent precipitation was positive, whereas it was expected to be negative. However, a significant correlation between the hydraulic conductivities ($K_s$) for each event and the normalized difference vegetation index was observed, highlighting the influence of vegetation cover on soil infiltration properties. The Green-Ampt parameters were in agreement with the measured, e.g., hydraulic conductivity at saturation, or estimated values. But, Green-Ampt finally scored less than SCS, because a high sensitivity to the $K_s$ parameter.

At this point, however, the predictive scores of the models are still low when considering the $NS$ values that were obtained with the best predicted values of $S$ or $K_s$. The main reason seems to be that the tillage practices are not actually taken into account in the models, nor in the predictors (e.g., NDVI) of the parameters of the models. This seems to be the main point to study for the improvement of the predictive scores of the models. In addition, added value could be brought by considering the whole nested set of catchments in Thysse Kaymor.

To conclude, it is worth noting the interest of such existing large data sets dating from the 80's, even before, Thysse Kaymor being an example among other. As these data are still underemployed for modeling benchmark and hydrological processes understanding, they could fill a gap concerning flood predicting in West Africa (e.g., T-years return period flood), and bring more confidence in designing small hydraulic works in small (ponding areas, culverts) as well as large (dams, bridges) catchments.

**Acknowledgments:** We thank the editors M. Piña and M. Li, and three anonymous reviewers for their valuable help in improving the quality of the paper. We are also very grateful to Nathalie Rouché and Jean-Emmanuel Paturel for providing the rainfall-runoff data used in this study.

**Author Contributions:** Christophe Bouvier and Yves Tramblay conceived and designed the modelling protocol and contributed to the materials; Christophe Bouvier, Lamia Bouchenaki and Yves Tramblay analyzed the data; Christophe Bouvier and Lamia Bouchenaki wrote the paper.

## References

1. Di Baldassarre, G.; Montanari, A.; Lins, H.F.; Koutsoyiannis, D.; Brandimarte, L.; Blöschl, G. Flood fatalities in Africa: From diagnosis to mitigation. *Geophys. Res. Lett.* **2010**, *37*, L22402. [CrossRef]
2. Tschakert, P.; Sagoe, R.; Ofori-Darko, G.; Codjoe, S.N. Floods in the Sahel: An analysis of anomalies, memory, and anticipatory learning. *Clim. Chang.* **2010**, *103*, 471–502. [CrossRef]
3. Amoussou, E.; Tramblay, Y.; Totin, H.; Mahé, G.; Camberlin, P. Dynamics and modelling of floods in the river basin of Mono in Nangbeto, Togo/Benin. *Hydrol. Sci. J.* **2014**, *59*, 2060–2071. [CrossRef]
4. Komi, K.; Neal, J.; Trigg, M.A.; Diekkrüger, B. Modelling of flood hazard extent in data sparse areas: A case study of the Oti River basin, West Africa. *J. Hydrol. Reg. Stud.* **2017**, *10*, 122–132. [CrossRef]

5. Cappelaere, B.; Vieux, B.E.; Peugeot, C.; Maia, A.; Séguis, L. Hydrologic process simulation of a semiarid, endoreic catchment in Sahelian West Niger: 2. Model calibration and uncertainty characterization. *J. Hydrol.* **2003**, *279*, 244–261. [CrossRef]
6. Le Lay, M.; Saulnier, G.M.; Galle, S.; Séguis, L.; Metadier, M.; Peugeot, C. Model representation of the Sudanian hydrological processes: Application on the Donga catchment (Benin). *J. Hydrol.* **2008**, *363*, 32–41. [CrossRef]
7. FAO. *Crues et Apports. Manuel Pour L'estimation des Crues Décennales et des Apports Annuels Pour les Petits Bassins Versants non Jaugés de L'afrique Sahélienne et Tropicale Sèche*; Bulletin FAO D'irrigation et de Drainage: Rome, Italy, 1996; Volume 54, p. 265. ISBN 92-5-203874-4. (In French)
8. Albergel, J.; Chevalier, P.; Lortic, B. D'Oursi à Gagara: Transposition d'un modèle de ruissellement dans le Sahel (Burkina-Faso). *Hydrol. Cont.* **1987**, *2*, 77–86. (In French)
9. Bouvier, C.; Desbordes, M. Un modèle de ruissellement pour les villes de l'Afrique de l'Ouest. *Hydrol. Cont.* **1990**, *5*, 77–86. (In French)
10. Lamachere, J.M.; Puech, C. Cartographie des états de surface par télédétection et prédétermination des crues des petits bassins versants en zones sahélienne et tropicale sèche. In *L'hydrologie Tropicale: Géoscience et Outil Pour le Développement*; International Association of Hydrological Sciences: Wallingford, UK, 1996; p. 238. (In French)
11. Séguis, L.; Bader, J.C. Modélisation du ruissellement en relation avec l'évolution saisonnière de la végétation (mil, arachide, jachère) au centre Sénégal. *Revue Sci. L'eau* **1997**, *4*, 419–438. (In French) [CrossRef]
12. Bader, J.C. Modèle analogique de ruissellement à stockage de surface: Test sur parcelles et extrapolation sur versant homogène. *Hydrol. Sci. J.* **1994**, *39*, 569–592. (In French) [CrossRef]
13. Tramblay, Y.; Bouvier, C.; Martin, C.; Didon-Lescot, J.F.; Todorovik, D.; Domergue, J.M. Assessment of initial soil moisture conditions for event-based rainfall–runoff modelling. *J. Hydrol.* **2010**, *387*, 176–187. [CrossRef]
14. Berthet, L.; Andreassian, V.; Perrin, C.; Javelle, P. How crucial is it to account for the antecedent moisture conditions in flood forecasting? Comparison of event-based and continuous approaches on 178 catchments. *Hydrol. Earth Syst. Sci.* **2009**, *13*, 819–831. [CrossRef]
15. Tramblay, Y.; Amoussou, E.; Dorigo, W.; Mahé, G. Flood risk under future climate in data sparse regions: Linking extreme value models and flood generating processes. *J. Hydrol.* **2014**, *519*, 549–558. [CrossRef]
16. Valentin, C. *Les Etats de Surface des Bassins Versants de Thysse Kaymor (Sénégal)*; Rapport ORSTOM 35.489; Office de la Recherche Scientifique Et Technique Outre-Mer (ORSTOM): Dakar, Senegal, 1990. (In French)
17. Diome, F. Rôle de la Structure du sol Dans son Fonctionnement Hydrique. Sa Quantification par la Courbe de Retrait. Ph.D. Thesis, Université Cheikh Anta Diop, Dakar, Senegal, 1996; p. 131. (In French)
18. Albergel, J.; Bernard, A.; Ruelle, P.; Touma, J. Hydrodynamique des Sols. Bassins Expérimentaux de Thysse Kaymor. Rapport de la Campagne de Mesures Fev–Avr 1988. 1989. Available online: http://horizon.documentation.ird.fr/exl-doc/pleins_textes/doc34-05/27469.pdf (accessed on 30 March 2018).
19. Ndiaye, B.; Esteves, M.; Vandervaere, J.P.; Lapetite, J.M.; Vauclin, M. Effect of rainfall and tillage direction on the evolution of surface crusts, soil hydraulic properties and runoff generation for a sandy loam soil. *J. Hydrol.* **2005**, *307*, 294–311. [CrossRef]
20. Rodier, J.A. *Caractéristiques des Crues des Petits Bassins Versants Représentatifs au Sahel*; Cahiers ORSTOM, Série Hydrologie; Office De La Recherche Scientifique Et Technique Outre-Mer (ORSTOM): Dakar, Senegal, 1985; Volume XXI, pp. 3–26. (In French)
21. Kohler, M.A.; Linsley, R.K. *Predicting Runoff from Storm Rainfall*; Res. Paper 34; U.S. Weather Bureau: Washington, DC, USA, 1951.
22. Zhang, L.; Wang, J.; Bai, Z.; Lv, C. Effects of vegetation on runoff and soil erosion on reclaimed land in an opencast coal-mine dump in a loess area. *Catena* **2015**, *128*, 44–53. [CrossRef]
23. Hunink, J.E.; Eekhout, J.P.C.; de Vente, J.; Contreras, S.; Droogers, P.; Baille, A. Hydrological Modelling Using Satellite-Based Crop Coefficients: A Comparison of Methods at the Basin Scale. *Remote Sens.* **2017**, *9*, 174. [CrossRef]
24. Pedelty, J.; Devadiga, S.; Masuoka, E.; Brown, M.; Pinzon, J.; Tucker, C.; Vermote, E.; Prince, S.; Nagol, J.; Justice, C.; et al. Generating a Long-term Land Data Record from the AVHRR and MODIS Instruments. In Proceedings of the IEEE International Geoscience and Remote Sensing Symposium (IGARSS 2007), Barcelona, Spain, 23–28 July 2007; Institute of Electrical and Electronics Engineers: New York, NY, USA, 2007; pp. 1021–1025.

25. Vermote, E.F.; Kaufman, Y.J. Absolute calibration of AVHRR visible and near-infrared channels using ocean and cloud views. *Int. J. Remote Sens.* **1995**, *16*, 2317–2340. [CrossRef]
26. Saleous, N.Z.; Vermote, E.F.; Justice, C.O.; Townshend, J.R.G.; Tucket, C.J.; Goward, S.N. Improvements in the global biospheric record from the Advanced Very High Resolution Radiometer (AVHRR). *Int. J. Remote Sens.* **2000**, *21*, 1251–1277. [CrossRef]
27. Bouvier, C.; Delclaux, F. ATHYS: A hydrological environment for spatial modelling and coupling with a GIS. In Proceedings of the HydroGIS 96, Vienna, Austria, 16–19 April 1996; AIHS Publication: Wallingford, UK, 1996; pp. 19–28.
28. Bouvier, C.; Crespy, A.; L'Aour-Dufour, A.; Crès, F.-N.; Delclaux, F.; Marchandise, A. Distributed Hydrological Modelling—The ATHYS platform. In *Environmental Hydraulics Series 5, Modelling Software*; Tanguy, J.-M., Ed.; Wiley: New York, NY, USA, 2010; pp. 83–100.
29. USDA, Soil Conservation Service. *National Engineering Handbook*; Supplement A, Section 4, Hydrology; Soil Conservation Service: Washington, DC, USA, 1956.
30. Ponce, V.; Hawkins, R. Runoff Curve Number: Has It Reached Maturity? *J. Hydrol. Eng.* **1996**, *1*, 11–19. [CrossRef]
31. Aron, G.; Miller, A.C.; Lakatos, D.F. Infiltration formula based on SCS Curve Number. *J. Irrig. Drain. Div.* **1977**, *103*, 419–428.
32. Gaume, E.; Livet, M.; Desbordes, M.; Villeneuve, J.P. Hydrological analysis of the river Aude, France, flash flood on 12 and 13 November 1999. *J. Hydrol.* **2004**, *286*, 135–154. [CrossRef]
33. Coustau, M.; Bouvier, C.; Borrell-Estupina, V.; Jourde, H. Flood modelling with a distributed event-based parsimonious rainfall-runoff model: Case of the karstic Lez river catchment Nat. *Hazards Earth Syst. Sci.* **2012**, *12*, 1119–1133. [CrossRef]
34. Green, W.H.; Ampt, G.A. Studies on Soil Physics. *J. Agric. Sci.* **1911**, *4*. [CrossRef]
35. Coustau, M.; Ricci, S.; Borrell-Estupina, V.; Bouvier, C.; Thual, O. Benefits and limitations of data assimilation for discharge forecasting using an event-based rainfall–runoff model. *Nat. Hazards Earth Syst. Sci.* **2013**, *13*, 583–596. [CrossRef]
36. Hawkins, R.H. Asymptotic Determination of Runoff Curve Numbers from Data. *J. Irrig. Drain. Eng.* **1993**, *119*, 334–345. [CrossRef]
37. Rezaei-Sadr, H. Influence of coarse soils with high hydraulic conductivity on the applicability of the SCS-CN method. *Hydrol. Sci. J.* **2017**, *62*, 843–848. [CrossRef]
38. Planchon, O.; Janeau, J.L. Le Fonctionnement Hydrodynamique à L'échelle du Versant. In *Equipe HYPERBAV Structure et Fonctionnement Hydropédologique d'un Petit Bassin Versant de Savane Humide*; Etudes et Theses; Office de la Recherche Scientifique et Technique Outre-Mer (ORSTOM): Paris, France, 1990; pp. 165–183.
39. Chow, V.T.; Maidment, D.R.; Mays, L.W. *Applied Hydrology*; McGraw Hill: New York, NY, USA, 1988; p. 572.